

THE STRUCTURE AND ENVIRONMENT
OF GALAXY CLUSTERS IN SIMULATIONS
AND OBSERVATIONS

by

Matthew W. Fong



APPROVED BY SUPERVISORY COMMITTEE:

Lindsay J. King, Chair

Michael Kesden

Mustapha Ishak-Boushaki

Phillip Anderson

Roderick Heelis

Copyright © 2019

Matthew W. Fong

All rights reserved

THE STRUCTURE AND ENVIRONMENT
OF GALAXY CLUSTERS IN SIMULATIONS
AND OBSERVATIONS

by

MATTHEW W. FONG, BS, MS

DISSERTATION

Presented to the Faculty of
The University of Texas at Dallas
in Partial Fulfillment
of the Requirements
for the Degree of

DOCTOR OF PHILOSOPHY IN
PHYSICS

THE UNIVERSITY OF TEXAS AT DALLAS

May 2019

ACKNOWLEDGMENTS

First of all I would like to express my gratitude to those on my committee: Dr. Lindsay King, Dr. Michael Kesden, Dr. Mustapha Ishak-Boushaki, Dr. Phillip Anderson, and Dr. Roderick Heelis. The committee members provided very useful comments on the proposal and dissertation defenses and papers. Their kind words and support have made my memories of the proposal and dissertation defenses great ones. Outside of being wonderful instructors, Dr. King, Dr. Ishak, Dr. Anderson, and Dr. Heelis have made me laugh in times of stress before my defenses, which I appreciate immensely. Also Dr. Anderson was a very helpful graduate advisor, and showed interest in my progress and future and used examples in his own life to help me with mine. Dr. King, Dr. Kesden, Dr. Ishak, and Dr. Kaloyan Penev host group meetings which have expanded my knowledge on the many interesting topics within the large umbrella of Cosmology and Astrophysics. Without them my education would be lacking in context and general knowledge of so many other fields under this umbrella. I'd also like to give a special thanks to Dr. Kesden, who is the smartest person I have ever met and is awesomely conscious of others. When discussions get deep or technical, he is always aware of the others in the room, where most students are afraid to ask questions or don't know what questions to ask. Before people are completely lost in the conversation, Dr. Kesden makes sure that everyone is on the same page by providing the most clear and insightful explanations that we students don't thank him enough for. The journey to completing my PhD has been the most fulfilling experience of my life. I have learned so much and had a lot of fun along the way. This is especially true because of my advisor, Dr. Lindsay King. She is the kindest, most down-to-earth person I have ever met. That along with her deep knowledge in the field and seemingly endless patience, creates an environment where people are unafraid to ask questions. When she does answer your questions she takes particular care in making sure you understand the steps to get from your current understanding to the solutions. She is a wonderful teacher and her passion on the topic shines through by her

excited and captive explanations. She always pushes me to do more, especially when it comes to working with others. Because of her I got to see how much care should go into others' education and how you should relate to them to create a more comfortable environment to learn. She has been more than an advisor to me, but also a really cool, fun, and overall great mentor. I have learned so much more from her that typing it all out would produce more pages than this dissertation. I would like to let her know that I truly appreciate the time she has given me, because without it I wouldn't be who I am today in a big way. In times of insecurity she guided me from the source of the insecurities, building up my knowledge and understanding. She helped me find confidence in myself and with what comes next. Without her mentorship I would not be as excited for the future as I am.

April 2019

THE STRUCTURE AND ENVIRONMENT
OF GALAXY CLUSTERS IN SIMULATIONS
AND OBSERVATIONS

Matthew W. Fong, PhD
The University of Texas at Dallas, 2019

Supervising Professor: Lindsay J. King, Chair

Galaxy clusters are powerful testing grounds for cosmology. They are the largest, most massively bound objects in the Universe and can give us deep insights on how baryons, dark matter, and dark energy impacts on the formation of large scale structure in the cosmos. In this dissertation we study the structure and environment of clusters, how neutrinos impact on cluster masses, and how we may find them.

We study cluster profiles on large scales to gain better understanding on the relationship between cosmic web filaments and clusters that reside in the nodes, which gives insight on the evolution of clusters from their environment. For more than two decades, the Navarro, Frenk, and White (NFW) model has stood the test of time; it is used to describe the distribution of mass in galaxy clusters out to their outskirts, beyond which the NFW model is no longer applicable. In this dissertation we assess how well the parameterised Diemer & Kravstov (DK) mass density profile describes the mass distribution of galaxy clusters extracted from cosmological simulations. This is determined from averaged synthetic lensing measurements of the 50 most massive clusters extracted from the OverWhelmingly Large Simulations (Cosmo-OWLS). The characteristics of the data reflect the Weighing the Giants survey and data from the future Large Synoptic Survey Telescope (LSST). In comparison

with the NFW model, the DK model is favored by the averaged data, in particular for the LSST data, where the number density of background galaxies is higher. The DK profile depends on the accretion history of clusters which is specified in the current study. Eventually subsamples of galaxy clusters with qualities indicative of disparate accretion histories could be studied.

We also study the impact of baryonic processes and massive neutrinos on weak lensing (WL) peak statistics that can be used to constrain cosmological parameters. We use the BAHAMAS suite of cosmological simulations, which self-consistently include baryonic processes and the effect of massive neutrino free-streaming on the evolution of structure formation. We construct synthetic WL catalogues by ray-tracing through light-cones, and use the aperture mass statistic for the analysis. The WL peaks reflect the cumulative signal from massive bound objects and general large-scale structure. We present the first study of WL peaks in simulations that include both baryonic physics and massive neutrinos, so that the uncertainty due to physics beyond the gravity of dark matter can be factored into constraints on cosmological models. Assuming a fiducial model of baryonic physics, we also investigate the correlation between peaks and massive haloes, over a range of neutrino masses. As higher neutrino mass tends to suppress the formation of massive structures in the Universe, the halo mass function and lensing peak counts are therefore modified as a function of neutrino mass. Over most of the $S/N \lesssim 5$, the impact of fiducial baryonic physics is greater (less) than neutrinos for 0.06 and 0.12 (0.24 and 0.48) eV models. Both baryonic physics and massive neutrinos should be accounted for when deriving cosmological parameters from weak lensing observations.

TABLE OF CONTENTS

ACKNOWLEDGMENTS	iv
ABSTRACT	vi
LIST OF FIGURES	x
LIST OF TABLES	xviii
CHAPTER 1 INTRODUCTION	1
1.1 Cosmology	1
1.2 Constraining the Mass at the Outskirts of Galaxy Clusters	4
1.3 Neutrinos and Baryonic Physics in Structure Formation	6
1.4 Shapes of Galaxy Clusters	10
1.5 Contents of this Dissertation	11
CHAPTER 2 WEAK GRAVITATIONAL LENSING	13
2.1 Brief Weak Lensing Introduction	13
2.2 Mass Density Models	18
2.3 Gravitational Shear for the NFW and DK Models	20
CHAPTER 3 SIMULATIONS	27
3.1 Cosmo-OWLS	27
3.2 BAHAMAS	28
CHAPTER 4 GENERATION OF SYNTHETIC GRAVITATIONAL LENSING GALAXY CATALOGUES	31
4.1 Mock Catalogues from Cosmo-OWLS	31
4.2 Synthetic Weak Lensing Catalogues from BAHAMAS light-cones	33
CHAPTER 5 STUDYING THE DISTRIBUTION OF MASS AT THE OUTSKIRTS OF CLUSTERS USING COSMO-OWLS	37
5.1 Stacking Cluster Signals Without Scaling	37
5.2 Stacking Cluster Signals With Scaling	39
5.3 Fitting Method	40
5.3.1 Parameterized Mass Model Fits	41
5.3.2 Extreme Galaxy Clusters in Cosmo-OWLS	42

5.4	Ideal DK Lensing Data Sets	46
5.5	Stacking Without Scaling for AGN 8.0 Cluster Lensing Data	50
5.6	Impact of Uncorrelated Large Scale Structure	54
5.7	Application of Stacking Without Scaling to Extended Field-of-View WtG-like Data	56
5.8	Splashback Radius	59
5.9	DK Mass Density and Stacking Conclusions	61
CHAPTER 6 THE IMPACT OF MASSIVE NEUTRINOS AND BARYONIC PHYSICS ON WEAK LENSING PEAK STATISTICS		64
6.1	Aperture Mass Statistic	64
6.2	S/N Peaks	66
6.3	Dependence of Weak Lensing Peak Counts on Baryonic Physics and Summed Neutrino Mass	69
6.4	High S/N Weak Lensing Peaks	74
6.4.1	Noise Realisations	76
6.4.2	Filter Sizes	77
6.4.3	Summed Neutrino Mass and S/N vs. Cluster Mass	77
6.4.4	Summary of Weak Lensing Peak Statistics for Varying Survey Characteristics	79
6.5	S/N Peak Conclusions	81
CHAPTER 7 CURRENT AND FUTURE WORK		96
7.1	Cluster Shapes	96
7.2	Other Future Work	106
REFERENCES		109
BIOGRAPHICAL SKETCH		125
CURRICULUM VITAE		

LIST OF FIGURES

2.1	Diagram of lens geometry. β is the angular position of the source, θ is the angular position of the source image, and $\hat{\alpha}$ is the deflection angle. The distances are from the observer to the lens or deflector plane, the lens plane to the source plane, and from the observer to the source plane, D_d , D_{ds} , and D_s respectively. η and ξ are the distances from the center of the source plane to the source and from the center of the lens plane to the source image, respectively. From Schneider et al. (1992).	14
2.2	Diagram of lensing distortion for a circular source. The circular source shown on the left is distorted by a lens, which we observe on the right. In the absence of shear, the isotropically magnified image, shown on the top right, depends on the convergence. When both convergence and shear are present, the stretched image appearance, shown on the bottom right, depends on both the convergence and shear. φ is the direction of the distortion image with respect to the field-of-view.	15
2.3	For NFW and DK, the upper, middle, and lower panels compare the 3D mass density, convergence, and shear profiles respectively. The DK profile is the solid blue curve, the NFW is the dashed orange curve, and $r_{200c} = 1.41 Mpc$ is the solid green vertical line. In this example we use typical values of $M_{200c} = 5 \times 10^{14} M_\odot$ and $c = 4$ to illustrate that the DK and NFW profiles are a good match out to the virial radius.	22
2.4	The top panel here shows the shear forms (scaled shear) for the NFW and DK profiles for a wide range of parameters. The dashed red curve is the NFW form, $f^{NFW}(x)$, the solid curves are the DK forms, f^{DK} , and the dashed vertical line a outer fit radius of 2.3 Mpc ($r_s \approx 0.38$ Mpc). The range of parameters plotted are $2.0 < M_{200c}[10^{14} M_\odot] < 17.4$ and $2.5 < c < 5.5$. The NFW form is self-similar so for any parameters the form will lie on the dashed curve, however the DK form varies with mass and concentration. The bottom panel measures the difference between the NFW and DK forms. The dashed horizontal line represents the difference between the NFW form to itself ($y = 0$), and the other lines are the difference between the DK forms and NFW form. Most of parameters used in these panels are quite extreme, where a more typical mass and concentration ($M_{200c}[10^{14} M_\odot] = 5.0$, $c = 4.0$) is highlighted by a thick black dashed curve. To the left of the dashed vertical line, the DK forms are nearly self-similar for more typical mass ranges used in this chapter. This shows that, though the DK and NFW forms differ quite significantly for large radii, for typical present day weak lensing fit ranges the DK and NFW forms nearly agree with one another for more typical masses and concentrations we use in this work.	24

2.5	The solid and the dashed lines are the DK and NFW ideal reduced shear profiles respectively. Though the profiles are similar for the typical average parameters used in this dissertation, we show that for higher mass bins there are deviations when varying concentration. The mass of these clusters is $M_{200c} = 1 \times 10^{15} M_{\odot}$ with concentrations 3, 4, and 5, from bottom to top. Six of the 50 clusters used in this dissertation are more massive than this example.	25
5.1	The red squares and blue points values plotted here are the DK and NFW mass estimates respectively versus the true masses from the simulation. The green dotted line is $y = x$. In this example, we consider the run with AGN 8.0 for LSST-like surveys and for the 50 most massive clusters in the sample. This shows that the DK fits prefer a lower mass estimate than that of the NFW. This trend is similar with other runs.	43
5.2	This plot is using the same data as Figure 5.1. The green dashed line is $y = x$ and the blue points with error bars are the DK vs. NFW fit mass estimates. For the lower mass clusters (of the 50 most massive clusters in the simulation), the DK and NFW masses are in agreement. For higher masses, their estimates begin to diverge, showing that for the highest mass clusters DK mass estimates are lower than the NFW.	44
5.3	This figure is over the same run as Figures 5.1 and 5.2. The NFW and DK fit parameters are marked by larger circles and smaller points respectively, where each cluster fit results are connected by lines of the same colour. Differences in fits in the x or y-directions reflects on the difference in estimates for mass and concentrations respectively. This plot shows that the NFW and DK profiles agree with mass and concentration estimation for lower mass bins (of the 50 most massive clusters) and the DK profile prefers a lower mass for higher mass bins, preferring higher concentrations to compensate. Also it looks like the DK profile generally prefers in a lower mass than the NFW throughout this cluster sample, though that is not always true in general.	45
5.4	κ map of a simulated cluster in xy projection overlaid with a vector representation of the cluster axes in projection. The κ map is zoomed into a radius of 5 Mpc. The arrows labelled 1, 2, and 3 represent the major, intermediate, and minor axes respectively. The axes have been scaled according to their respective eigenvalues. Though longest in 3D space, the major axis appears shortest in projection because it lies in a similar direction to the line of sight (z axis). This leads to a large error in mass estimation when using a spherical model.	47
5.5	Stack without scaling (Section 5.1) for ideal DK haloes. The green points are $\langle \Delta \Sigma(R) \rangle$ (stack without scaling) scaled by $2\rho_c r_s$ (determined by fitting onto the stack), to compare with $F(x)$. The corresponding error bars is $\sigma_{(\epsilon)}$. The thick black curve is $F^{DK}(x, \vec{\pi})$ (DK form) and, for reference, the red curve is $F^{NFW}(x)$ (NFW form). This shows that stack without scaling for ideal DK haloes is well represented by the DK form.	48

5.6	stack with scaling ($\langle F(x) \rangle$, Section 5.2) for ideal DK haloes. The green points are $\langle F(x) \rangle$ with the corresponding error bars $\sigma_{\langle F(x) \rangle}$. Even with ideal DK haloes, stack with scaling is not well represented by the DK form. This is likely due to the bias in parameter estimation that is needed for $\langle F(x) \rangle$ and parameter dependency in the DK form (i.e., each signal that goes into stack may have different concentrations and therefore different profile shapes, see Section 2.3). The parameters used in the DK form is determined by fitting over the stack without scaling (Figure 5.5).	49
5.7	Each thin curve represents a cluster's reduced shear that went into the stack, the thick green curve represents the stack without scaling, and the thick red curve is the NFW form, $F^{\text{NFW}}(x)$. Everything is then scaled using the best fit parameters onto the stack, to compare with $F(x)$. Here we follow Section 5.1 with the 50 most massive clusters with no noise. For simplicity, we omitted error bars to show individual signals compared to the stack without scaling. This plot is an example of how stack without scaling compares with each individual cluster shear profile and the NFW form.	52
5.8	This plot uses realistic LSST-like clusters from the AGN 8.0 simulation. The green points are $\langle \Delta\Sigma(R) \rangle$ (stack without scaling, following Section 5.1), scaled by $(2\rho_c r_s)^{bf}$ (so we can compare with $F(x)$) with error bars of $\sigma_{\langle \epsilon \rangle} / (2\rho_c r_s)^{bf}$ (Equation 5.5). The thick black curve is the DK form, $F^{DK}(x, \vec{\pi})$, and the red curve is the NFW form, $F^{\text{NFW}}(x)$. It is clear that the stack is better represented by DK than NFW. The DK $\chi_{red}^2 = 1.08$ with $d.o.f. = 64 - 2$.	53
5.9	This plot uses realistic LSST-like clusters from the AGN 8.0 simulation but with added noise approximating that due to Large Scale Structure (σ_{LSS}). The green points are $\langle \Delta\Sigma(R) \rangle$ (stack with scaling, following Section 5.1), scaled by $(2\rho_c r_s)^{bf}$ (so we can compare with $F(x)$) with error bars as $\sigma_{\langle \epsilon \rangle} / (2\rho_c r_s)^{bf}$ (Equation 5.5) and $\sigma_{LSS} / (2\rho_c r_s)^{bf}$ added in quadrature. The thick black curve is the DK form, $F^{DK}(x)$, and the red curve is the NFW form, $F^{\text{NFW}}(x)$. It is clear that the stack is better represented by DK than NFW. The added noise is extremely crude (flat $\sigma_{LSS} = 0.004$), but is included in this plot to show the difficulty in distinguishing between the DK and NFW forms when Large Scale Structure is considered.	55
5.10	Here we plot stack without scaling ($\langle \Delta\Sigma(R) \rangle$, following Section 5.1) in green for a WtG-like run for the AGN 8.0 simulation using the 50 most massive clusters. The thick black and red curves are $F^{DK}(x, \vec{\pi})$ and $F^{\text{NFW}}(x)$, the DK and NFW forms, respectively. This shows that with a smaller number density of background galaxies, n_0 , the more difficult it is to distinguish between the NFW and DK forms (Compare with Figure 5.8, where the number density is $n_0 = 30$ gals/arcmin ²). So in order to distinguish, we either need to increase the number of sources or include more cluster signals.	58

5.11	This figure is the same as Figure 5.10 but with 300 (as opposed to 50) of the most massive clusters from the AGN 8.0 simulation for a WtG-like run ($n_0 = 10$ gals/arcmin ²). $\langle M_{200c}^{3D} \rangle = 3.30 \times 10^{14} M_\odot$ with $1.97 < M_{200c}^{3D} [10^{14} M_\odot] < 17.35$. This figure shows the results for a larger number of clusters with a much larger mass range, where χ_{red}^2 are 0.97 and 1.33 for DK (<i>d.o.f.</i> = 64 – 2) and NFW (<i>d.o.f.</i> = 64) respectively.	60
5.12	The splashback radius of the DK profile using M_{200c}, c, s_e, b_e fit parameters onto $\langle \Delta \Sigma(R) \rangle$ (stack without scaling, following Section 5.1) for realistic LSST-like clusters from the AGN 8.0 simulation Cosmo-OWLS (see Section 5.5, Figure 5.8, and Table 5.1). Plotted in the top, middle, and bottom panels are the exponential behavior of r for $\rho, \Sigma,$ and g respectively. The dashed green line is the DK profile using the fit parameters and the solid green line is the NFW profile for reference. The Red dashed vertical line is the truncation radius $r_t = 3.02$ Mpc and the vertical black solid lines are the minimum of the exponential behavior of r for each panel. The true r_{sp} is the minimum of the DK mass density profile (top panel), which is 2.72 Mpc. The middle and bottom panel minima are located at 1.80 and 6.20 Mpc respectively.	62
6.1	$Q_{NFW}(x)$ is the aperture mass filter function used in this work (Equation 6.5), taken from Schirmer et al. (2007). The aperture mass calculated in Equation 6.3 cuts off at the filter size, $\theta = \theta_{ap}$ and the falloff towards the centre down-weights the bright central galaxy and the strong lensing regime.	66
6.2	A 60×60 arcmin ² sub-region of a 5×5 deg ² aperture mass map for source number density 9 gal/arcmin ² . The aperture size is 12.5 arcmin, and the S/N contour lines are plotted from 0 with an increment of 1. The field in grey scale in the background is the original BAHAMAS convergence map, and the cross marks are the locations of clusters from the BAHAMAS friends-of-friends catalogues, where the lowest mass cut is $10^{14} M_\odot$ and the upper limit redshift cut is at $z=0.5$. The triangles are the peak locations above S/N=2.	68
6.3	The S/N peak counts for the different baryonic physics prescriptions and the DMONLY case, all without massive neutrinos. The bottom panel shows the $\ln(RoM)$ compared to the DMONLY peak count.	70
6.4	The S/N peak counts with varying summed neutrino mass, all with fiducial baryonic physics prescription, for DGB data. The bottom panel shows the $\ln(RoM)$ compared to the zero summed neutrino mass peak count.	71

6.5	The impact of different cosmologies (<i>WMAP</i> 9 and <i>Planck</i> 2015) on the weak lensing peak statistics with aperture filter size fixed at 12.5 arcmin. The number densities shown here are 9 and 30 gal/arcmin ² , corresponding to KiDS and DGB respectively. The bottom panels show the $\ln(RoM)$ compared to <i>WMAP</i> 9 with fiducial AGN feedback and the error bars show the variance of the five different shape noise realisations. The dashed horizontal line shows where the ratio is unity. Note that we exclude the <i>WMAP</i> 9 $M_\nu = 0.48$ eV model as it is well outside of the range of the <i>Planck</i> 2015 models (see Figure 6.4). All of the models have fiducial baryonic physics.	85
6.6	Relative percentage differences in peak counts with respect to the DMONLY peak count distribution (Figure 6.4). For the DGB survey, five models ($M_\nu = 0.00, 0.06, 0.12, 0.24,$ and 0.48 eV, all with fiducial baryonic physics) of the <i>WMAP</i> 9 cosmology are compared with the DMONLY model in order to determine percentage differences in each interval of S/N.	86
6.7	The cluster counts as a function of mass for different summed neutrino mass runs. The solid, dotted, dash-dotted, and dashed lines correspond to M_ν [eV] = 0.06, 0.12, 0.24, and 0.48. These results are for $\theta_{ap} = 12.5$ arcmin, and $n_{eff} = 9$ gal/arcmin ² . The bottom panel shows the ratio of the number counts between the different massive neutrino simulations in comparison with the 0.06 eV model.	87
6.8	The locations of clusters on the convergence maps for different summed neutrino mass. This is the same field-of-view for four different simulations in the <i>Planck</i> 2015 cosmology with $n_{eff} = 9$ gal/arcmin ² . The four panels have M_ν [eV] = 0.06, 0.12, 0.24, and 0.48 for the top left, top right, bottom left, and bottom right panels respectively. The grey scale is the convergence map and \times s are the cluster locations. The smaller the \times the higher the cluster redshift. The values next to the \times s are the cluster masses in units of $10^{14} M_\odot$	88
6.9	The correspondence between the locations of S/N peaks and massive dark matter haloes for four sets of shape noise realisations for KiDS and DGB surveys. The grey scale is the convergence map, the line contours are the S/N of the aperture mass map, triangle markers are the S/N peaks, and \times markers are cluster locations from the halo finder catalogue. A smaller triangle or \times corresponds to a lower S/N peak value or a higher cluster redshift, respectively. All four panels show the same field-of-view (1×1 deg ²) with the <i>Planck</i> 2015 cosmology and $M_\nu = 0.06$ eV.	89
6.10	The distribution by S/N for various aperture sizes for KiDS and DGB, top and bottom panels respectively. The lines represent $\theta_{ap} = 8.0, 10.0, 12.5,$ and 15.0 arcmin. The top sub-panels show the S/N distribution while the bottom sub-panels show the logarithmic ratio of means for the distributions relative to $\theta_{ap} = 12.5$ arcmin. The error bars show the variance of the five different shape noise realisations.	90

6.11	The S/N peaks vs. M_{200c} for different summed neutrino mass for KiDS and DGB (left and right panels respectively). The different sub-panels correspond to different summed neutrino mass M_ν [eV] = 0.06, 0.12, 0.24, and 0.48. This shows the S/N peaks closest to the cluster centres. The points are the S/N values plotted against cluster mass, while the line shows the mean S/N in logarithmic mass bins. The Pearson Correlation Coefficient (PCC) is calculated for each sub-panel (see text for details). The PCC values for each sub-panel are (M_ν, PCC) , for KiDS: (0.06 eV, 0.28), (0.12 eV, 0.30), (0.24 eV, 0.30), (0.48 eV, 0.31); and for DGB: (0.06 eV, 0.46), (0.12 eV, 0.46), (0.24 eV, 0.46), (0.48 eV, 0.49). . . .	91
6.12	The S/N peaks vs. M_{200c} in different redshift bins for KiDS and DGB (upper and lower panels respectively). The points are the S/N peak values (≥ 3) closest to the massive objects; the lines are the average of the S/N values in logarithmic mass bins and the error bars show the variance (note that there is a limit at S/N = 3). This plot is for $M_\nu = 0.06$ eV. The Pearson Correlation Coefficient values are (z_{bin}, PCC) , for KiDS: ([0.1, 0.2], 0.63), ([0.2, 0.3], 0.67), ([0.3, 0.4], 0.43), ([0.4, 0.5], 0.24), ([0.5, 0.6], 0.04), ([0.6, 0.7], -0.05), ([0.7, 0.8], -0.03), ([0.8, 0.9], -0.06); and for DGB: ([0.1, 0.2], 0.67), ([0.2, 0.3], 0.71), ([0.3, 0.4], 0.64), ([0.4, 0.5], 0.56), ([0.5, 0.6], 0.36), ([0.6, 0.7], 0.31), ([0.7, 0.8], 0.15), ([0.8, 0.9], 0.04). . . .	92
6.13	The high S/N peak distribution for $n_{\text{eff}} = 9, 30, \text{ and } 60$ gal/arcmin ² (dashed, solid, and dash-dotted curves respectively).	93
6.14	The fraction of clusters that have an associated S/N peak as a function of cluster mass. Source number densities $n_{\text{eff}} = 9, 30, \text{ and } 60$ gal/arcmin ² are represented by the dashed, solid, and dash-dotted curves, respectively.	94
6.15	The fraction of S/N peaks (≥ 3) that have a nearby cluster within radius $\theta_{\text{ap}} = 12.5$ arcmin, for different galaxy number densities $n_{\text{eff}} = 9, 30, \text{ and } 60$ gal/arcmin ² (represented by the dashed, solid, and dash-dotted curves, respectively).	95
7.1	This shows, for 66 simulated clusters, how many true 3D major, intermediate, and minor axis are aligned with the projected major axis.	97
7.2	This shows stacked kappa maps for clusters without any orientation adjustments. The clusters here are extracted with line-of-sight along the z-direction, all sharing common x and y-hat directions. The blue, red, and yellow arrows represent the projected 3D major, intermediate, and minor axes of the moment of inertia of the cluster, respectively, where the 3D lengths are normalized to the radius of the circle. The longer the arrow, the smaller the angle between the axis and the lens plane, or x and y-hat directions. The stacked kappa maps here look spherical, as we'd expect.	98

7.3	This shows stacked kappa maps for clusters while aligning their true 3D major axis. The blue, red, and yellow arrows represent the projected 3D major, intermediate, and minor axes of the moment of inertia of the cluster, respectively, where the 3D lengths are normalized to the radius of the circle. The longer the arrow, the smaller the angle between the axis and the lens plane, or x and y-hat directions. The clusters are similar to Figure 7.2, but with their orientation angle set to zero. The stack shows a stronger signal along the x-axis, where we'd expect a stronger shear signal. Using the shear signal along this axis, we may get better insight on how clusters are related to filaments.	99
7.4	These plots show the pixel distance, to a contour value of 0.2, against the angle starting from the x-axis. For the left panel, this shows that the stack kappa drops to 0.2 at almost a constant pixel distance from the center. For the right panel, this shows that the stack kappa drops to 0.2 further out for the angles along the x-direction as opposed the the others.	100
7.5	These plots show the aperture mass signal-to-noise maps of the same cluster, but with different aperture mass sizes. The left panel shows an aperture size of 10 arcmin while the right shows 5 arcmin. If an ellipse is applied to these maps, we may obtain slightly different orientation angles. So we will need to study how aperture sizes effects the shape and orientation of the maps. This can be done by comparing the orientations to the true orientation values found in Rachel's work.	100
7.6	This plot shows an example of ellipse orientation fit results for 10 S/N band for a particular cluster (FoF ID 6). The orientation results vary depending on which S/N band is used. Note that the S/N values are very large in this example because we are using ideal shear in this example and not adding any shape noise to the ellipticities before calculating the aperture mass, or S/N map.	101
7.7	A comparison of the orientation angles (colors corresponding to the 10 S/N bands, See Figure 7.6) and the true projected major, intermediate, and minor axis of the ellipsoid of the cluster, determined from the moment of inertia (FoF ID 6). In this case most ellipse orientations do not agree with the projected major axis.	102
7.8	The median angular separation, between the orientation angle and the projected major axis for the 10 rings, for the most massive clusters. All S/N rings on average have similar orientation predictability.	103
7.9	The contours are the lines of constant distribution density of a/c vs. b/c distributions for varying summed neutrino mass (eV). The values plotted are the contour values.	104

7.10	An example 3D map of the triaxial NFW density. Plotted here is a small band of density for the triaxial NFW model, shown in blue dots. Projecting the points along the Z'_{los} -direction gives an idea of how the convergence shape should appear on the $X'_{\text{los}}-Y'_{\text{los}}$ plane, shown as orange dots. The dashed lines are the X'_{los} , Y'_{los} , and Z'_{los} the line-of-sight orthogonal coordinates, and the solid lines are the minor, intermediate, and major axis of the triaxial halo, x_{min} , y_{int} , and z_{maj} respectively. The parameters M_{200c} , c , a , b , θ , ϕ are the triaxial NFW parameters. M_{200c} and c are the NFW mass and concentration, a and b are the minor and intermediate axes scaled by the major axis, θ is the angle between Z'_{los} and z_{maj} , and ϕ is the angle between the projected Z'_{los} (onto the $x_{\text{min}}-y_{\text{int}}$ plane) and $-X'_{\text{los}}$, where X'_{los} is constrained to be in the $x_{\text{min}}-y_{\text{int}}$ plane.	105
7.11	The convergence of the triaxial NFW halo shown in Figure 7.10.	106
7.12	The reduced shear of the triaxial NFW halo shown in Figure 7.10.	107

LIST OF TABLES

3.1	Cosmological parameter values for 12 suites of the BAHAMAS simulations (McCarthy et al., 2017, 2018). Adjustments on the summed neutrino mass, baryonic matter fractions, AGN feedback temperatures, σ_8 values, and changes in S_8 are given in this table. The columns are: (1) The summed mass of the 3 active neutrino species (we adopt a normal hierarchy for the individual masses); (2) the logarithm to base 10 of the AGN feedback temperature defined by McCarthy et al.; (3) the total matter density; (4) present-day baryon density; (5) present-day dark matter density; (6) present-day neutrino density, computed as $\Omega_\nu = M_\nu/(93.14 \text{ eV } h^2)$; (7) present-day (linearly-evolved) amplitude of the matter power spectrum on a scale of $8 \text{ Mpc } h^{-1}$ (note that we use A_s rather than σ_8 to compute the power spectrum used for the initial conditions, thus the initial conditions are CMB normalised); (8) $S_8 = \sigma_8\sqrt{\Omega_m/0.3}$	30
5.1	Ratios for DK and NFW profile, $\chi_{red}^2/\overline{\chi_{red}^2}$, for the LSST-like runs for AGN 8.0 and DMO simulations. In this section we only have M_{200c} and c as the free parameters for the DK form and we used 64 radial bins for the analysis ($d.o.f. = 64 - 2$). The NFW form doesn't have parameters, so the $d.o.f. = 64$ for NFW. The average χ_{red}^2 values for stack without scaling, $\langle\Delta\Sigma(R)\rangle$, for the ideal DK and NFW halo runs with LSST-like noise are $\overline{\chi_{red}^2} = 1.06$ and 1.26 respectively. The $\overline{\chi_{red}^2}$ values are calculated over eight LSST-like runs but over ideal DK or NFW haloes. . .	51
5.2	Ratios for DK profile, $\chi_{red}^2/\overline{\chi_{red}^2}$, for the LSST-like runs for AGN 8.0 and DMO simulations. This table is similar to Table 5.1 but with Large Scale Structure noise $\sigma_{LSS} = 0.004$. The average χ_{red}^2 values for stack without scaling, $\langle\Delta\Sigma(R)\rangle$, for the ideal DK and NFW halo runs with LSST-like noise are $\overline{\chi_{red}^2} = 0.57$ and 0.51 respectively. The $\overline{\chi_{red}^2}$ values are calculated over eight LSST-like runs. . . .	54
5.3	Ratios for DK and NFW profile, $\chi_{red}^2/\overline{\chi_{red}^2}$, for the WtG-like runs for AGN 8.0 and DMO simulations. The DK form has $\vec{\pi}$ as the free parameters and uses 64 radial bins for the analysis, so the $d.o.f. = 64 - 2$. The NFW form does not have any parameters in the form, so the $d.o.f. = 64$. The average χ_{red}^2 values for stack without scaling, $\langle\Delta\Sigma(R)\rangle$, for the ideal DK and NFW halo runs with WtG-like noise are $\overline{\chi_{red}^2} = 1.04$ and 1.13 respectively. The $\overline{\chi_{red}^2}$ values are calculated over eight WtG-like runs but over ideal DK or NFW haloes.	57
5.4	Ratios for DK profile, $\chi_{red}^2/\overline{\chi_{red}^2}$, for the WtG-like runs for AGN 8.0 and DMO simulations. This table is similar to Table 5.3 but with Large Scale Structure noise $\sigma_{LSS} = 0.004$. The average χ_{red}^2 values for $\langle\Delta\Sigma(R)\rangle$ for the ideal DK and NFW halo runs with WtG-like noise are $\overline{\chi_{red}^2} = 0.66$ and 0.65 respectively. The $\overline{\chi_{red}^2}$ values are calculated over eight WtG-like runs.	57

6.1 The relative percentage differences in S/N peak counts for the DGB survey (these values are taken from Figures 6.4 and 6.6). The values are in units of percent (%) and compare the five different simulations ($M_\nu = 0.0, 0.06, 0.12, 0.24,$ and 0.48 eV, all with fiducial baryonic physics) per S/N bin with the DMONLY simulation. 74

CHAPTER 1

INTRODUCTION

1.1 Cosmology

The study of cosmology and astrophysics tells a rich history of the Universe from its early beginnings to predictions of its fate. This is done by testing model predictions of different epochs against observational data and seeking to understand the physics of massive objects from asteroids in our solar system to the largest super clusters in the Universe. The prevailing cosmological model is Λ CDM (Λ Cold Dark Matter), which is consistent with a broad range of astrophysical observations, such as the Cosmic Microwave Background (CMB), type Ia supernovae, Baryon Acoustic Oscillations (BAO), and gravitational lensing. As outlined below, most of the matter is cold and dark and observations cannot be explained by just matter, since the expansion of the Universe is accelerating. Observations are consistent with the presence of a cosmological constant (Λ), however other alternatives such as models of modified gravity are also being explored.

When we observe light from a distant object we are looking into the past, due to the finite speed of light. The CMB is the earliest electromagnetic radiation in the Universe that we can observe today, which was predicted in 1948 by Ralph Alpher and Robert Herman (Alpher and Herman, 1948). The CMB gives us a temperature and polarization map of our sky at the recombination epoch that shows small differences in temperature, which reflects the matter density fluctuations at that time (Hu, 2001; Hu and Dodelson, 2002; Hinshaw et al., 2013; Planck Collaboration et al., 2018). This describes an early Universe that is hot, dense, and nearly uniform. As the Universe expands and cools, the small density fluctuations in the early Universe eventually evolve to large bound structures such as a large collection of galaxies, called galaxy clusters, which we observe today. In the Millennium N-body Simulation, Springel et al. (2005) show the 3D evolution of DM from early fluctuations to

today. The structure of the DM distribution is commonly called the cosmic web, where the web filaments feed into nodes, the intersections of filaments. The center of these nodes are where galaxy clusters grow.

In 1912 Vesto Slipher recorded the first receding velocity of a spiral nebula (Slipher, 1913), which today we know are galaxies. Afterward he wrote a series of papers on receding spiral galaxies that were critical to our understanding of the expanding Universe. Later in 1929 Hubble compared the relative radial velocities of galaxies to their distances from us (Hubble (1929)). This was the first analysis showing that galaxies that are farther away from us move away from us more quickly, and lead to the discovery that our Universe is expanding. Further work done on the radial velocities of supernovae tells us that the Universe is undergoing accelerated expansion, where a possible source of the acceleration is Dark Energy. In 1933 Fritz Zwicky studied of velocities of galaxies bound to the Coma Cluster (Zwicky (1937)). He found that the observed luminous mass was not nearly enough to keep the fast moving galaxies bound to the cluster, to which he concluded that the bulk matter is dark. Further studies found that all clusters have an abundance of dark matter. With the advent of X-ray satellites it was realised that most of the normal luminous mass in galaxy clusters is in the form of plasma. Even so about 5 to 10 times as much mass is required to be dark matter as compared with luminous matter. These studies deduce that the Universe is not only made of baryonic matter, what makes up all luminous matter, planets, and black holes, but also dark energy and dark matter. Today the energy density of the Universe is thought to be approximately 5% baryonic matter, 25% dark matter, and 70% dark energy (Hinshaw et al., 2013; Planck Collaboration et al., 2018).

In this work we study galaxy clusters, the most massive bound structures in the Universe. Most of the mass of clusters is thought to be cold dark matter, where about 1/8th of the mass is X-ray emitting plasma and only a couple of percent is in the form of stars in cluster galaxies (Allen et al., 2011). Because these massive structures house many different processes, they

are interesting laboratories for cosmological studies. As most of the mass of clusters is dark, the mass profiles are not only dependent on baryonic processes, but heavily dependent on the properties of DM. In [Spergel and Steinhardt \(2000\)](#) for example, it is shown that observations are consistent with DM being cold. Constraints can also be put on the DM interaction cross section (e.g., [Spergel and Steinhardt, 2000](#); [Randall et al., 2008](#)). Furthermore, the number of clusters as a function of mass and redshift, called the cluster mass function, depends on the properties of dark energy and mass density fluctuations of the Universe ([Wen et al., 2010](#)). The cluster mass function is sensitive to Ω_m and σ_8 (defined below), and is a useful tool in constraining those parameters. Ω_m is the fraction of dark and baryonic matter over the critical density of the Universe while $\Omega_0 = \Omega_m + \Omega_\Lambda$ is the density parameter, where Ω_Λ is the dark energy content over the critical density. The critical density is an important parameter to compare to because it tells us the eventual fate of the Universe. In the absence of the cosmological constant ($\Lambda = 0$) where $\Omega_0 = \Omega_m$, when $\Omega_0 < 1$ the Universe is open and will expand forever, $\Omega_0 = 1$ the Universe is flat and will halt in its expansion at infinite time, and $\Omega_0 > 1$ the Universe is closed and will eventually recollapse. Current studies show that $\Omega_m \approx 0.3$ and $\Omega_0 \approx 1$ ([Hinshaw et al., 2013](#); [Planck Collaboration et al., 2018](#)). σ_8 is the dispersion of density fluctuations on the scales of $8h^{-1}$ Mpc. The mass fluctuations in the early Universe gave birth to the large structures that we see today, so the properties of the perturbations greatly influence the number count of the objects those perturbations gave birth to. As clusters are important in our Universe today, we look at fluctuations on scales $8h^{-1}$ Mpc box, which are characteristic cluster scales.

The masses of clusters can be determined by measuring X-ray emissions of the intracluster medium (ICM), the radiation of energetic gas at the center of clusters; the Sunyaev Zel'dovich (SZ) effect, the inverse Thomson scattering of the CMB photons; gravitational lensing, the distortion of light from background galaxy sources as it passes near to a cluster on the way to us. In our work we focus on gravitational lensing, particularly weak gravitational

lensing. In strong gravitational lensing there can be multiply imaged sources or giant arcs, with non-negligible magnification effects, that can directly provide useful constraints on the central regions of clusters. Weak gravitational lensing, however, does not result in multiple images, and the images are not obviously stretched or magnified. In this case a statistical approach is required to analyse background source populations and obtain information on the lensing cluster. In the weak lensing regime, mass measurements can be carried out by fitting parametric cluster mass models to distorted background galaxy shapes and orientations. Other non-parametric techniques can be used to reconstruct cluster mass maps and other statistics also quantify the lensing mass distribution.

Throughout this work we use the angular diameter distance, D_A , to determine distances from an object to us (Weinberg, 1972). The ratio, $D_A = \frac{L}{\theta}$, is of the object's true physical size, L , divided by the comoving transverse angular size as viewed from earth, θ . The line-of-sight comoving distance, D_C , is used to determine the distance from us to an object, where the distance to that object remains constant with epoch while the object moves with the expansion of the Universe. The distance between two objects at the same redshift, (transverse distance) for a flat Universe $\Omega_k = 0$, is $\delta\theta D_A$, where $\delta\theta$ is the separation distance on the sky. The angular diameter distance is the most commonly used distance for weak lensing.

1.2 Constraining the Mass at the Outskirts of Galaxy Clusters

One of the research goals of this dissertation is to test if we can eventually use weak gravitational lensing signals of clusters to deduce the mass density profiles at the outskirts of galaxy clusters, by fitting a parametric model. Navarro et al. (1997) (Hereafter referred to as NFW) discovered that haloes formed in Cold Dark Matter (CDM) simulations of structure formation are well described by a universal form of mass density profiles that is characterised by a scale radius and the concentration of mass (or equivalent parameters). Jing and Suto

(2000) found that about 70% of haloes formed in CDM simulations are well fit by this so-called NFW profile. The NFW profile is also found to be a good fit to cluster scale haloes in more recent analysis of gravitational lensing data from the fields of real galaxy clusters, away from the central regions that are dominated by brightest cluster galaxies (e.g., Umetsu et al., 2016). Variants on the NFW density profile that have slightly different behaviours, in particular in the inner and outer regions of clusters, have been found to better reproduce higher resolution haloes (e.g., Moore et al., 1999; Jing and Suto, 2002; Fukushige and Makino, 2001; Navarro et al., 2010).

In general, although cluster profiles are relatively simple and well described by the NFW model (with the caveat of setting aside complex mergers and cluster systems), nevertheless in their outskirts the large scale structure of filaments in the cosmic web and contributions from neighbouring clusters eventually become important. It has therefore long been recognised from simulations that eventually the NFW model ceases to be an accurate representation of the mass density. Formally the mass of an NFW halo diverges when integrated to infinity, and usually the NFW description is only applied out to the virial radius. The halo model formalism (see e.g., Cooray and Sheth, 2002, for a review) is often used as a prescription for these additional contributions beyond the single halo. Various works have used higher resolution simulations than were available at the time of Navarro et al. (1997) and modified the form of the NFW profile in the inner regions of haloes and/or added an extra contribution to the density in the outskirts of haloes (e.g., Navarro et al., 2004; Prada et al., 2006; Hayashi and White, 2008). Recently, using fits to cosmological simulations, Diemer and Kravtsov (2014) (hereafter referred to as DK) suggested a new parametric model that describes clusters and the structure in which they are embedded, with a dependency on the rate at which mass has been accreted. We return to a full description of this model in a later chapter. The advent of detailed wide field images of galaxy clusters, and surveys that will cover many thousands of square degrees of the sky, motivates a consideration of the accuracy with which mass can

be determined in the periphery of clusters, beyond the 1-halo term. [Umetsu and Diemer \(2017\)](#), adopting the DK model, described lensing constraints on the shape of the average mass profile of 16 massive galaxy clusters from the CLASH (Cluster Lensing and Supernova survey with Hubble) sample of [Postman et al. \(2012\)](#). In that work they found that although the DK model was slightly preferred compared with the NFW that the differences were not statistically significant.

We determined the average mass density profile of massive clusters by fitting to the azimuthally averaged synthetic lensing signal over many clusters from cosmological simulations; this process is called stacking. In practice this will help us understand how observed clusters relate to their 3D surroundings and act as a first step toward our future research goals. Stacked weak gravitational lensing can be used to show that the spherical NFW mass density profile does well in describing clusters out to the virial radius ([Niikura et al., 2015](#)). For larger scales we expect the spherical DK mass density profile to represent the stacked signals better than the NFW. In particular, as outlined above, we consider the parametric DK model since it is related to the cluster environment.

1.3 Neutrinos and Baryonic Physics in Structure Formation

The second main research topic of this dissertation investigates the impact of neutrinos and baryonic physics on galaxy cluster observables. Galaxy clusters and large-scale structure (LSS) provide a powerful laboratory to study the Universe (e.g., [Bond et al., 1980](#); [Blumenthal et al., 1984](#); [Voit, 2005](#); [Allen et al., 2011](#); [Kravtsov and Borgani, 2012](#)). Measurements of LSS help constrain cosmological parameters, independent from observations of the CMB and other probes.

Agreement between various astrophysical probes has provided strong evidence for a concordance cosmology, the Λ CDM model. However, recent high-precision measurements have suggested a tension in some of the parameter estimates. For example, some authors have

determined that local measurements of Hubble’s constant H_0 (73.48 ± 1.66 km/s/Mpc, [Riess et al. 2018](#)) disagree with the value derived from the joint analysis of CMB and BAO (67.4 ± 0.5 km/s/Mpc, [Planck Collaboration et al. 2018](#)). However some analyses have suggested that the discrepancy between the measurements is of low significance. For example, [Feeney et al. \(2018\)](#) developed a Bayesian hierarchical model of the distance ladder that finds a local H_0 value nearly identical to the *Planck* CMB measurement. Another tension that has been found by some studies is between measurements of Ω_m and of σ_8 (see for example the discussion in [McCarthy et al. 2018](#); [Planck Collaboration et al. 2018](#)).

Traditionally, simulations of cosmological structure formation have considered only collisionless gravitational dynamics. However, with the increase in computational capabilities, some large-volume simulations have now been carried out to model the LSS for various cosmologies and using various prescriptions for baryonic physics (e.g., [Dolag et al. 2009](#); [Schaye et al. 2010](#); [Vogelsberger et al. 2013](#); [Le Brun et al. 2014](#); [Schaye et al. 2015](#); [Dubois et al. 2014](#); [McCarthy et al. 2017](#); [Pillepich et al. 2018](#)). These and other simulations have shown that baryonic physics affects the total matter power spectrum (e.g., [van Daalen et al. 2011](#); [Schneider and Teyssier 2015](#)), the halo mass function (e.g., [Sawala et al. 2013](#); [Velliscig et al. 2014](#); [Cusworth et al. 2014](#)) and galaxy cluster mass density profiles and mass estimation (e.g., [Mummery et al. 2017](#); [Henson et al. 2017](#); [Lee et al. 2018](#)). For example, on galaxy and cluster scales baryonic feedback produces an outward pressure that acts against the infall of matter, resulting in a shallower inner density profile, corresponding to a lower concentration of mass ([Mummery et al. 2017](#)). These works have illustrated that the addition of baryons can have a significant impact on our measurements, and therefore on our inference of cosmological parameters.

Theoretical and observational studies of the impact of neutrinos on cosmological structure formation have been carried out by e.g., [Hu et al. \(1998\)](#); [Bashinsky and Seljak \(2004\)](#); [Hannestad et al. \(2006\)](#); [Gratton et al. \(2008\)](#); [Namikawa et al. \(2010\)](#); [Lahav et al. \(2010\)](#);

[Bird et al. \(2012\)](#); [Wagner et al. \(2012\)](#); [Costanzi et al. \(2013\)](#); [Villaescusa-Navarro et al. \(2014\)](#); [Castorina et al. \(2014\)](#); [Mummery et al. \(2017\)](#); [Moscardini et al. \(2018\)](#); [Hagstotz et al. \(2018\)](#). However, their mass is not yet known, and the relevance of massive neutrinos to structure formation and to astrophysical observables is an open question. [Lesgourgues and Pastor \(2006\)](#) found that the three active neutrino species have a summed mass of at least 0.06 eV for normal or inverted hierarchies, by studying atmospheric and solar oscillation experiments. In their fiducial analysis, [Planck Collaboration et al. \(2016a\)](#) adopt a value of $M_\nu = 0.06$ eV. The CMB data itself can be used to constrain the summed neutrino mass and, when combined with external BAO constraints, [Planck Collaboration et al. \(2016a\)](#) set an upper limit of $M_\nu < 0.21$ eV. However, the derived upper limit is sensitive to the treatment of internal tensions in the primary CMB data (e.g., [Addison et al. 2016](#); [Planck Collaboration et al. 2017](#)) and, when this is factored in, values of up to 0.4 eV are potentially compatible with the data (e.g., [Di Valentino et al. 2017](#); [McCarthy et al. 2018](#); [Poulin et al. 2018](#)).

Some studies find that the aforementioned tension in cosmological parameter measurements can potentially be remedied with the inclusion of massive neutrinos (e.g., [Wyman et al. 2014](#); [Battye and Moss, 2014](#); [McCarthy et al. 2018](#)). [Mummery et al. \(2017\)](#) used cosmo-OWLS (the Overwhelmingly Large Simulations; [Le Brun et al. 2014](#)) and BAHAMAS (BARYons and HALoes of MASSive Systems; [McCarthy et al. 2018](#)) to study how baryonic physics and neutrinos impact the halo mass function, mass density profiles of haloes, the halo mass-concentration relation, and the clustering properties of haloes.

The impact of baryonic physics and massive neutrinos is thought to be significant and has been considered as systematics in various works on weak lensing (WL) statistics with dark matter only simulations and observation surveys (e.g., [Yang et al. 2013](#); [Hildebrandt et al. 2017](#); [Martinet et al. 2018](#)). In this work we are motivated by the studies above that suggest the importance of physics beyond the gravity associated with cold dark matter. The

statistics of the peaks on weak gravitational lensing maps has been shown to be a powerful probe of cosmology and massive galaxy clusters (e.g., [Kruse and Schneider, 1999](#), [2000](#); [Jain and Waerbeke, 2000](#); [Dietrich and Hartlap, 2010](#); [Maturi et al., 2010](#); [Kratochvil et al., 2010](#); [Fan et al., 2010](#); [Yang et al., 2011](#); [Hamana et al., 2012](#); [Martinet et al., 2015](#); [Lin and Kilbinger, 2015](#); [Kacprzak et al., 2016](#); [Liu and Haiman, 2016](#); [Liu et al., 2016](#); [Peel et al., 2017](#), [2018](#); [Martinet et al., 2018](#); [Li et al., 2018](#); [Shan et al., 2018](#)). The weak lensing peaks arise from massive structures such as galaxy clusters but also from the large scale structure of the Universe. Thus, the peak statistics contain information about the Universe on both non-linear and linear scales.

We estimate the impact that baryons and massive neutrinos have on the counts of weak gravitational lensing peaks. The cosmological hydrodynamical simulations that we use in this work is BAHAMAS, a suite that includes the effects of massive neutrinos and for which the efficiencies of stellar and Active Galactic Nuclei (AGN) feedback have been carefully calibrated to match the observed baryon fractions of massive systems ([McCarthy et al., 2017](#)). For each run we use light-cones from BAHAMAS and generate sets of synthetic weak lensing surveys with different source redshift distributions and source number densities for galaxies from which the weak lensing signal is measured. The synthetic surveys used in this work are based on the Kilo Degree Survey (KiDS) ([Hildebrandt et al., 2017](#)), Deep Ground Based, and Deep Spaced Based survey characteristics, such as those expected for the Large Synoptic Survey Telescope (LSST, [Chang et al., 2013](#)) and Euclid (e.g., [Laureijs et al., 2011](#); [Amendola et al., 2018](#)) and for the *Hubble Space Telescope* (*HST*, e.g., the weak lensing observations in [King et al., \(2016\)](#)). We determine peaks on maps of the aperture mass statistic ([Schneider, 1996](#); [Schneider et al., 1998](#); [Maturi et al., 2010](#)). This statistic has been used on wide field surveys to identify massive objects, e.g., [Hettterscheidt et al. \(2005\)](#). Various cluster detection methods that incorporate tomographic redshift information for the source galaxies and different shapes of filter function have also been developed. For example,

[Hennawi and Spergel \(2005\)](#) considered the efficiency of cluster detection using the aperture mass statistic and also including tomographic information and optimal filtering.

Miyoung Choi led the research on comparing the dark matter only simulations with simulations including the impact of a range of different baryonic prescriptions. I also contributed to that research. For a fiducial baryonic physics model, we both explore the impact of massive neutrinos, the lower bound of the summed neutrino mass in BAHAMAS is taken from [Lesgourgues and Pastor \(2006\)](#), with additional runs increasing the summed neutrino mass by factors of 2 up to 0.48 eV. Using a fiducial baryonic prescription outlined in Section [3.2](#), I lead the examination of the correlation between high signal-to-noise (S/N) peaks and massive galaxy clusters and assessing our ability to detect clusters using aperture mass peaks.

1.4 Shapes of Galaxy Clusters

Though we assume spherical mass density models in Chapter [5](#), galaxy clusters are in general non-spherical. However, we use spherical models to represent them on average because clusters are randomly shaped and oriented on the sky. To study individual galaxy clusters it will be important to consider their departure from spherical mass densities.

High resolution simulations of galaxy cluster formation carried out since the groundbreaking work of [Navarro et al. \(1997\)](#) confirm that the shapes of cluster-scale dark matter haloes often significantly depart from spherical symmetry. Haloes are mostly (football-shaped) prolate halos, with axis ratios between the shortest and longest axis as small as 0.4 (e.g., [Jing and Suto, 2002](#); [Shaw et al., 2006](#); [Bett et al., 2007](#); [Despali et al., 2014](#)). In fact, triaxial haloes are a direct consequence of initial mass density fluctuations that are described by a Gaussian random field undergoing gravitational collapse (e.g., [Doroshkevich, 1970](#)).

The degree to which cluster shapes differ from spherical symmetry also depends on the mass and redshift (e.g., [Despali et al., 2014](#)). If dark matter is in particle form, the shape of cluster haloes also reflects the interaction cross-section for dark matter particles (e.g., [Peter](#)

et al., 2013). Galaxy clusters can also exhibit very complex structure due to merger activity (e.g., Abell 2146 King et al., 2016).

Considering the shapes of galaxy clusters is a particular interest of mine, where I will discuss them further in the Current and Future Work Chapter (Chapter 7).

1.5 Contents of this Dissertation

Chapter 2 describes the background gravitational lensing concepts needed for this dissertation. Chapter 3 describes the cosmological simulations used in this work. Chapter 4 describes how the synthetic weak lensing catalogues are created from the cosmological simulations used in this dissertation. Chapter 5 introduces stacking and goes over the results on Fong et al. (2018): “Prospects for Determining the Mass Distributions of Galaxy Clusters on Large Scales Using Weak Gravitational Lensing”. Chapter 6 introduces weak lensing peak statistics and goes over the results in a recently MNRAS submitted paper (Fong & Choi et al. 2019): “The impact of baryonic physics and massive neutrinos on weak lensing peak statistics”. Chapter 7 discusses current and future work.

Much of the text in Chapters 1, 2, 3, 4, and 5 originally appeared as part of “Prospects for Determining the Mass Distributions of Galaxy Clusters on Large Scales Using Weak Gravitational Lensing”, M. Fong, R. Bowyer, A. Whitehead, B. Lee, L. King, D. Applegate, I. McCarthy (2018), MNRAS 478-5366-5378 Fong et al. (2018). Rachel Bowyer and Alisha Whitehead were undergraduate students at Rice University and at UTD respectively, advised by Matthew Fong and Lindsay King. The Cosmo-OWLS cosmological simulations were provided by Ian McCarthy. The shear fields and moment of inertia tensors were calculated by Brandyn Lee. Rachel Bowyer created Figure 7.9. Doug Applegate provided the Weighing the Giants observational data and advice on Python algorithms. Doug Applegate and Ian McCarthy gave advice throughout the work. All the writing and other work was carried out by Matthew Fong in collaboration with Lindsay King. This article has been accepted

for publication in Monthly Notices of the Royal Astronomical Society[©]: 2018, M. Fong, Published by Oxford University Press on behalf of the Royal Astronomical Society. All rights reserved.

Much of the text in Chapters [1](#), [2](#), [3](#), [4](#), and [6](#) has been submitted to MNRAS, “The impact of baryonic physics and massive neutrinos on weak lensing peak statistics”, M.Fong, M. Choi, V. Catlett, B. Lee, A. Peel, R. Bowyer, L. King, I. McCarthy (2019), MNRAS submitted: MN-19-1088-MJ. Victoria Catlett and Rachel Bowyer are/were undergraduate students at UTD and Rice University respectively, advised by Matthew Fong and Lindsay King. The BAHAMAS cosmological simulations were provided by Ian McCarthy. The moment of inertia tensor code was provided by Brandyn Lee and adapted by Matthew Fong and Victoria Catlett. Miyoung Choi and Victoria Catlett adapted Debbie Bard’s aperture mass GPU code to run on a local machine and on a supercomputer at TACC. Austin Peel provided code to determine peaks on the aperture mass maps. Austin Peel and Ian McCarthy gave advice throughout the work. All the writing and other work was carried out by Matthew Fong (focusing on high S/N cluster mass peaks) and Miyoung Choi (focusing on lower S/N LSS peaks, most of which is not included in this dissertation) in collaboration with Lindsay King. This article has been accepted for publication in Monthly Notices of the Royal Astronomical Society Published by Oxford University Press on behalf of the Royal Astronomical Society.

Unless otherwise stated algorithms and code were developed for this dissertation. The packages from other references that we use in this dissertation are COLOSSUS, for all cosmological and DK profile calculations ([Diemer, 2017](#)), and LMFIT, for minimization and parameter estimation ([Newville et al., 2014](#)). [Bard et al. \(2012\)](#) wrote the suite of tools used in Chapter [6](#) for the calculation of the aperture mass statistic. We also use various publicly available libraries in Python, for example to calculate fourier transforms.

CHAPTER 2

WEAK GRAVITATIONAL LENSING

The material in the section has been taken from our papers listed at the end of Section 1.5: the version on record (Fong et al., 2018) and an original version (MNRAS submitted: MN-19-1088-MJ).

2.1 Brief Weak Lensing Introduction

The deflection and distortion of light as it passes a massive object can be predicted with General Relativity (GR) (Einstein, 1916). Clusters, having very large masses, are powerful gravitational lenses, or deflectors. As light bundles from a source well beyond the lens pass the lens, they are deflected and distorted in shape and size. This is due to the light passing through the gravitational potential of the lens and any other structure between the source and the observer along the line-of-sight. Because the distance that the light travels from background sources are much larger than the extent of the cluster itself, we use the thin lens approximation. For an introduction to weak gravitational lensing see for example Schneider (2005).

In Figure 2.1 we show the lens geometry of gravitational lensing assuming a point source. In the thin lens approximation we assume that the mass of the deflector is projected onto a flat plane, called the lens plane. Because light is deflected we do not observe a source at its true position β , but at the position θ , where $\hat{\alpha}$ is the angle through which a light ray is deflected at the lens plane.

With an extended source, the image can be distorted in shape and size. In the case of cluster lensing where the angular size of the source is much smaller than the angular scale on which the tidal gravitational field varies, the distortion of an image can be described by linearized lens mapping, i.e., the Jacobi matrix \mathcal{A} (Schneider, 2005). The locally linearized

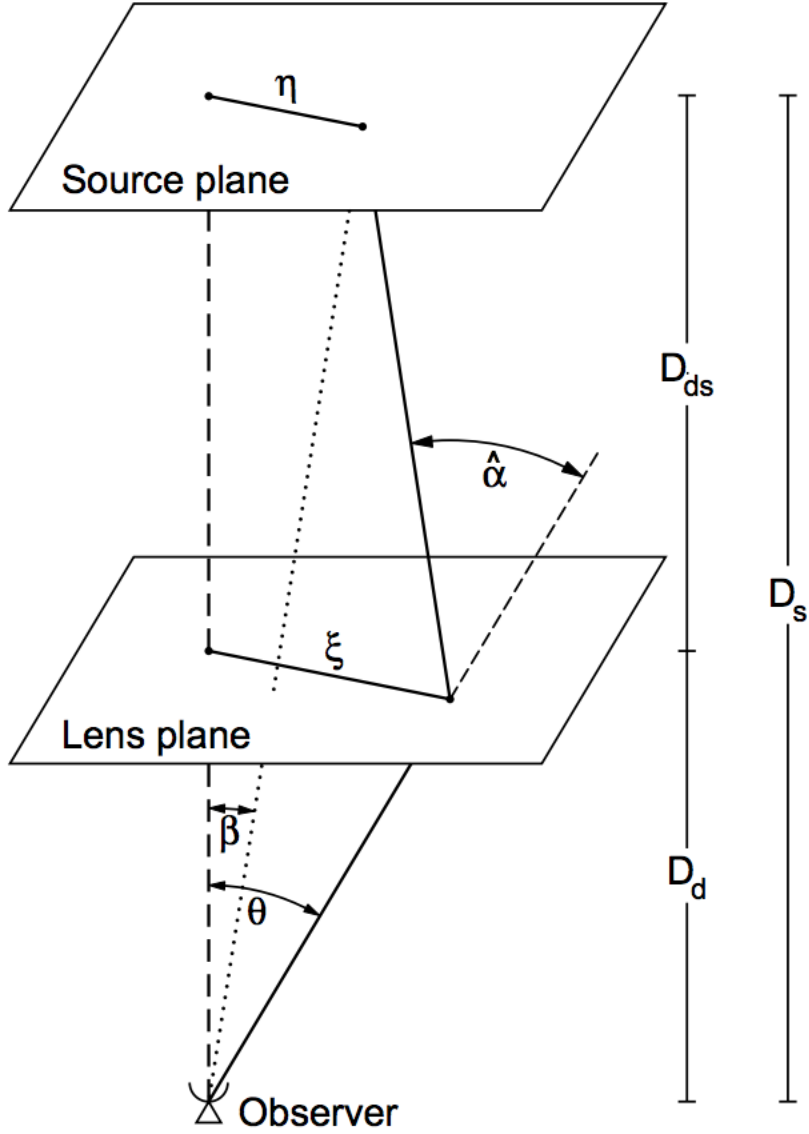


Figure 2.1: Diagram of lens geometry. β is the angular position of the source, θ is the angular position of the source image, and $\hat{\alpha}$ is the deflection angle. The distances are from the observer to the lens or deflector plane, the lens plane to the source plane, and from the observer to the source plane, D_d , D_{ds} , and D_s respectively. η and ξ are the distances from the center of the source plane to the source and from the center of the lens plane to the source image, respectively. From [Schneider et al. \(1992\)](#).

lens equation is

$$\beta - \beta_0 = \mathcal{A}(\theta_0) \cdot (\theta - \theta_0), \quad (2.1)$$

and the Jacobi Matrix is:

$$\mathcal{A}(\theta) = (1 - \kappa) \begin{pmatrix} 1 - g_1 & -g_2 \\ -g_2 & 1 + g_1 \end{pmatrix}. \quad (2.2)$$

The reduced shear,

$$g(\theta) = \frac{\gamma(\theta)}{1 - \kappa(\theta)}, \quad (2.3)$$

describes the image distortion due to the lens (assuming a circular source), which is a complex number with real and imaginary components g_1 and g_2 . The convergence, κ , is the surface mass density scaled by the critical surface mass density. The critical surface mass density is a quantity which characterizes the lens system, where any lens with $\kappa > 1$ is a sufficient but not necessary condition for multiple images. The shear is denoted by γ . In this Figure [2.2](#)

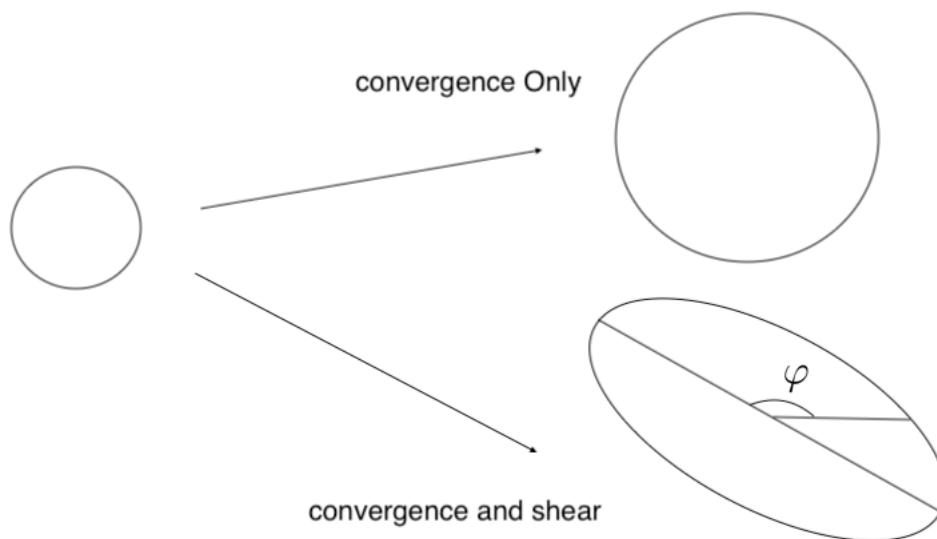


Figure 2.2: Diagram of lensing distortion for a circular source. The circular source shown on the left is distorted by a lens, which we observe on the right. In the absence of shear, the isotropically magnified image, shown on the top right, depends on the convergence. When both convergence and shear are present, the stretched image appearance, shown on the bottom right, depends on both the convergence and shear. φ is the direction of the distortion image with respect to the field-of-view.

we show a distorted image of a circular source (shown on the left). In the absence of shear,

the isotropically magnified image (shown on the top right) depends on the convergence, κ . When both convergence and shear, γ , are present, the stretched image appearance (shown on the bottom right), depends on both the convergence and shear. φ is the phase, or the orientation of the distortion image with respect to the field-of-view. The the factor 2 in the phase is the fact that an ellipse transforms into itself after a rotation by π . The compact form of the shear and reduced shear are:

$$\gamma = \gamma_1 + i\gamma_2 = |\gamma|e^{2i\varphi} \quad (2.4)$$

and

$$g = g_1 + ig_2 = |g|e^{2i\varphi}. \quad (2.5)$$

For this work we use weak gravitational lensing to study the masses and mass density profiles of clusters. In the weak lensing regime $\kappa \ll 1$ and $g \approx \gamma_+$ for spherical lenses, where $+$ denotes the tangential component. Formally the tangential shear is (following the convention in [Schneider, 2005](#)):

$$\gamma_+ = -\mathcal{R}e[\gamma e^{-2i\phi}] = -\gamma_1 \cos(2\phi) - \gamma_2 \sin(2\phi), \quad (2.6)$$

where ϕ is the position angle of the image with respect to the lens center. With spherically symmetric models, like the NFW and DK profiles, the (reduced) shear is the same as the tangential (reduced) shear.

For completion the cross component of the shear is:

$$\gamma_\times = -\mathcal{I}m[\gamma e^{-2i\phi}] = \gamma_1 \sin(2\phi) - \gamma_2 \cos(2\phi). \quad (2.7)$$

In observations we measure the ellipticities of lensed images, the ellipse axis ratio, $q = \frac{b}{a}$, and the orientation, φ . The compact form of an image ellipticity is:

$$\epsilon = \frac{1-q}{1+q}e^{2i\varphi} = \epsilon_1 + i\epsilon_2 = |\epsilon|e^{2i\varphi}. \quad (2.8)$$

The measured ellipticity is a combination of the complex intrinsic ellipticity ϵ^s of the source and the complex distortion due to the lens, g :

$$\epsilon = \frac{\epsilon^s + g}{1 + g^* \epsilon^s}, \quad (2.9)$$

where the $*$ denotes the complex conjugate. In the absence of lensing, if galaxies are randomly oriented in the Universe, taking the average ellipticities of enough unlensed galaxies on a patch of sky results in $\langle \epsilon^s \rangle \approx 0$. In the weak lensing limit, the average of a large sample of observed lensed ellipticities then yields (Schneider, 2005):

$$\langle \epsilon \rangle = g \approx \gamma. \quad (2.10)$$

Therefore in the weak lensing regime we can determine the shear of a cluster given a large enough number of lensed galaxies, providing a way to estimate the mass density profile.

The deflection and distortion of light bundles depend on the mass distribution of the lens itself and any other structure along the line-of-sight. In the thin lens approximation, the extent of the cluster is much smaller than the line-of-sight distance of the lens or the source. To calculate the shear of a spherically symmetric 3D mass density profile, we obtain the 2D surface mass density by integrating the 3D profile along the line-of-sight, dz , from $-\infty < z < \infty$ from the cluster center:

$$\Sigma(R) = 2 \int_0^\infty \rho(R, z) dz. \quad (2.11)$$

$R = D_d \sqrt{\theta_1^2 + \theta_2^2}$ is the projected radius relative to the center of the lens on the lens plane, where θ_1 and θ_2 are angular variables on the sky and D_d is the angular diameter distance to the deflector or lens plane.

The convergence is the ratio of the surface mass density to the critical surface mass density:

$$\kappa(R) = \frac{\Sigma(R)}{\Sigma_{cr}}, \quad (2.12)$$

where the critical mass density is (Subramanian and Cowling, 1986):

$$\Sigma_{\text{cr}} \equiv \frac{v_c^2}{4\pi G} \frac{D_s}{D_d D_{ds}}. \quad (2.13)$$

D_d , D_s , and D_{ds} are the angular diameter distances between the observer and the lens, the observer and the source, and the lens and the source respectively, while v_c is the speed of light, and G is the gravitational constant.

In the case of a spherically symmetric lens, the tangential shear is given by:

$$\gamma_+(x) = \frac{\bar{\Sigma}(x) - \Sigma(x)}{\Sigma_{\text{cr}}(z_d, z_s)} \equiv \frac{\Delta\Sigma(x)}{\Sigma_{\text{cr}}(z_d, z_s)}, \quad (2.14)$$

where $x = R/r_s$, with R being the projected distance on the lens plane from the halo centre and r_s is the scale radius. The mean surface mass density of the halo is given by

$$\bar{\Sigma}(x) = \frac{2}{x^2} \int_0^x x' \Sigma(x') dx'. \quad (2.15)$$

2.2 Mass Density Models

Parametric lens models are useful in that we can compare the mass density of clusters to theoretical predictions. In this work we will look at two profiles. The Navarro, Frenk, and White (NFW, Navarro et al., 1997) and the Diemer and Kravtsov (DK, Diemer and Kravtsov, 2014) models. The NFW profile is a good fit to the spherically averaged profiles of haloes formed in cold dark matter simulations out to (very roughly the virial radius) r_{200c} (Navarro et al., 1997). r_{200c} defines a sphere that encloses a mean density of $200\rho_{cr}(z)$, and the mass enclosed inside the sphere of radius r_{200c} is

$$M_{200c} \equiv M(< r_{200c}) = \frac{800\pi}{3} \rho_{cr}(z) r_{200c}^3, \quad (2.16)$$

where the critical mass density of the Universe where the halo formed is $\rho_{cr}(z) = \frac{3H^2(z)}{8\pi G}$.

The mass density profile is given by:

$$\rho_{\text{NFW}}(r) = \frac{\delta_c \rho_{cr}}{(r/r_s) (1 + r/r_s)^2}, \quad (2.17)$$

where the characteristic overdensity for the halo is:

$$\delta_c = \frac{200}{3} \frac{c^3}{\ln(1+c) - c/(1+c)}. \quad (2.18)$$

$H(z)$ is the Hubble parameter at redshift z , and G is Newton's Gravitational constant. This profile is parameterised by the scale radius, $r_s = r_{200c}/c$, and the concentration parameter, c .

DK proposes a mass density profile that describes the average mass density of clusters within and beyond the virial radius (Diemer and Kravtsov, 2014). It more accurately captures the steepening at radii $r \geq 0.5r_{200m}$ of averaged Λ CDM haloes than the NFW profile, and flattens out to the mean density of the universe, ρ_m on large scales. The subscript m denotes the mean density of the Universe as opposed to the critical density of the Universe. The DK mass density is

$$\begin{aligned} \rho_{\text{dk}}(r) &= \rho_{\text{inner}} * f_{\text{trans}} + \rho_{\text{outer}} \\ \rho_{\text{inner}} = \rho_{\text{Einasto}} &= \rho_s \exp\left(-\frac{2}{\alpha^{\text{slope}}} \left[\left(\frac{r}{r_s}\right)^{\alpha^{\text{slope}}} - 1\right]\right) \\ f_{\text{trans}} &= \left[1 + \left(\frac{r}{r_t}\right)^{\beta^{\text{slope}}}\right]^{-\frac{\gamma^{\text{steepness}}}{\beta^{\text{slope}}}} \\ \rho_{\text{outer}} &= \rho_m \left[\frac{b_e}{\frac{1}{\rho_{\text{max}}} + \left(\frac{r}{5r_{200m}}\right)^{s_e}} + 1\right]. \end{aligned} \quad (2.19)$$

The Einasto profile (Einasto, 1965) describes the inner density, the transition term f_{trans} describes the steepening of the profile around a truncation radius r_t , and the outer density is a power law that flattens out to the mean density of the Universe. The inner density is characterised by the scale density ρ_s and α^{slope} , where ρ_s is the mass density at $r = r_s$ and α^{slope} determines how quickly the slope of the inner Einasto profile steepens. The transition term parameters are $\gamma^{\text{steepness}}$ and β^{slope} , where $\gamma^{\text{steepness}}$ defines the steepness of the density around $r \approx r_{200m}$ and β^{slope} tells how quickly the slope changes. The outer density profile

parameters are ρ_m , the radius r_{200m} that encloses an average overdensity of $200\rho_m$, and parameters that describe the normalization and slope of the power law of the outer profile, b_e and s_e respectively. The outer density profile is a modification of [Diemer and Kravtsov \(2014\)](#), where the term $\frac{1}{\rho_{\max}}$ is introduced to avoid a spike toward the center of the cluster. This term determines the maximum overdensity that can be contributed from the outer profile. We use the COLOSSUS ([Diemer, 2017](#)) package for all DK profile calculations, where $\frac{1}{\rho_{\max}} = 0.001$. Note that the mean cosmic density acts like a constant density sheet of mass and hence does not impact on the shapes of distant galaxies.

[Diemer and Kravtsov \(2014\)](#) show that some of the parameters are correlated, reducing the number of free parameters from eight to four:

$$\begin{aligned}\alpha^{\text{slope}}(\nu) &= 0.155 + 0.0095\nu^2, \\ r_t &= (1.9 - 0.18\nu)r_{200m},\end{aligned}\tag{2.20}$$

where ν is the peak height. In this work, we fix $\beta^{\text{slope}} = 4$ and $\gamma^{\text{steepness}} = 8$, which is an accurate fit to the mass density profiles if the truncation radius is related to ν and r_{200m} ([Diemer and Kravtsov, 2014](#)). The remaining four parameters are the Einasto parameters ρ_s and r_s , and the two outer profile parameters b_e and s_e . In [Diemer and Kravtsov \(2014\)](#), the best-fit for the outer parameters are $b_e \approx 1.0$ and $s_e \approx 1.5$. For the majority of this work we will fix $b_e = 1.0$ and $s_e = 1.5$ for the DK model and use the mass and concentration parameters, M_{200c} and c , to describe the NFW and DK models.

2.3 Gravitational Shear for the NFW and DK Models

The NFW tangential shear can be obtained analytically:

$$\gamma_+^{\text{NFW}}(x) \equiv \frac{\Delta\Sigma^{\text{NFW}}(x)}{\Sigma_{\text{cr}}(z_d, z_s)} = \frac{2\rho_c r_s}{\Sigma_{\text{cr}}(z_d, z_s)} f^{\text{NFW}}(x),\tag{2.21}$$

with the form of the shear (Niikura et al., 2015; Bartelmann, 1996):

$$f^{\text{NFW}}(x) = \begin{cases} \frac{2}{x^2} \ln \frac{x}{2} + \frac{1}{1-x^2} \left(1 + \frac{2-3x^2}{x^2 \sqrt{1-x^2}} \cosh^{-1} \frac{1}{x} \right), & (x < 1) \\ \frac{5}{3} - 2 \ln 2, & (x = 1) \\ \frac{2}{x^2} \ln \frac{x}{2} - \frac{1}{x^2-1} \left(1 + \frac{2-3x^2}{x^2 \sqrt{x^2-1}} \cos^{-1} \frac{1}{x} \right), & (x > 1) \end{cases}$$

and the central density parameter (following notation in Niikura et al., 2015):

$$\rho_c = \delta_c \rho_{cr} = \frac{M_{200c}}{4\pi r_s^3 m(c)}, \quad (2.22)$$

where $m(c) = \log(1+c) - \frac{c}{1+c}$. The NFW tangential shear form $f^{\text{NFW}}(x)$ is self-similar, meaning $\gamma_+^{\text{NFW}}(x)$ has the same shape for any combinations of M_{200c} and c .

The DK shear cannot be obtained analytically, so it must be calculated numerically. Figure 2.3 shows that the DK and NFW 3D density, 2D convergence, and shear are very similar within r_{200c} for typical parameters that are relevant to this chapter ($M_{200c} = 5 \times 10^{14} M_\odot$ and $c = 4$; $r_{200c} = 1.41$ Mpc). The profiles remain in agreement for a wide range of mass and concentration combinations within r_{200c} , encompassing the average parameters for the sample of 50 massive simulated clusters that are used in this chapter. We first of all hypothesize that the DK shear can be approximated similarly to the NFW profile, where the DK shear form is self-similar:

$$\gamma_+^{\text{DK}}(x) \equiv \frac{\Delta \Sigma^{\text{DK}}(x)}{\Sigma_{\text{cr}}(z_d, z_s)} = \frac{2\rho_c r_s}{\Sigma_{\text{cr}}(z_d, z_s)} f^{\text{DK}}(x, \vec{\pi}), \quad (2.23)$$

where $\vec{\pi}$ are the mass and concentration parameters. Since the DK profile, $f^{\text{DK}}(x, \vec{\pi})$ has to be calculated numerically.

In Figure 2.4 we vary the parameters for the NFW and DK shear forms. For cosmo-OWLS (Section 3.1) the mean mass of the 50 most massive clusters is $\langle M^{3D} \rangle = 6.64 \times 10^{14} M_\odot$ with a range $4.04 < M^{3D} [10^{14} M_\odot] < 17.40$ ¹. The range of parameters plotted are $2.0 <$

¹The simulation masses (M^{3D}) are calculated by identifying the particle deepest in the potential well of a cluster and calculating the mass density within spheres around that particle. When a mean enclosed density of $200\rho_c$ is reached, the mass enclosed in r^{3D} is M^{3D} .

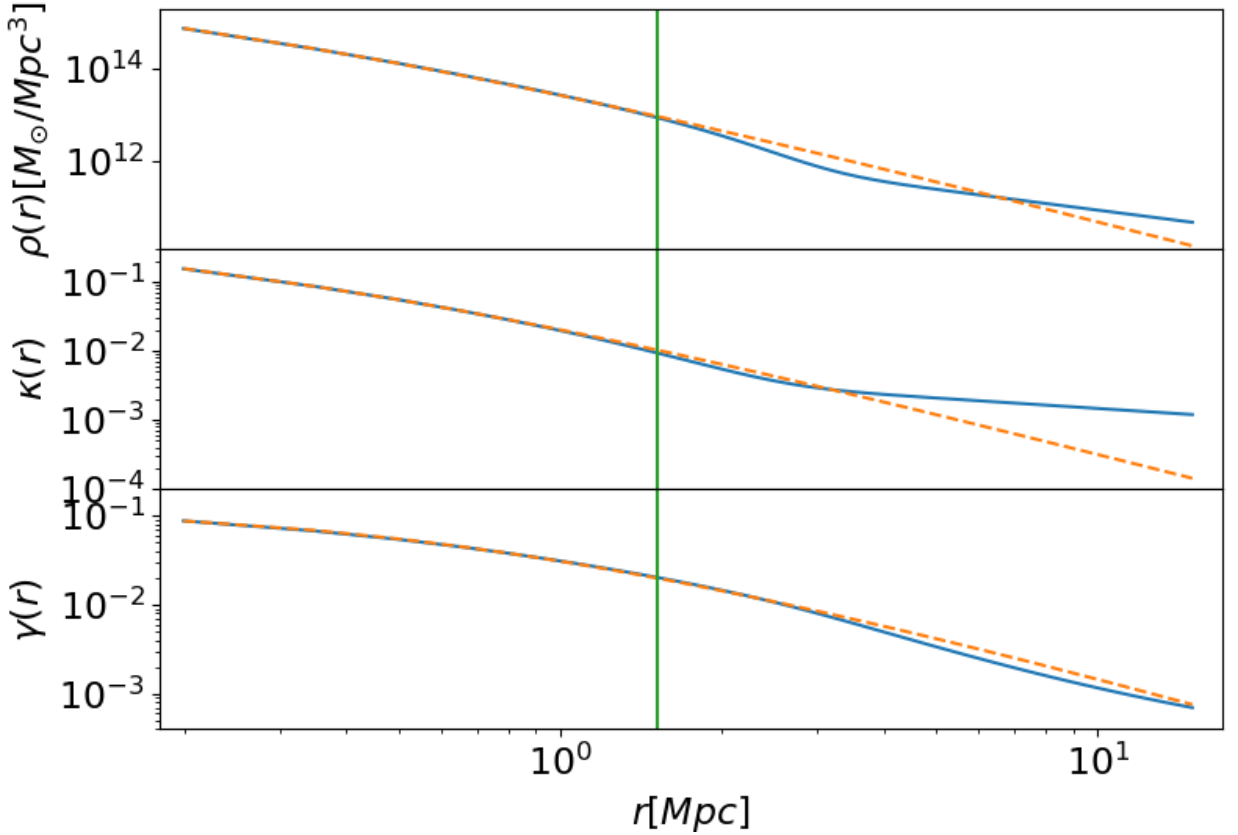


Figure 2.3: For NFW and DK, the upper, middle, and lower panels compare the 3D mass density, convergence, and shear profiles respectively. The DK profile is the solid blue curve, the NFW is the dashed orange curve, and $r_{200c} = 1.41 Mpc$ is the solid green vertical line. In this example we use typical values of $M_{200c} = 5 \times 10^{14} M_{\odot}$ and $c = 4$ to illustrate that the DK and NFW profiles are a good match out to the virial radius.

$M_{200c}[10^{14} M_{\odot}] < 17.4$ and $2.5 < c < 5.5$, encompassing the masses of clusters used in the simulations, and the concentration range encompasses the minimum and maximum concentrations using the c - M relation of various models.² In the top panel we show the NFW and DK shear forms, dashed curve and solid curves respectively, and a weak lensing outer fit radius of 2.3 Mpc ($r_s \approx 0.38$ Mpc), dashed vertical line. Because the NFW shear can be written exactly as in Equation 2.21, the NFW forms are in exact agreement, and is repre-

²COLOSSUS was used to calculate concentrations. The models are Bullock et al. (2001); Duffy et al. (2008); Klypin et al. (2011); Prada et al. (2012); Bhattacharya et al. (2013); Dutton and Macciò (2014); Diemer and Kravtsov (2015); Klypin et al. (2016). Please see Diemer (2017) for details.

sented by the dashed red curve $f^{NFW}(x)$. However since Equation 2.23 is an approximation, the $f^{DK}(x, \vec{\pi})$ forms do not lie on top of each other for the wide range of parameters listed above. This means that $f^{DK}(x, \vec{\pi})$ in Equation 2.23 depends on mass and concentration. A more typical mass and concentration in the simulation ($M_{200c}[10^{14}M_{\odot}] = 5.0$, $c = 4.0$) is represented by a thick dashed curve. The DK forms, for masses and concentrations we use in this work, have roughly the same small difference from the thick dashed black curve within the weak lensing fit range. Therefore the plot shows that the DK and NFW forms are both nearly self-similar over fit ranges typically probed by weak lensing observations, for clusters relevant to this work. Furthermore, Niikura et al. (2015) shows that the NFW shear does a good job at representing the stacked shear of the 50 massive clusters in their simulations and in observations, out to about 2.3 Mpc. With the NFW and DK shear forms in agreement within roughly r_{200c} , we can determine the mass and concentration from the stacked shear by fitting over the weak lensing range (where both the DK and NFW shear profiles are similar) using the NFW profile. We then use these parameters ($\vec{\pi}$) to determine the DK form ($f^{DK}(x, \vec{\pi})$) out to larger radii and compare the form to stacked shear data, within and beyond r_{200c} .

For spherical profiles the reduced shear, g , is given by

$$g(x) = \frac{2\rho_c r_s}{\Sigma_{\text{cr}}(z_d, z_s)} \frac{f(x)}{1 - \kappa(x)} = \frac{2\rho_c r_s}{\Sigma_{\text{cr}}(z_d, z_s)} F(x). \quad (2.24)$$

Here $f(x)$ can be the form of the NFW or DK shear profiles, $f^{NFW}(x)$ and $f^{DK}(x, \vec{\pi})$ respectively, while $F(x)$ is the form of the NFW or DK reduced shear profiles, $F^{NFW}(x)$ and $F^{DK}(x, \vec{\pi})$ respectively. In the weak lensing regime $\kappa(x) \ll 1$ and $F(x) \approx f(x)$.

Figure 2.5 shows the ideal reduced shear profiles of the DK and NFW profiles with the same parameters. The solid lines are DK and the dashed are the NFW. The mass of these clusters is $M_{200c} = 10^{15}M_{\odot}$ with concentrations 3, 4, and 5, from bottom to top. This shows that the DK ideal reduced shear profiles do in fact differ from the NFW for high masses,

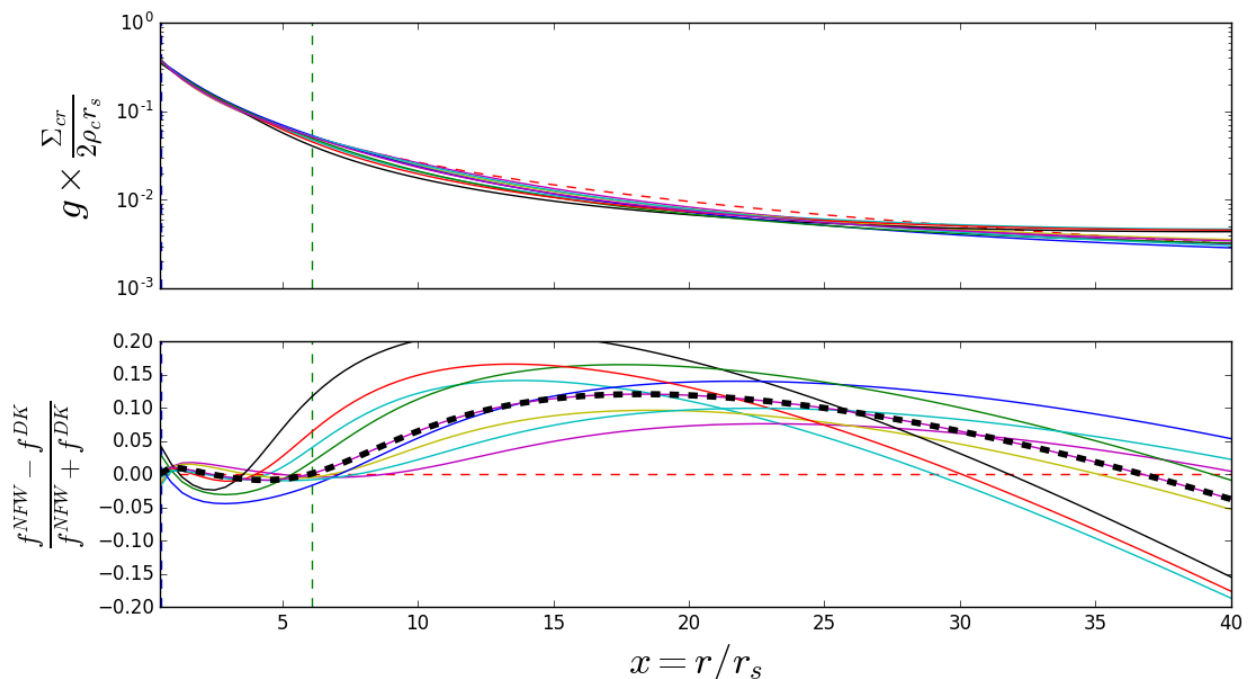


Figure 2.4: The top panel here shows the shear forms (scaled shear) for the NFW and DK profiles for a wide range of parameters. The dashed red curve is the NFW form, $f^{NFW}(x)$, the solid curves are the DK forms, f^{DK} , and the dashed vertical line a outer fit radius of 2.3 Mpc ($r_s \approx 0.38$ Mpc). The range of parameters plotted are $2.0 < M_{200c}[10^{14}M_{\odot}] < 17.4$ and $2.5 < c < 5.5$. The NFW form is self-similar so for any parameters the form will lie on the dashed curve, however the DK form varies with mass and concentration. The bottom panel measures the difference between the NFW and DK forms. The dashed horizontal line represents the difference between the NFW form to itself ($y = 0$), and the other lines are the difference between the DK forms and NFW form. Most of parameters used in these panels are quite extreme, where a more typical mass and concentration ($M_{200c}[10^{14}M_{\odot}] = 5.0$, $c = 4.0$) is highlighted by a thick black dashed curve. To the left of the dashed vertical line, the DK forms are nearly self-similar for more typical mass ranges used in this chapter. This shows that, though the DK and NFW forms differ quite significantly for large radii, for typical present day weak lensing fit ranges the DK and NFW forms nearly agree with one another for more typical masses and concentrations we use in this work.

well outside of the mean of the cluster masses in this dissertation. However, for more typical masses and concentrations, $M_{200c} \approx 5 - 7 \times 10^{14}M_{\odot}$ and $c = 2 - 7$, the profiles within r_{200c} agree with one another.

In this chapter we want to see if the numerical DK form $F^{DK}(x, \vec{\pi})$ is supported by surveys on large scales, keeping in mind the concentration dependency outside of r_{200c} . In

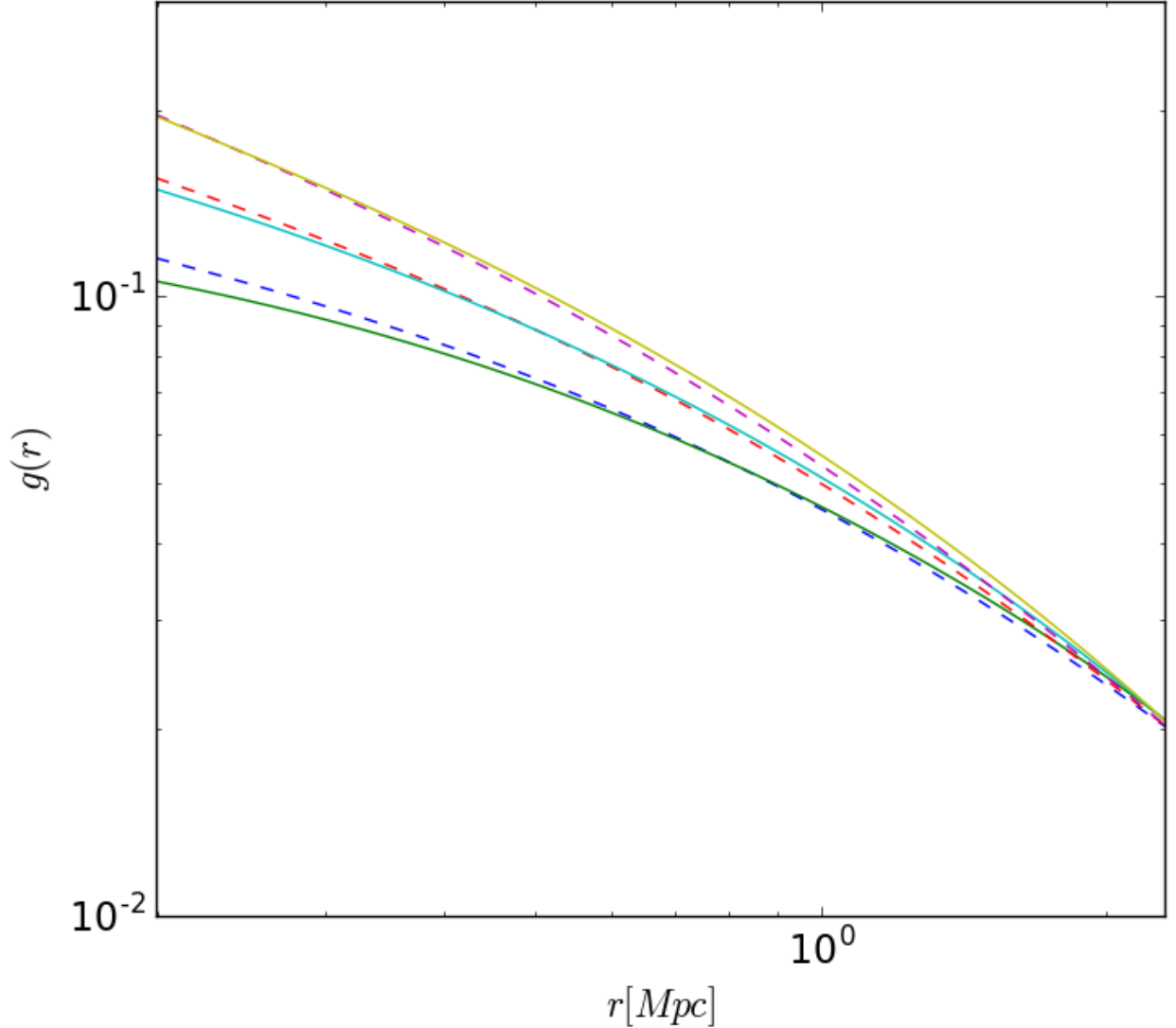


Figure 2.5: The solid and the dashed lines are the DK and NFW ideal reduced shear profiles respectively. Though the profiles are similar for the typical average parameters used in this dissertation, we show that for higher mass bins there are deviations when varying concentration. The mass of these clusters is $M_{200c} = 1 \times 10^{15} M_{\odot}$ with concentrations 3, 4, and 5, from bottom to top. Six of the 50 clusters used in this dissertation are more massive than this example.

that section we showed that, within the weak lensing regime and r_{200c} , the NFW and DK profiles behave similarly. So if the concentration can be determined by using the NFW profile, then that concentration can be used in the DK form. As a reference we will compare

this to the NFW form $F^{\text{NFW}}(x)$. For the NFW, the reduced shear $g^{\text{NFW}}(x) = \frac{\gamma^{\text{NFW}}(x)}{1-\kappa^{\text{NFW}}(x)}$ is, though complicated, an analytic function of x . Note that $g(x)$ and x are dimensionless.

From Equation [2.24](#), with an ideal spherical halo we can get the "form" of the reduced shear for an individual halo with

$$F(x) = \frac{\Sigma_{\text{cr}}}{2\rho_c r_s} g(x). \quad (2.25)$$

The scaling factor $\frac{\Sigma_{\text{cr}}}{2\rho_c r_s}$ scales the signal according to cluster mass. So in the ideal case, the form of the reduced shear, $F(x)$, will be the same for all clusters in the weak lensing regime and r_{200c} and within the parameter space of this chapter. The form, $F(x) = \frac{f(x)}{1-\kappa(x)}$, can vary due to the parameter dependency in $\kappa(x)$. However, our focus is in the weak lensing regime where $\kappa(x) \ll 1$ and therefore $F(x) \approx f(x)$ ³. For the rest of this chapter we will simply just refer to $F(x)$ since $F^{\text{DK}}(x, \boldsymbol{\pi})$ and $F^{\text{NFW}}(x)$ are very similar in the weak lensing regime out to the virial radius. We want to test if the DK profile can describe stacked clusters beyond the virial radius. As the scaling factor shifts a reduced shear signal vertically to obtain $F(x)$, the choice in scaling the radial bins can shift the curve either left or right. It is important to note that neither changes the shape of the signal. Through this chapter we scale the radial bins by r_s .

³It can be shown that scaling γ^{NFW} for various ideal haloes will all conform to the curve $f^{\text{NFW}}(x)$ for all of x

CHAPTER 3

SIMULATIONS

The material in the section has been taken from our papers listed at the end of Section 1.5: the version on record (Fong et al., 2018) and an original version (MNRAS submitted: MN-19-1088-MJ).

3.1 Cosmo-OWLS

The simulations used in the first project, on stacking weak lensing signals from galaxy clusters, are from Cosmo-OWLS (Le Brun et al., 2014), a suite of cosmological hydrodynamic simulations using a version of the GADGET3 code (last described in Springel, 2005). The runs explore structure formation in cosmologies with dark matter only, and with dark matter and various prescriptions for baryonic physics. A particularly important effect is due to AGN (Active Galactic Nucleus) feedback, the feedback radiation due to accretion of matter onto super massive black holes at the center of galaxies. Without this feedback, simulations produce an excess of massive galaxies, called the overcooling problem. The strength of AGN feedback in Cosmo-OWLS was tuned to reproduce a wide range of observations. The simulation runs were carried out in periodic boxes of $400 h^{-1}$ Mpc on a side (comoving), using the same initial conditions and cosmological parameters from *WMAP7* (Komatsu et al., 2011): $\{\Omega_m, \Omega_b, \Omega_\Lambda, \sigma_8, n_s, h\} = \{0.272, 0.0455, 0.728, 0.81, 0.967, 0.704\}$. Each run uses 2×1024^3 particles with masses $\approx 3.75 \times 10^9 h^{-1} M_\odot$ and $\approx 7.54 \times 10^8 h^{-1} M_\odot$ for dark matter particles and for baryonic particles respectively.

We specifically use two of the six simulation runs from Le Brun et al. (2014):

- DMO: a Dark Matter Only run that accounts for only gravitational interaction between particles.

- AGN Feedback 8.0, the feedback due to accretion of matter on to supermassive black holes at the center of galaxies: in addition to gravity this run implements star formation (Schaye and Dalla Vecchia, 2008), with radiative cooling, stellar evolution and chemical enrichment (Wiersma et al. 2009a and Wiersma et al. 2009b), supernova feedback (Dalla Vecchia and Schaye, 2008) and a UV/X-Ray photoionizing background (Haardt and Madau, 2001). The growth of supermassive black holes and AGN feedback are described by prescriptions from Booth and Schaye (2009). AGN 8.0 yields clusters that are closest to observed clusters out of the various Cosmo-OWLS runs.

The 50 most massive clusters at $z = 0.25$, having M_{200c} in excess of $4.04 \times 10^{14} M_{\odot}$ in the DMO run, were extracted in boxes of 30 Mpc on a side. These clusters were matched to their counterpart clusters in the AGN 8.0 run, then each of the clusters was projected along the z -axis in order to obtain maps of the projected mass density, a scaled version of the lensing convergence. The maps of lensing shear and reduced shear were obtained using the relationship between lensing convergence and shear in Fourier space (see e.g., Schneider, 2005).

3.2 BAHAMAS

In the second project, studying the impact of summed neutrino mass on weak lensing peaks and clusters, we use data extracted from BAHAMAS (McCarthy et al., 2017). Motivated by the fact that neutrinos are massive and by the tension between cosmological parameter estimates from the LSS and the primary CMB, BAHAMAS allows for a range of non-zero neutrino masses (McCarthy et al., 2018). BAHAMAS is the only suite of cosmological hydrodynamical simulations that have been explicitly calibrated on the baryon fractions of collapsed systems. This guarantees that the response of the redistribution of total matter due to baryonic physics is broadly correct (see Table 1 of McCarthy et al., 2017). In this

section we will discuss the different runs with varying cosmologies and neutrino mass that we use from the BAHAMAS simulations. We also discuss the creation of synthetic light-cones and weak lensing galaxy catalogues used in our study.

The initial conditions for BAHAMAS are based on the cosmological parameters derived from the cosmic microwave background WMAP 9-yr mission (WMAP9, [Hinshaw et al., 2013](#)) and the Planck 2015 mission (Planck2015, [Planck Collaboration et al., 2016](#)), using the six-parameter standard Λ CDM model.

[McCarthy et al. \(2018\)](#) generated suites of WMAP9 simulations for the collisionless dynamics (DMONLY), for varying AGN feedback temperatures with massless neutrinos, and also for different summed neutrino mass with fiducial AGN feedback (see Table [3.1](#)). For example, the BAHAMAS fiducial AGN feedback value 7.8 has AGN feedback temperature $\Delta T_{\text{heat}} = 10^{7.8} K$. This feedback radiation comes from the active galactic nuclei at the center of galaxies. The summed neutrino masses are set to M_ν [eV] = 0.06, 0.12, 0.24, and 0.48. See [McCarthy et al. \(2018\)](#) for details of the baryonic physics implemented in the simulations.

The suites for the *Planck* 2015 cosmology were also generated by [McCarthy et al. \(2018\)](#) for varying neutrino mass to explore the $\sigma_8 - \Omega_m$ parameter space, and to attempt to resolve the well known tension at $2\text{-}\sigma$ between the missions. For the “*Planck* 2015/ A_{Lens} - based” simulations used in this dissertation, the Markov Chains of [Planck Collaboration et al. \(2016b\)](#) corresponding to the “CMB+BAO+CMB lensing” with marginalization over A_{Lens} (the amplitude of the CMB lensing power spectrum) was used (See Figure 2 of [McCarthy et al. \(2018\)](#)). Cosmological parameter sets were selected that have summed neutrino mass within $\Delta M_\nu = 0.02$ eV of the target value, and the weighted mean of the other important cosmological parameters is taken from the Markov Chains. By selecting parameter values in this way, it ensures that the selected cosmologies are consistent with the CMB+BAO constraints.

Table 3.1: Cosmological parameter values for 12 suites of the BAHAMAS simulations (McCarthy et al., 2017, 2018). Adjustments on the summed neutrino mass, baryonic matter fractions, AGN feedback temperatures, σ_8 values, and changes in S_8 are given in this table. The columns are: (1) The summed mass of the 3 active neutrino species (we adopt a normal hierarchy for the individual masses); (2) the logarithm to base 10 of the AGN feedback temperature defined by McCarthy et al.; (3) the total matter density; (4) present-day baryon density; (5) present-day dark matter density; (6) present-day neutrino density, computed as $\Omega_\nu = M_\nu/(93.14 \text{ eV } h^2)$; (7) present-day (linearly-evolved) amplitude of the matter power spectrum on a scale of $8 \text{ Mpc } h^{-1}$ (note that we use A_s rather than σ_8 to compute the power spectrum used for the initial conditions, thus the initial conditions are CMB normalised); (8) $S_8 = \sigma_8 \sqrt{\Omega_m}/0.3$.

(1)	(2)	(3)	(4)	(5)	(6)	(7)	(8)
$M_\nu(\text{eV})$	$\log(\Delta T_{\text{heat}}[\text{K}])$	Ω_m	Ω_b	Ω_{cdm}	Ω_ν	σ_8	S_8
WMAP9-based							
0 (DMONLY)	-	0.2793	0.0463	0.2330	0.0	0.8211	0.7923
0 (Low AGN)	7.6	0.2793	0.0463	0.2330	0.0	0.8211	0.7923
0 (Fiducial AGN)	7.8	0.2793	0.0463	0.2330	0.0	0.8211	0.7923
0 (High AGN)	8.0	0.2793	0.0463	0.2330	0.0	0.8211	0.7923
0.06	7.8	0.2793	0.0463	0.2317	0.0013	0.8069	0.7786
0.12	7.8	0.2793	0.0463	0.2304	0.0026	0.7924	0.7646
0.24	7.8	0.2793	0.0463	0.2277	0.0053	0.7600	0.7333
0.48	7.8	0.2793	0.0463	0.2225	0.0105	0.7001	0.6755
Planck 2015/A_{Lens}-based							
0.06	7.8	0.3067	0.0482	0.2571	0.0014	0.8085	0.8175
0.12	7.8	0.3091	0.0488	0.2574	0.0029	0.7943	0.8063
0.24	7.8	0.3129	0.0496	0.2576	0.0057	0.7664	0.7827
0.48	7.8	0.3197	0.0513	0.2567	0.0117	0.7030	0.7257

CHAPTER 4

GENERATION OF SYNTHETIC GRAVITATIONAL LENSING GALAXY CATALOGUES

The material in the section has been taken from our papers listed at the end of Section 1.5: the version on record (Fong et al., 2018) and an original version (MNRAS submitted: MN-19-1088-MJ).

In this chapter we describe how we generate synthetic catalogues of galaxies lensed by foreground galaxy clusters or galaxy clusters embedded in the LSS of the Universe, in Sections 4.1 and 4.2 respectively.

4.1 Mock Catalogues from Cosmo-OWLS

In Chapter 5 we use mock catalogues from Cosmo-OWLS to investigate the DK profile described in Section 2.2 earlier in this dissertation. From Cosmo-OWLS we obtain κ and γ (real and complex components γ_1, γ_2) on a 2D projected lens plane with 30 Mpc per side and 2,000 regularly spaced pixel bins spanning each side. We describe how γ is obtained from κ in the next section on mock catalogues from BAHAMAS. From there we generate sets of background source galaxies with random locations, with $z_s = 1$. Different number densities of galaxies were explored, $n_0 = 10$ or 30 gal/arcmin² and the total number of galaxies adjusted using Poisson statistics to allow for shot noise in their number. For upcoming surveys like LSST, we use $n_0 = 30$ gal/arcmin², while for past surveys like Weighing the Giants (WtG, Applegate et al., 2014), $n_0 = 10$ gal/arcmin² in keeping with the observations. The (complex) intrinsic ellipticity of each source galaxy, describing its shape and orientation of the non-lensed source, ϵ^s , was drawn from a Gaussian distribution with $\sigma_{\epsilon^s} = 0.25$. Following Schneider et al. (2000), the number density of galaxies on each small patch of sky

was modified to account for lensing magnification¹, $n = n_0 \mu^{\beta_{\text{slope}} - 1}$, where $\mu = \frac{1}{(1-\kappa)^2 - \gamma^2}$ is the magnification on the small patch, and β_{slope} is the slope of the unlensed source counts taken to be $\beta_{\text{slope}} = 0.5$. The magnification of each galaxy due to the foreground cluster was calculated at each location, and after drawing a random uniform variate $\eta_{\text{random}} \in [0, 1]$, the galaxy was only included in the lensed galaxy catalogue if $[\mu]^{\beta_{\text{slope}} - 1} \geq \eta_{\text{random}}$, otherwise discarded. This accounts for the change in brightness of lensed galaxies as well as the stretching of space around them, having more magnified galaxies more likely to be excluded. Since we are in the weak lensing regime we assume that the galaxy image positions are not offset from the source positions.

After taking into account survey characteristics, and intrinsic shape noise, we calculate (complex) ϵ (Equation 2.9) at galaxy positions on the lens plane. The ellipticity amplitude and tangential component, $\epsilon_{(s_a)}$ and $\epsilon_{(s_a)+}$ respectively, are given by (Schneider et al., 2000)

$$\epsilon_{(s_a)} = \sqrt{\epsilon_{1(s_a)}^2 + \epsilon_{2(s_a)}^2} \quad (4.1)$$

and

$$\epsilon_{(s_a)+} = -\epsilon_{1(s_a)} \cos(2\phi) - \epsilon_{2(s_a)} \sin(2\phi), \quad (4.2)$$

where $\epsilon_{1(s_a)}$ and $\epsilon_{2(s_a)}$ are the real and complex components of the lensed galaxy s_a respectively.

For the AGN 8.0 and DMO simulations multiple WtG and LSST-like Monte Carlo runs were carried out to obtain synthetic weak lensing catalogues, taken from boxes centered on galaxy clusters with 30 Mpc per side, where the differences between similar survey-like Monte Carlo runs are the random background source galaxy locations (still with $z_s = 1$) and shape noise realizations. This was done to see if different realizations would give significantly different results when the synthetic catalogues were analysed, comparing the

¹Although this effect is small, we include it for completeness.

average (stacked) cluster signals on large scales with the DK reduced shear. Though all the LSST-like runs for 50 clusters had some large differences in mass estimations for individual clusters, there were no significant differences in the final average results. The same can be said about the WtG-like runs, but these results have larger error bars because of the lower number density of background galaxies from which the shear is measured (see Section 5.7). We also explore using exclusively ideal DK or NFW haloes (as opposed to clusters from simulations) for each set of survey-like characteristics to compare our simulation runs with ideal runs (see Section 5.4).

4.2 Synthetic Weak Lensing Catalogues from BAHAMAS light-cones

For the BAHAMAS simulations that we use to explore the impact of massive neutrinos and baryonic physics on gravitational lensing signatures, we employ light-cones for the simulations instead of extracting clusters in boxes. Light-cones can be thought of as capturing the dark and luminous structure that is distributed in redshift, that light-bundles would pass by on their journey through the Universe. This gives us access to galaxy clusters as well as to the uncorrelated LSS along the line-of-sight to the distant galaxies from which we measure the weak lensing signal. The convergence and shear for the light-cones are determined for distant galaxies which have a distribution in redshift, reflecting different types of surveys, discussed later in this section.

The simulation boxes of BAHAMAS from which the light-cones are constructed are $400\text{Mpc } h^{-1}$ per comoving side. In order to construct BAHAMAS light-cones, McCarthy et al. (2018) saved particle data at snapshots from $z = 3$ to today. There are 15 snapshots at $z = 0.0, 0.125, 0.25, 0.375, 0.5, 0.75, 1.0, 1.25, 1.5, 1.75, 2.0, 2.25, 2.5, 2.75,$ and 3.0 . The snapshots were then randomly oriented and translated, and slices of $5 \times 5 \text{ deg}^2$ (at pixel resolution of 10 arcseconds) were taken from the snapshots. A total of 25 randomisations of rotations and translations of the 15 snapshots were performed, the same for each cosmology

and prescription for baryonic physics and neutrino mass, so that cosmic variance does not play a role when comparing light-cones across different runs. Here we consider 25 light-cones with a total area 625 deg².

The distorted appearance of the weakly lensed images of distant sources can be described by lensing convergence and shear. The weak lensing calculations here assume the so-called "Born approximation", where the paths of light rays are approximated as straight lines in comoving coordinates. This has been shown to be accurate for weak lensing (Schneider et al., 1998; White and Vale, 2004). In a given cosmological model, the weak lensing convergence at a particular angular position, $\kappa(\theta)$, depends on the spatial distribution of mass density fluctuations, δ , in the Universe, and the redshift distribution of sources that are being lensed by the fluctuations, $p_s(z)$:

$$\kappa(\theta) = \frac{3\Omega_m H_0^2}{2v_c^2} \int_0^{\chi(z_{\max})} (1+z)s(\chi)\delta(\chi, \theta)d\chi, \quad (4.3)$$

where v_c is the speed of light, χ is the cosmological comoving distance, and $s(\chi)$ is a lensing kernel defined as:

$$s(\chi) = \chi(z) \int_z^{z_{\max}} p_s(z') \left(\frac{\chi(z') - \chi(z)}{\chi(z')} \right) dz'. \quad (4.4)$$

The lensing kernel depends on the source redshift probability distribution, $p_s(z)$, where the maximum source redshift is z_{\max} and the distribution is normalised to 1. The light-cones we use from BAHAMAS extend out to $z_{\max} = 3$. The lensing convergence results in an isotropic magnification of a lensed source.

Given a map of the weak lensing convergence, the complex shear, $\gamma = \gamma_1 + i\gamma_2$, can be obtained using Fourier transform techniques since both γ and κ can be written as linear combinations of second derivatives of the lensing potential. Following e.g., Clowe et al. (2004):

$$\tilde{\gamma} = \left(\frac{\hat{k}_1^2 - \hat{k}_2^2}{\hat{k}_1^2 + \hat{k}_2^2} \tilde{\kappa}, \frac{2\hat{k}_1\hat{k}_2}{\hat{k}_1^2 + \hat{k}_2^2} \tilde{\kappa} \right) \quad (4.5)$$

where $\tilde{\gamma}$ and $\tilde{\kappa}$ are the Fourier transforms of the complex γ and scalar κ maps, and \hat{k} are wave vectors in Fourier space. The inverse Fourier transform of $\tilde{\gamma}$ yields γ .

The light-cones extracted from the simulations then give us ideal convergence maps, integrating the spatial matter overdensities $\delta(\chi, \theta)$ through the discrete slices along the line of sight with the kernel containing the source redshift distribution $n_s(z)$, as in Equation 4.3 and 4.4. We adopt two different redshift distributions, one for the 450 deg² Kilo Degree Survey (KiDS-450, Hildebrandt et al., 2017) and one predicted for the LSST survey (Chang et al., 2013). The convergence maps for the former were created by McCarthy et al. (2018) and the convergence maps for the latter were constructed for this work. Shear maps, and reduced shear maps, are constructed from convergence maps using Equation 4.5 and 2.24. Using the reduced shear maps from the simulations, synthetic catalogues of weakly lensed galaxies are produced.

As for the Cosmo-OWLS catalogues, we populate the maps with unlensed galaxies that are randomly placed on the sky, with number density appropriate for observations with a particular survey. In this case, however, the sources are distributed in redshift. The moduli of the complex ellipticities (related to the axis ratios) are drawn from a Gaussian distribution with $\sigma_{e^s} = 0.25$ and zero mean. The position angles, φ^s , are randomly assigned between 0 and π . At the position of a source galaxy, the reduced shear is extracted at the nearest pixel of the BAHAMAS maps. The observed ellipticity is determined using Equation 2.9 (e.g., Bartelmann, 1996; Schneider et al., 1998).

In this work we roughly base one of the 625 deg² synthetic surveys on Hildebrandt et al. (2017), where they analyse ~ 450 deg² of imaging data from the Kilo Degree Survey, or KiDS. In KiDS the effective number density of galaxies is 8.53 gal/arcmin² (the number density of galaxies was determined in Hildebrandt et al. (2017) by using the method proposed by Heymans et al. (2012)), but for our synthetic survey we use a source number density of 9 gal/arcmin². The observed ellipticity dispersion in Hildebrandt et al. (2017) is $\sigma_{e^s} \approx 0.33$.

We also consider synthetic surveys of the same 625 deg^2 area, but with convergence (shear and reduced shear) maps constructed using the source redshift distribution from [Chang et al. \(2013\)](#), estimated for the deeper upcoming Large Synoptic Survey Telescope (LSST, [Chang et al., 2013](#)). Both LSST and *Euclid* ([Amendola et al., 2018](#); [Laureijs et al., 2011](#)) surveys have an expected effective galaxy source number density $n_{\text{eff}} = 30 \text{ gal/arcmin}^2$. We also consider $n_{\text{eff}} = 60 \text{ gal/arcmin}^2$ when we create our synthetic lensing catalogues, to reflect deeper space based characteristics, such as the *HST* (see for example the source number density in [King et al. \(2016\)](#)). Note that we use the same redshift distribution for this even deeper survey, but increase the effective number density of sources from which the shear can be measured. The different surveys with the effective number density of 9, 30, and 60 gal/arcmin^2 will be referred to as KiDS, Deep Ground Based (DGB), and Deep Space Based (DSB) respectively.

Similar to [Martinet et al. \(2018\)](#), we generate 5 synthetic catalogues of observed ellipticities with different shape realisations per suite (as in Table [3.1](#)) to make sure that the simulations are not biased to one particular realisation of shape noise. Across simulation suites for different neutrino mass and baryonic physics we keep the same positions and the same five sets of random seeds for the shape noise.

CHAPTER 5

STUDYING THE DISTRIBUTION OF MASS AT THE OUTSKIRTS OF CLUSTERS USING COSMO-OWLS

The material in the section has been taken from our paper listed at the end of Section [1.5](#): an original version (MNRAS submitted: MN-19-1088-MJ).

This chapter is concerned with our analysis of the DK profile and how well it describes synthetic stacked cluster lensing signals, and determining whether DK fits can be made to upcoming observational data.

5.1 Stacking Cluster Signals Without Scaling

Realistic clusters are not spherical, and mass estimates from weak lensing fits using a spherical model generally have high scatter with small bias. However, we can determine the mean signal of clusters better than any individual cluster which can have low signal to noise for individual measurements, by taking the weighted average of many clusters' signals - a method called stacking. This process increases the signal to noise by averaging out any shear due to substructure unrelated to the lens, and the impact of triaxiality. Though we lose information of individual clusters with this method, we can obtain more precise estimates on the average behaviour of the stacked clusters. In this chapter we follow the method in [Niikura et al. \(2015\)](#):

$$\langle \Delta \Sigma(R) \rangle = \frac{1}{N} \sum_{a=1}^{N_c} \sum_{s_a; \mathbf{R}_{(a)s_a} \in R'} w_{(a,s_a)} \Sigma_{\text{cr}(a)} \epsilon_{(s_a)+}(\mathbf{R}_{s_a}) \quad (5.1)$$

where the first summation $\sum_{a=1}^{N_c}$ is over each cluster a in the stack with N_c clusters, while the second $\sum_{s_a; \mathbf{R}_{(a)s_a} \in R'}$ runs over the background galaxies s_a , that belong to cluster a , that reside in the preset radial bins R' . The tangential ellipticity of the s_a th source galaxy of

cluster a at position \mathbf{R}_{s_a} is $e_{(s_a)+}(\mathbf{R}_{s_a})$. The normalization factor is defined as

$$N = \sum_{a=1}^{N_c} \sum_{s_a; |\mathbf{R}_{(a)s_a}| \in R'} w_{(a,s_a)}, \quad (5.2)$$

with the weight factor for each background galaxy in a cluster adopted from [Okabe and Smith \(2016\)](#)¹

$$w_{(a,s_a)} = \frac{1}{\Sigma_{\text{cr}}^2(z_a, z_{s_a})(\sigma_{(s_a)\epsilon}^2 + \alpha_{\text{noise}}^2)}. \quad (5.3)$$

z_a and z_{s_a} are the redshifts of the a th cluster and s_a th background galaxy respectively. For the s_a th source galaxy, $\sigma_{(s_a)\epsilon}$ is the measurement error, and α_{noise} is the constant factor that regularizes the weight. For this chapter we set $\sigma_{(s_a)\epsilon}$ to a constant for all galaxies and $\alpha_{\text{noise}} = 0.4$ (Similar to [Niikura et al., 2015](#); [Okabe et al., 2010](#)) in Equation [5.3](#). With $\Sigma_{\text{cr}(a)}$ a constant throughout this chapter (redshifts are constant), this makes the weight a constant value and will be factored out with N . In practice the redshifts and measurement uncertainties, $\sigma_{(s_a)\epsilon}$, would be provided from observational data.

The stacked radial bins is given as

$$R \equiv \frac{1}{N} \sum_{a=1}^{N_c} \sum_{s_a; |\mathbf{R}_{(a)s_a}| \in R'} w_{(a,s_a)} R_{(a)s_a}, \quad (5.4)$$

where $R_{(a)s_a}$ is the position of the background galaxy s_a from the center of cluster a .²

The statistical uncertainty of the stacked lensing at each radial bin is estimated as

$$\sigma_{\langle \epsilon \rangle}^2(R) = \frac{1}{2N^2} \sum_{a=1}^{N_c} \sum_{s_a; |\mathbf{R}_{(a)s_a}| \in R'} w_{(a,s_a)}^2 \epsilon_{(s_a)}^2(\mathbf{R}_{s_a}). \quad (5.5)$$

It is important to note that Equations [5.1](#) and [5.5](#) are functions of stacked radial bins R (Equation [5.4](#)).

¹This differs slightly from [Niikura et al. \(2015\)](#) by the ellipticity amplitude $\epsilon_{(s_a)}^2$. The ellipticity amplitude in the weight is not included in this chapter.

²In this chapter we use a common redshift of clusters and of sources, so $\Sigma_{\text{cr}(a)}$ essentially becomes factored out. So we are taking the weighted average positions of sources in the bins set by R' .

5.2 Stacking Cluster Signals With Scaling

Niikura et al. (2015) shows that stacking with NFW scaling will have less scatter as opposed to the stacking without scaling method and that the NFW profile describes stacked clusters (with or without scaling) out to the virial radius very well. Furthermore, for reasonable parameters in stacking, the DK and NFW profiles (ρ , Σ , γ , and g) agree with each other out to the virial radius. With this process, we can scale the lensing data with the common scaling factor $\frac{\Sigma_{cr}}{2\rho_c r_s}$ (in Equation 2.25) and study the non-analytic DK reduced shear form $F^{DK}(x, \vec{\pi})$. The parameters $\vec{\pi}$ (in the form, see Section 2.3) is determined by fitting the stack, Equation 5.1, with the NFW profile.

Stacked weak lensing with NFW scaling reduces scatter of the reduced shear signals going into the stack. Haloes in simulations exhibit a high degree of self-similarity (e.g., NFW) when scaled appropriately. Therefore the expectation when we scale before stacking is that the diversity (or spread) in the profiles will be minimised (Niikura et al., 2015, Figure 4).

The stack with NFW scaling will be represented as $\langle F(x) \rangle$, instead of the individual halo form $F(x)$ (Equation 2.25). The stacked reduced shear with scaling follows as

$$\langle F(x) \rangle = \frac{1}{N} \sum_{a=1}^{N_c} \sum_{s_a; |\mathbf{x}_{(a)s_a}| \in x'} \frac{w_{(a,s_a)} \Sigma_{cr(a)} \epsilon_{(s_a)+}(\mathbf{x}_{s_a})}{2\rho_c(M_{(a)}, c_{(a)}) r_s(M_{(a)}, c_{(a)})}, \quad (5.6)$$

where $\epsilon_{(s_a)+}(\mathbf{x}_{s_a})$ is the tangential ellipticity of a source galaxy at position $\mathbf{x}_{s_a} = R/r_s(M_{(a)}, c_{(a)})$, and the parameters $(M_{(a)}, c_{(a)})$ are the NFW M_{200c} and concentration fit parameters for cluster a (see Section 5.3.1 for details on fits). In the case of stacking with scaling, the second summation in the normalization N is over $s_a; |\mathbf{x}_{(a)s_a}| \in x'$.

$$x \equiv \frac{1}{N} \sum_{a=1}^{N_c} \sum_{s_a; |\mathbf{x}_{(a)s_a}| \in x'} w_{(a,s_a)} x_{(a)s_a}, \quad (5.7)$$

Diemer and Kravtsov (2014, Figure 3) shows that scaling the mass density profiles by ρ_m and the radial bins by r_{200m} can reduce scatter for the outskirts of haloes. We studied the

stacking results with r_{200m} and r_s and found that scaling with r_{200m} gives slightly better χ^2 results than r_s . However, when the ratios of the simulation run χ^2 over the mean ideal halo stacks $\overline{\chi^2}$ are taken (which will be further discussed in Section 5.5), we get roughly similar results with both scaling methods. For consistency, throughout this chapter we will scale with r_s .

We find that the resulting stacks using scaling even when using ideal NFW or DK haloes do not agree with the NFW or DK forms. The disagreement is due to parameter estimation of M_{200c} and c , and therefore r_s .³ However this disagreement can be mitigated when using ratios of the χ^2 results with respect to the $\overline{\chi^2}$ results of ideal DK haloes (see Section 5.5).

The errors of the stack at each x can then be obtained from

$$\sigma_{(F)}^2(x) = \frac{1}{2N^2} \sum_{a=1}^{N_c} \sum_{s_a; |\mathbf{x}_{(a)s_a}| \in x'} \frac{w_{(a,s_a)}^2 \Sigma_{cr(a)}^2 \epsilon_{(s_a)}^2(\mathbf{x}_{s_a})}{4\rho_c^2(M_{(a)}, c_{(a)}) r_s^2(M_{(a)}, c_{(a)})}. \quad (5.8)$$

Both Equations 5.6 and 5.8 are functions of Equation 5.7.

5.3 Fitting Method

To obtain the parameters that describe the profiles in Section 2.2, we use the background galaxy ellipticities, described in Section 4.1. This is done by azimuthally averaging the tangential shear with $N = 300$ galaxies per bin to obtain $g(r)$ (Equation 2.10) for cluster a , then fitting the data with $g^{NFW}(r)$ to obtain the free parameters (M_{200c}, c) for each cluster, or ($M_{(a)}, c_{(a)}$). Throughout this dissertation we fit with the NFW profile to the inner region since the fitting process is much faster than using the DK profile (NFW shear is analytic) and the parameter estimation is similar to the DK profile anyway. With these parameters we can calculate the scaling factor $\frac{2\rho_c r_s}{\Sigma_{cr}}$ in Equation 2.25 using Equation 2.16, Equation 2.22 and $r_s = r_{200c}/c$. The fit ranges are set to $0.20 < r[\text{Mpc}] < 2.30$ and $0.75 < r[\text{Mpc}] < 3.00$

³This was tested by following this stacking process with one run using weak lensing parameter estimates and another run using true parameters

for LSST-like surveys and WtG-like surveys respectively. The LSST-like lower limit of the fit range was taken from [Niikura et al. \(2015\)](#) while the higher fit range is from the highest value of r_{200c}^{3D} from the simulation catalog. The fit range from the WtG sample is from [Applegate et al. \(2014\)](#). The two fit ranges used in this chapter do not have a significant impact on the stacking results. The error for the fits is determined from the variance from binning and the number of galaxies per bin, σ/\sqrt{N} . Throughout this chapter we use the public module `LmFit`⁴ as the fitting tool ([Newville, Stensitzki, Allen, and Ingargiola, 2014](#)). The fitting function used in `LmFit` minimizes the sum of squared residuals:

$$\mathcal{L} = \sum_i \frac{(\langle\epsilon\rangle_i - g_i^{NFW})^2}{\sigma_i/\sqrt{N_i}}, \quad (5.9)$$

where $\langle\epsilon\rangle_i$, g_i^{NFW} , and $\sigma_i/\sqrt{N_i}$ are the average tangential ellipticities, predicted NFW reduced shear, and error in bin i

5.3.1 Parameterized Mass Model Fits

Throughout this chapter we use the public module `LmFit`⁵ as the fitting tool ([Newville, Stensitzki, Allen, and Ingargiola, 2014](#)), where both the fits and the error bars are determined from the module. The Cosmo-OWLS synthetic cluster lensing data used in this chapter will be one of the LSST-like runs with true mass range for the sample of the 50 most massive clusters being $4.04 < M_{200c}^{3D}[10^{14}M_\odot] < 17.4$ with an average of $\langle M_{200}^{3D}[10^{14}M_\odot] \rangle = 6.64$. The true mass of a cluster, M^{3D} , is calculated by finding the particle deepest in the potential well of a cluster, and calculating the density within spherical shells around the particle. Once the average mass density becomes $200\rho_c$, the corresponding radius is r_{200c}^{3D} and the mass enclosed is M_{200c}^{3D} . There are no true concentrations calculated for the simulations for cluster-to-cluster comparisons.

⁴The `LmFit` package is Free software, using an Open Source license

⁵The `LmFit` package is Free software, using an Open Source license

Figure 5.1 and Figure 5.2 show individual mass estimates compared with true mass for an AGN 8.0 LSST-like run. The many other runs with different noise realizations yield similar results. The red squares and blue points and error bars are the DK and NFW M_{200c} estimates respectively. The plots show that the DK and NFW fits agree well with one another for lower masses, and differ from one another for higher masses. For higher masses, the DK fits give lower masses than the NFW does. Note that we fix the outer DK parameters s_e and b_e for this section.

Figure 5.3 shows the NFW and DK fit parameters. The NFW and DK parameters are marked by circles and dots respectively, connected by lines. Differences in fits in the x or y-directions reflect on the difference in estimates for mass and concentrations respectively. For lower mass clusters the DK and NFW mass estimates are similar, which is what we would expect if the DK and NFW shear profiles are similar in this mass range (see Section 2.3). For the largest mass clusters, the difference between the mass estimates tend to be higher. For the entire mass range we find that the DK mass estimates do better than the NFW. The overall bias (arithmetic average) of NFW mass estimates in this sample is $\approx 15\%$ (biased high), which is large in magnitude, but the sample includes two extremely triaxial clusters with the long axis close to the line-of-sight. Once these are excluded, the bias drops to $\approx 10\%$. For the DK the bias is $\approx 10\%$ (high bias) including all clusters and $\approx 5\%$ for excluding the two triaxial clusters. Throughout this chapter we keep all of the 50 clusters in our stacking process and there is a significant scatter in the biases from run to run. When we have a larger sample of 300 clusters our bias drops significantly. For simulated clusters we found the bias for NFW and DK profiles to be overestimating by $\approx 7\%$ and $\approx 5\%$ respectively.

5.3.2 Extreme Galaxy Clusters in Cosmo-OWLS

Many of the clusters significantly depart from spherical, and as detailed in Lee et al. (2018), the moments of inertia were calculated for each of the clusters, giving descriptions as ellip-

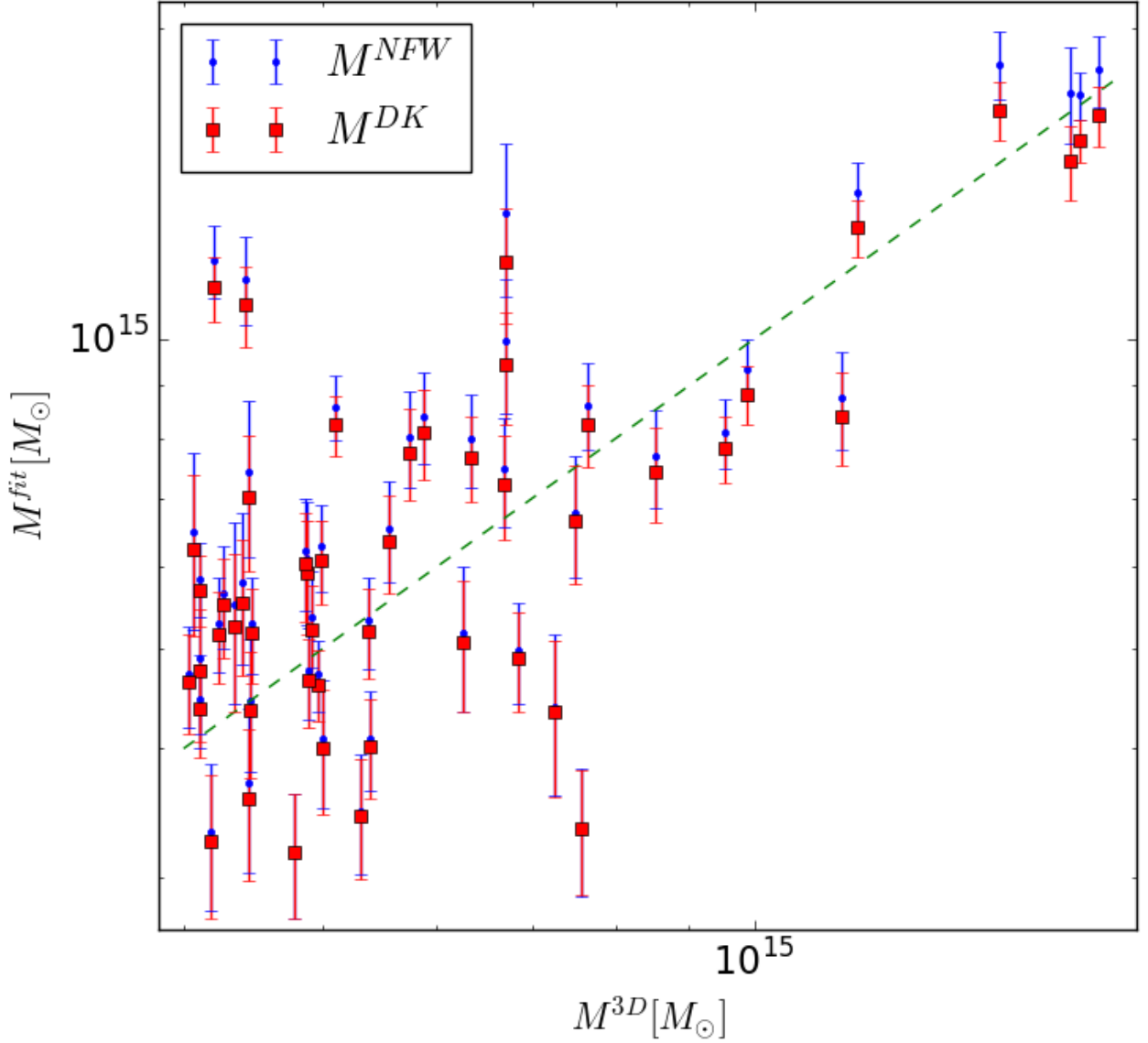


Figure 5.1: The red squares and blue points values plotted here are the DK and NFW mass estimates respectively versus the true masses from the simulation. The green dotted line is $y = x$. In this example, we consider the run with AGN 8.0 for LSST-like surveys and for the 50 most massive clusters in the sample. This shows that the DK fits prefer a lower mass estimate than that of the NFW. This trend is similar with other runs.

soids with ratios for the major, intermediate and minor axes, along with their orientation in 3D and with respect to the z-axis along which the cluster mass is projected. Of the 50 most massive clusters we found that there are two clusters in this sample that are extremely tri-

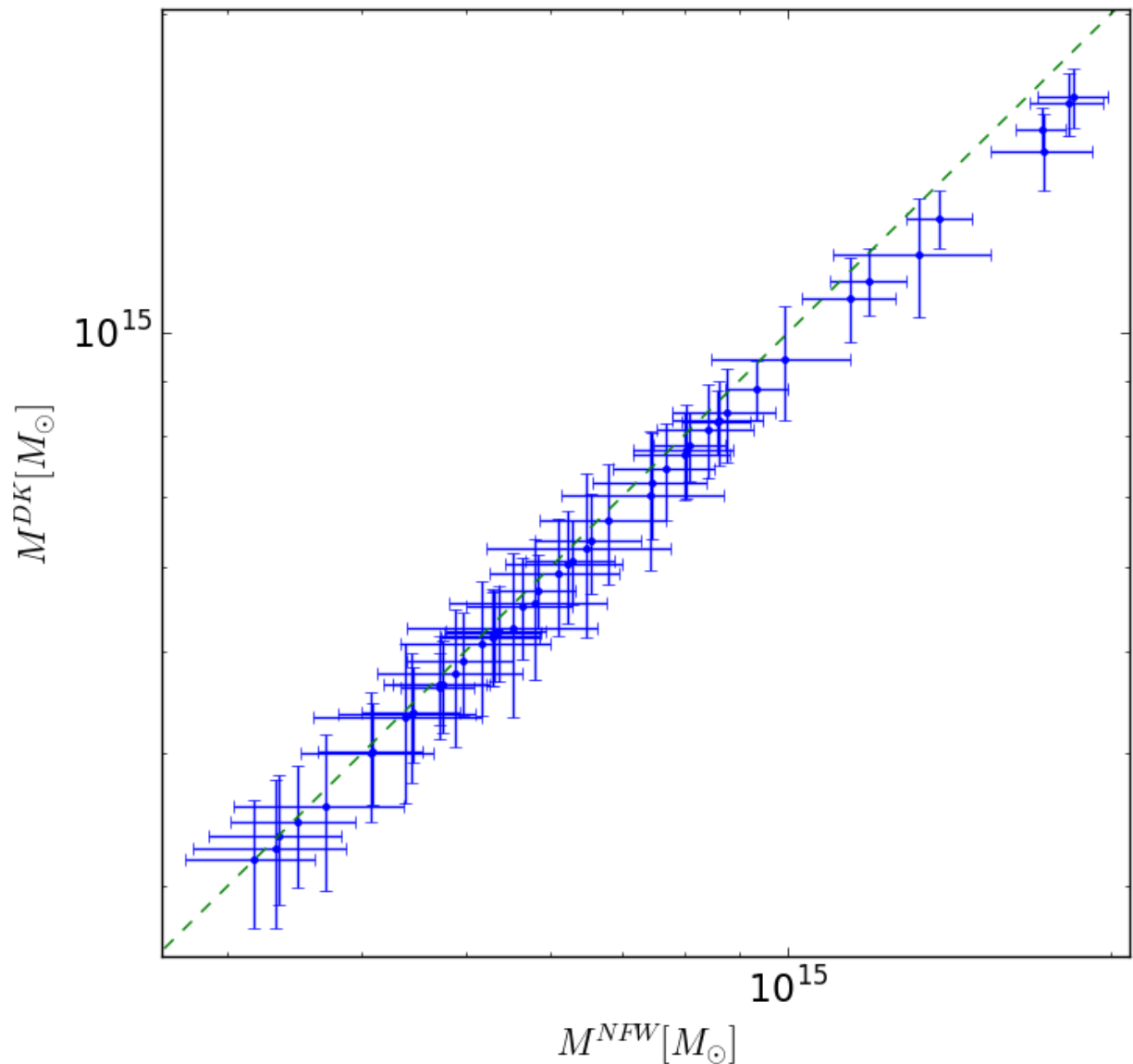


Figure 5.2: This plot is using the same data as Figure 5.1. The green dashed line is $y = x$ and the blue points with error bars are the DK vs. NFW fit mass estimates. For the lower mass clusters (of the 50 most massive clusters in the simulation), the DK and NFW masses are in agreement. For higher masses, their estimates begin to diverge, showing that for the highest mass clusters DK mass estimates are lower than the NFW.

axial, and their major axes are aligned close to the line of sight. As noted above, when their synthetic lensing data are omitted, the average bias and error drop significantly. Figure 5.4 shows a convergence map for one of the highly triaxial clusters. The three different arrows

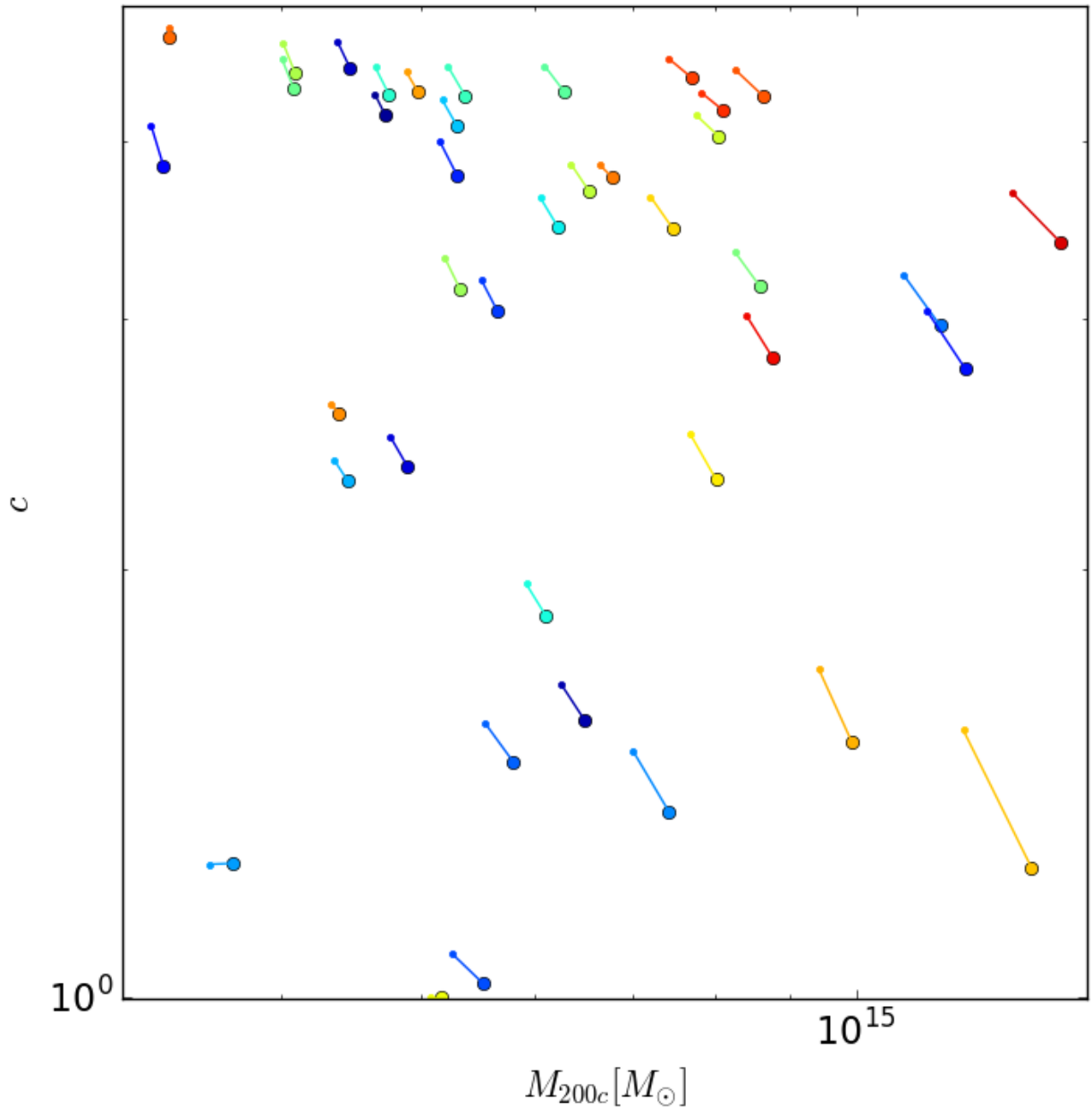


Figure 5.3: This figure is over the same run as Figures [5.1](#) and [5.2](#). The NFW and DK fit parameters are marked by larger circles and smaller points respectively, where each cluster fit results are connected by lines of the same colour. Differences in fits in the x or y-directions reflects on the difference in estimates for mass and concentrations respectively. This plot shows that the NFW and DK profiles agree with mass and concentration estimation for lower mass bins (of the 50 most massive clusters) and the DK profile prefers a lower mass for higher mass bins, preferring higher concentrations to compensate. Also it looks like the DK profile generally prefers in a lower mass than the NFW throughout this cluster sample, though that is not always true in general.

represent the physical projection of the major, intermediate, and minor axes in the xy-plane. Note that the shortest arrow corresponds to the major axis, indicating that the major axis is close to the line-of-sight as black, gray, and white respectively. From the moment of inertia tensor, the minor and intermediate to major axis ratios are 0.45 and 0.62 (Lee et al., 2018). In addition the masses determined from the projections in the xz and yz-planes are significantly different. However, since in practice we would not be able to identify these clusters as highly triaxial, we keep them in our analysis. With huge samples of galaxy clusters expected from future surveys many clusters can be stacked to study mass profiles. The results from Corless and King (2007) indicate that stacking at least 100, and more ideally 500, clusters in a particular mass range would negate the impact of triaxiality on the determination of masses from a sample. We are currently investigating improved triaxial models for individual clusters, derived from lensing, X-Ray, Sunyaev-Zel’dovich and other cluster data.

5.4 Ideal DK Lensing Data Sets

Before detailing the simulation results we explore how both stacking methods work with ideal DK haloes. We use the 50 most massive clusters in the sample and determine their concentrations using DK14 $M - c$ relation. Then we generate ideal DK data sets and follow the steps in Section 4.1 for LSST-like runs with realistic shape noise levels. We follow the steps in Sections 5.1 and 5.2.

In Figure 5.5 the green points are $\langle \Delta\Sigma(R) \rangle$ (stack without scaling), scaled by $2\rho_c r_s$ determined by fitting onto the stack, with error bars $\sigma_{\langle \epsilon \rangle}$. The fit range for each stack depends on the type of run and can be found in Section 5.3; in this case the fit range is set to $0.20 < r[\text{Mpc}] < 2.30$. The thick black curve is $F^{DK}(x, \vec{\pi})$ (DK form) and, for reference, the red curve is $F^{NFW}(x)$ (NFW form). The parameters used in $F^{DK}(x, \vec{\pi})$ is determined from the NFW fit results onto the stack ($r_s[\text{Mpc}] = 0.50$). The stack uses 64 bins and the χ_{red}^2 of the stack to $F^{DK}(x, \vec{\pi})$ is 1.09. We use $d.o.f. = 64 - 2$ for the DK form because of

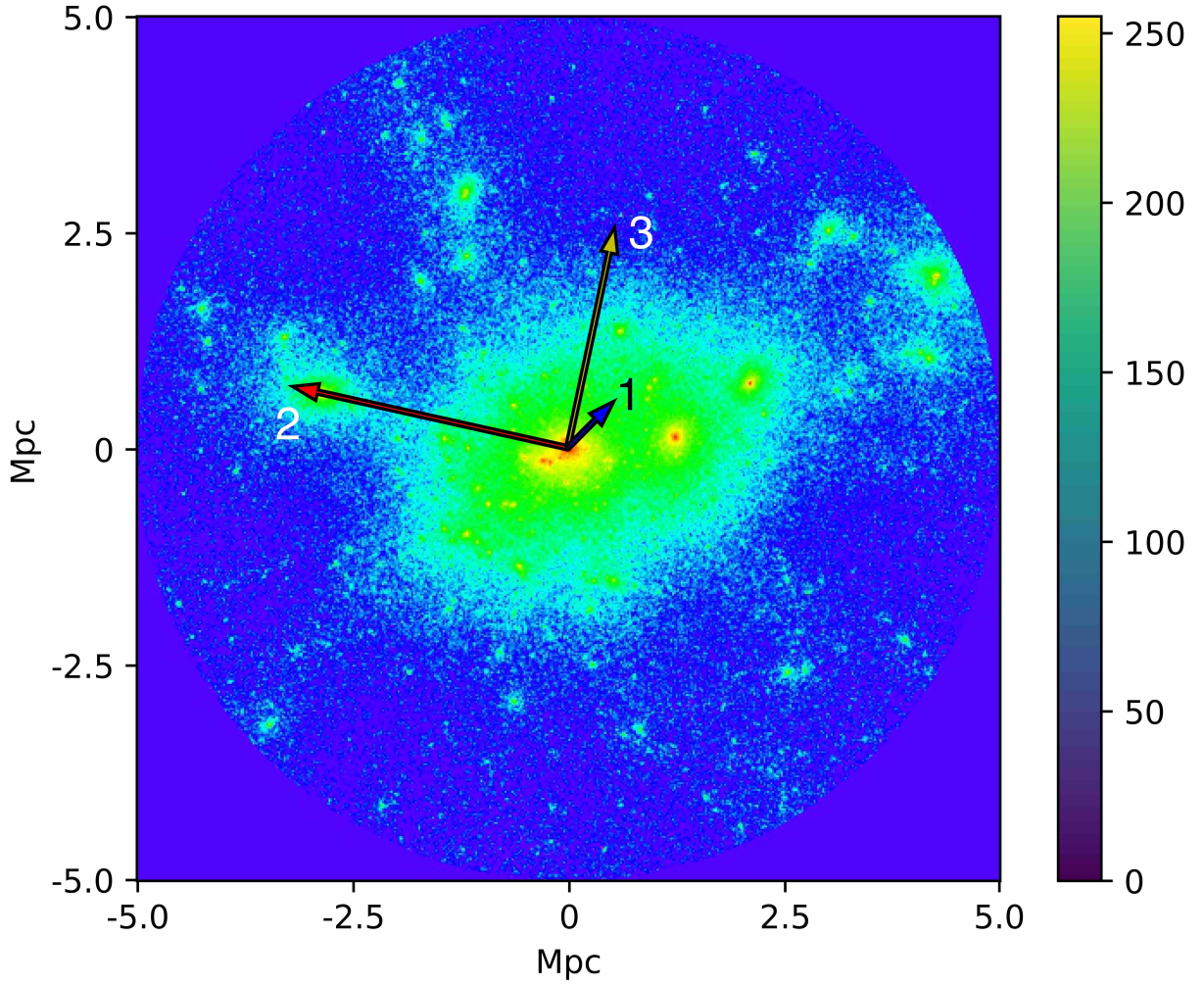


Figure 5.4: κ map of a simulated cluster in xy projection overlaid with a vector representation of the cluster axes in projection. The κ map is zoomed into a radius of 5 Mpc. The arrows labelled 1, 2, and 3 represent the major, intermediate, and minor axes respectively. The axes have been scaled according to their respective eigenvalues. Though longest in 3D space, the major axis appears shortest in projection because it lies in a similar direction to the line of sight (z axis). This leads to a large error in mass estimation when using a spherical model.

the parameter, $\vec{\pi}$, dependency. This shows that $F^{DK}(x, \vec{\pi})$ represents the stacked signals of ideal DK haloes. This has been done over eight total runs with $\overline{\chi_{red}^2} = 1.06$.

In Figure 5.6 the green points are $\langle F(x) \rangle$ (stack with scaling) with error bars $\sigma_{\langle F \rangle}$. The thick black curve is $F^{DK}(x, \vec{\pi})$ (DK form) and, for reference, the red curve is $F^{NFW}(x)$ (NFW form). The parameters is the same as above (determined by NFW fitting the normal

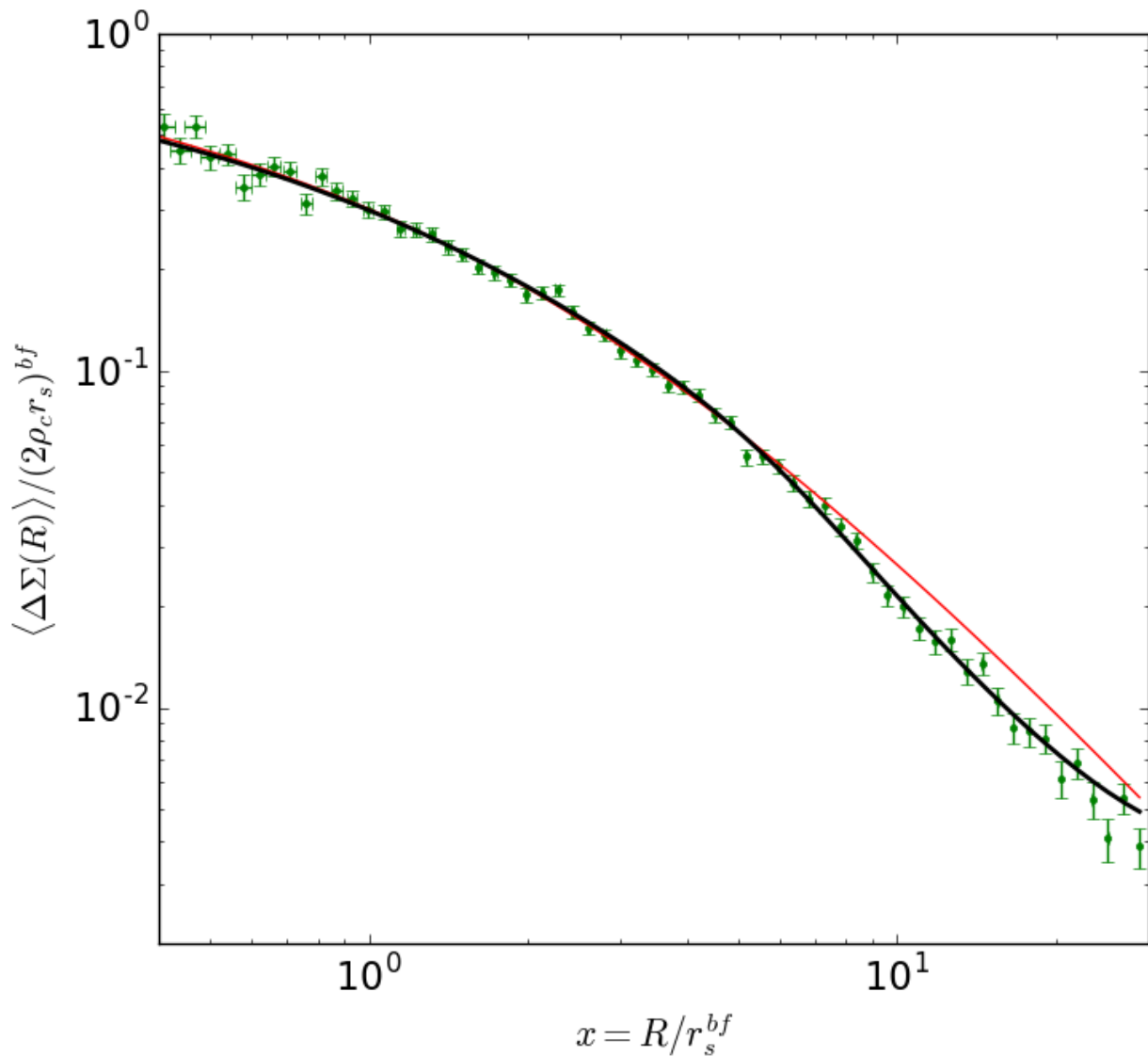


Figure 5.5: Stack without scaling (Section 5.1) for ideal DK haloes. The green points are $\langle \Delta \Sigma(R) \rangle$ (stack without scaling) scaled by $2\rho_c r_s$ (determined by fitting onto the stack), to compare with $F(x)$. The corresponding error bars is $\sigma_{\langle \epsilon \rangle}$. The thick black curve is $F^{DK}(x, \vec{\pi})$ (DK form) and, for reference, the red curve is $F^{NFW}(x)$ (NFW form). This shows that stack without scaling for ideal DK haloes is well represented by the DK form.

stack). $\chi_{red}^2 = 4.36$ of the stack to $F^{DK}(x, \vec{\pi})$ with $d.o.f. = 64 - 2$, for the 64 bins and the parameters $\vec{\pi}$ dependency. For eight total runs $\overline{\chi_{red}^2} = 8.63$. This shows that stack with scaling, using weak lensing mass and concentrations estimates, for ideal DK haloes is not well represented by $F^{DK}(x, \vec{\pi})$. When we use the true parameters, the χ_{red}^2 values are reduced,

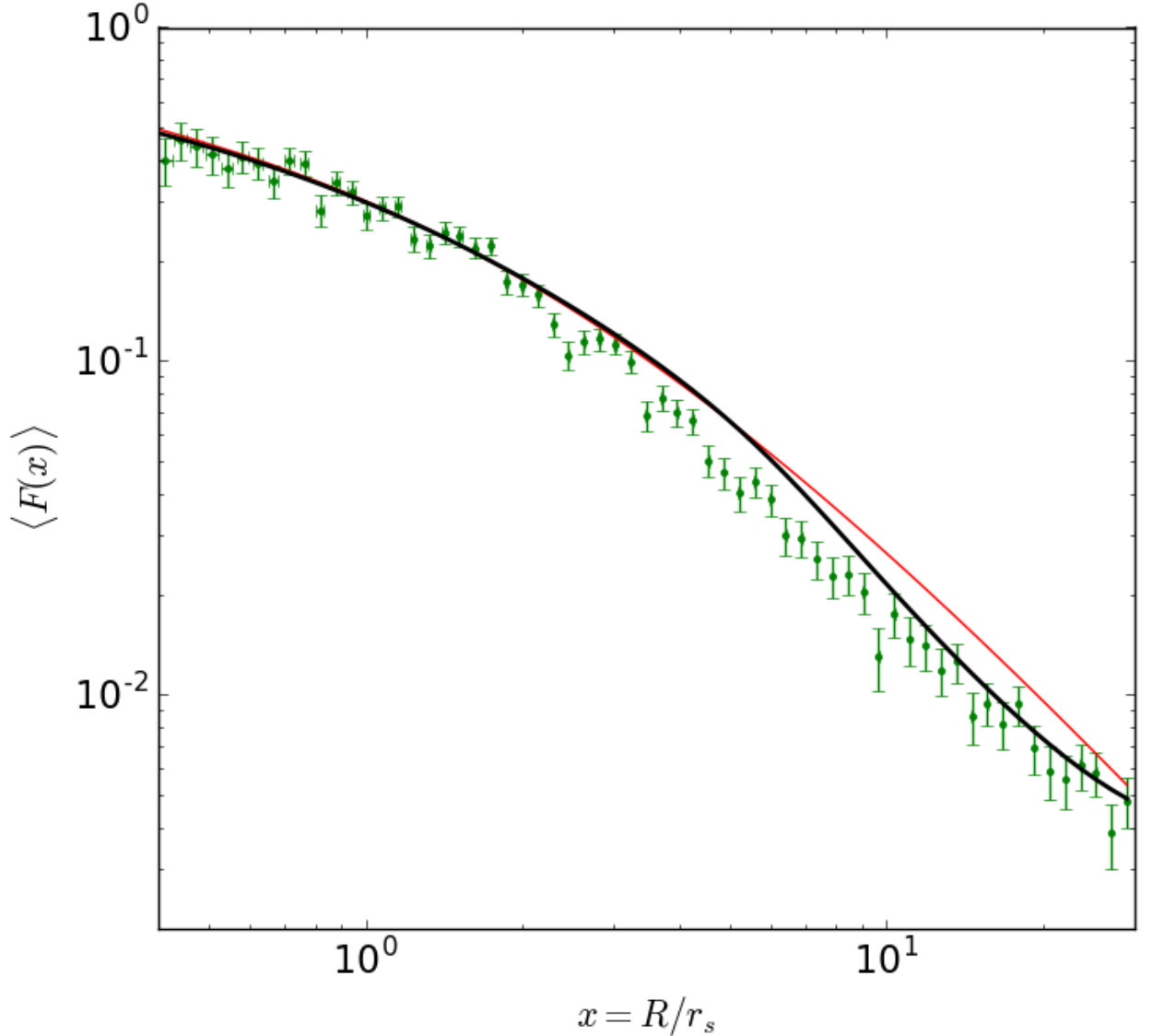


Figure 5.6: stack with scaling ($\langle F(x) \rangle$, Section 5.2) for ideal DK haloes. The green points are $\langle F(x) \rangle$ with the corresponding error bars $\sigma_{\langle F(x) \rangle}$. Even with ideal DK haloes, stack with scaling is not well represented by the DK form. This is likely due to the bias in parameter estimation that is needed for $\langle F(x) \rangle$ and parameter dependency in the DK form (i.e., each signal that goes into stack may have different concentrations and therefore different profile shapes, see Section 2.3). The parameters used in the DK form is determined by fitting over the stack without scaling (Figure 5.5).

with an average of 1.74. stack with scaling likely is not well represented by $F^{DK}(x, \vec{\pi})$ due to the difficulty in accurately estimating the parameters and that the shear form is dependent

on parameters $\vec{\pi}$. The spread in parameters $\vec{\pi}$ values can be seen outside r_{200c} ($= 1.69$ Mpc) (see Section 2.3), where the stack dips below the NFW and DK forms. Since the shear form depends on M_{200c} and c outside $\sim r_{200c}$, the form varies for each individual signal outside of that. This may cause the stacked signals to differ from that of $F^{DK}(x, \vec{\pi})$ (DK form), where c is determined from the fit onto $\langle \Delta\Sigma(R) \rangle$ (stack without scaling).

The DK form performs better for the stack without scaling, $\langle \Delta\Sigma(R) \rangle$ (then scaled by the best-fit parameters to the stack itself), as opposed to stack with scaling, $\langle F(x) \rangle$, for ideal DK haloes when using weak lensing parameter estimation. The DK form is better represented by stack with scaling when we use the exact parameters that created the haloes in the first place, but still not as good as stack without scaling. *So for the rest of this chapter we will focus on the stacking without scaling method, $\langle \Delta\Sigma(R) \rangle$.*

There is another DK scaled mass density form proposed by Umetsu and Diemer (2017) that gives would give good results when stacking very massive clusters. However, for the mass range considered here, we have tested that even though stacking with scaling works for ideal NFW haloes in the absence of noise, the individual cluster parameters are too poorly constrained with realistic noise for stacking to be viable.

5.5 Stacking Without Scaling for AGN 8.0 Cluster Lensing Data

In this section we look at the 50 most massive clusters in a single LSST-like run over the AGN 8.0 simulation while setting the radial bins as $0.20 < R'[\text{Mpc}] < 15.0$ in 64 bins. For illustration we look at the results with no shape noise, or $\epsilon^s = 0$ in Equation 2.8. In Figure 5.7 we follow Section 5.1. The thin curves are the individual cluster signals and the thick green curve is the stack without scaling ($\langle \Delta\Sigma(R) \rangle$, Equation 5.1), all scaled by the best fit parameters to the stack. The thick red curve is the same NFW form, $F^{\text{NFW}}(x)$ in Equation 2.25. Here, $\langle \Delta\Sigma(R) \rangle$ (stack without scaling) is scaled by $2\rho_c r_s$ and R is scaled by r_s , parameters determined by fitting to the stack (Equation 5.1), to compare with the DK form,

Table 5.1: Ratios for DK and NFW profile, $\chi_{red}^2/\overline{\chi_{red}^2}$, for the LSST-like runs for AGN 8.0 and DMO simulations. In this section we only have M_{200c} and c as the free parameters for the DK form and we used 64 radial bins for the analysis ($d.o.f. = 64 - 2$). The NFW form doesn't have parameters, so the $d.o.f. = 64$ for NFW. The average χ_{red}^2 values for stack without scaling, $\langle\Delta\Sigma(R)\rangle$, for the ideal DK and NFW halo runs with LSST-like noise are $\overline{\chi_{red}^2} = 1.06$ and 1.26 respectively. The $\overline{\chi_{red}^2}$ values are calculated over eight LSST-like runs but over ideal DK or NFW haloes.

Runs	DK		NFW	
	AGN 8.0	DMO	AGN 8.0	DMO
1	1.41	1.34	2.83	3.46
2	1.01	1.20	3.41	2.50
3	1.18	1.36	2.96	3.10
4	1.20	1.35	2.00	3.47
Avg.	1.20	1.31	2.84	3.13

$F^{DK}(x, \vec{\pi})$ (parameters $\vec{\pi}$ determined by the NFW fit onto the stack for $0.20 < r[\text{Mpc}] < 2.30$ in this case). Using the same parameters, each individual signal is scaled by $2\rho_c r_s/\Sigma_{cr}$ and radial positions by r_s .

Now we include realistic shape noise ($\sigma_\epsilon = 0.25$ in Section 4.1) for the same clusters for one of the runs. These results can be seen in Figure 5.8. This shows that the stack without scaling is very well represented by the DK profile, with $\chi_{red}^2 = 1.08$ and $d.o.f. = 64 - 2$ (NFW: $\chi_{red}^2 = 4.30$ and $d.o.f. = 64$).

To help us determine if the stack is well represented by the DK profile, we use the NFW profile as reference. First, we follow the same procedure in determining the stacks but instead of using simulations we use ideal DK or NFW haloes. We then take an average of their χ_{red}^2 values. To determine if the simulation haloes are more like DK or NFW, we take the ratio of the simulation stack χ_{red}^2 values with the average of the ideal halo runs, $\overline{\chi_{red}^2}$. Therefore, whichever ratio is closer to 1 then the resulting simulation stack behaves more like either the ideal DK or NFW haloes. In Table 5.1 we look at the DK and NFW results for AGN 8.0 and DMO simulations for LSST-like runs, without Large Scale Structure noise. With these ratios it is clear that the mass density profiles of the simulated clusters behave more like the

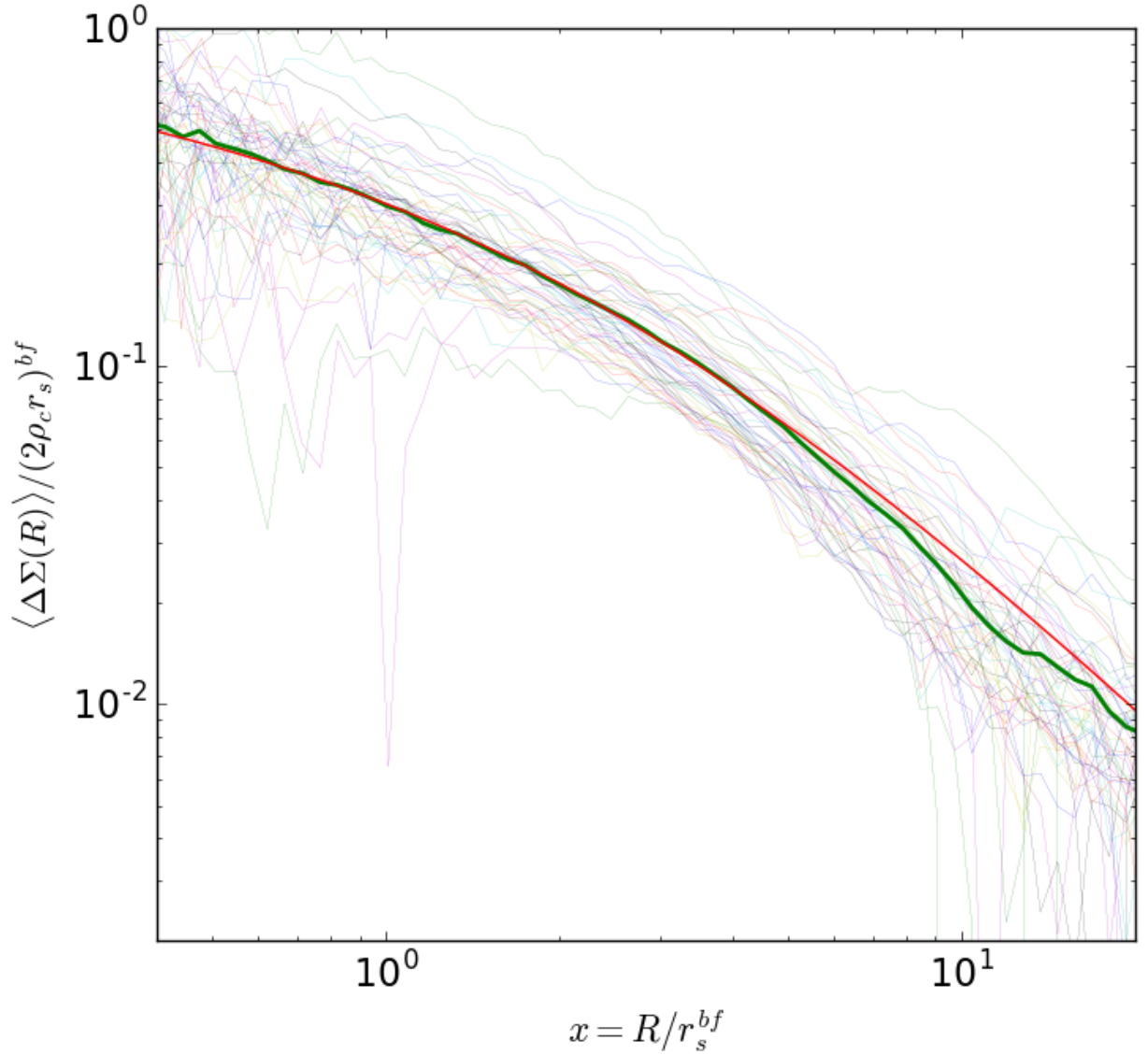


Figure 5.7: Each thin curve represents a cluster’s reduced shear that went into the stack, the thick green curve represents the stack without scaling, and the thick red curve is the NFW form, $F^{\text{NFW}}(x)$. Everything is then scaled using the best fit parameters onto the stack, to compare with $F(x)$. Here we follow Section 5.1 with the 50 most massive clusters with no noise. For simplicity, we omitted error bars to show individual signals compared to the stack without scaling. This plot is an example of how stack without scaling compares with each individual cluster shear profile and the NFW form.

DK profile, but using this analysis it is difficult to determine if baryonic prescriptions have any impact on their overall profile.

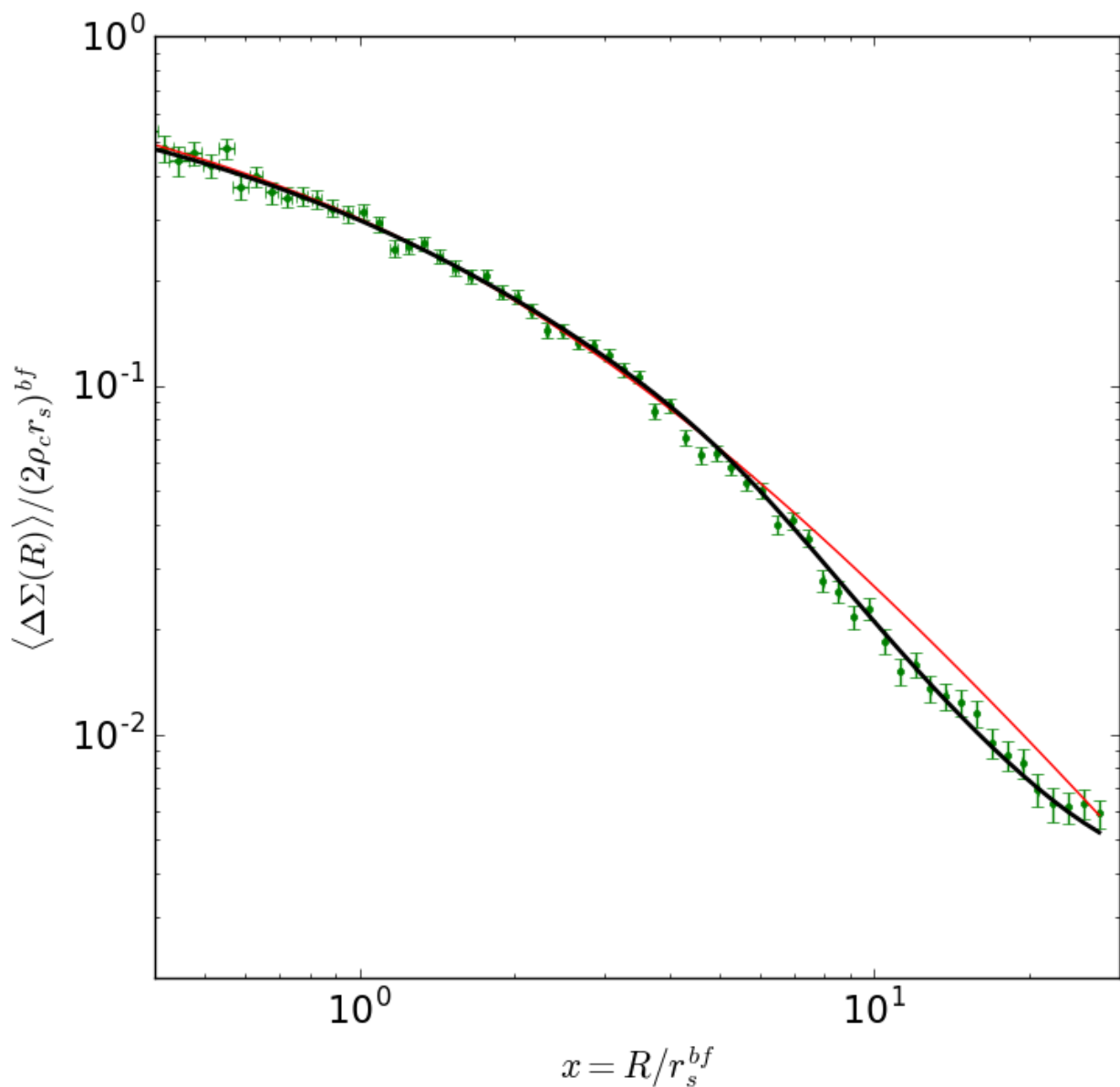


Figure 5.8: This plot uses realistic LSST-like clusters from the AGN 8.0 simulation. The green points are $\langle \Delta \Sigma(R) \rangle$ (stack without scaling, following Section 5.1), scaled by $(2\rho_c r_s)^{bf}$ (so we can compare with $F(x)$) with error bars of $\sigma_{(\epsilon)} / (2\rho_c r_s)^{bf}$ (Equation 5.5). The thick black curve is the DK form, $F^{DK}(x, \vec{\pi})$, and the red curve is the NFW form, $F^{NFW}(x)$. It is clear that the stack is better represented by DK than NFW. The DK $\chi_{red}^2 = 1.08$ with $d.o.f. = 64 - 2$.

Table 5.2: Ratios for DK profile, $\chi_{red}^2/\overline{\chi_{red}^2}$, for the LSST-like runs for AGN 8.0 and DMO simulations. This table is similar to Table 5.1 but with Large Scale Structure noise $\sigma_{LSS} = 0.004$. The average χ_{red}^2 values for stack without scaling, $\langle\Delta\Sigma(R)\rangle$, for the ideal DK and NFW halo runs with LSST-like noise are $\overline{\chi_{red}^2} = 0.57$ and 0.51 respectively. The $\overline{\chi_{red}^2}$ values are calculated over eight LSST-like runs.

Runs	DK		NFW	
	AGN 8.0	DMO	AGN 8.0	DMO
1	1.08	1.13	1.78	1.97
2	0.87	0.96	1.64	1.49
3	0.98	1.17	1.66	1.86
4	0.92	0.97	1.35	1.66
Avg.	0.97	1.06	1.61	1.75

5.6 Impact of Uncorrelated Large Scale Structure

We also look at the results when Large Scale Structure noise σ_{LSS} is included. In real data there would be more noise due to structure along the line of sight, which is not fully accounted for by taking 30 Mpc boxes from the simulations. For simplicity we set $\sigma_{LSS} = 0.004$, typical of the noise at the outskirts of clusters due to LSS in Dodelson (2004); the inner region of the DK and NFW reduced shear forms are very similar anyway and the DK and NFW forms depart toward the outskirts. Another simplification in our treatment of the LSS is that the noise originating from uncorrelated projected LSS (i.e., structures not associated with the clusters themselves) is correlated at various scales, and this is of particular importance at large radii (in excess of $r \approx 10'$; e.g., Hoekstra (2003)). Figure 5.9 is the results for the stacking without scaling method (Section 5.1), with new error bars with σ_{LSS} added in quadrature to the stacked error bars, $\sigma_{\langle\epsilon\rangle}^2$. It is clear that the stack (without scaling) is well represented by the DK profile even when the noise due to large scale structure is included. ($\chi_{red}^2 = 0.50$ and 0.84 for DK and NFW forms respectively. For DK, the *d.o.f.* = $64 - 2$ while for NFW *d.o.f.* = 64). The low χ_{red}^2 values are due to large error bars.

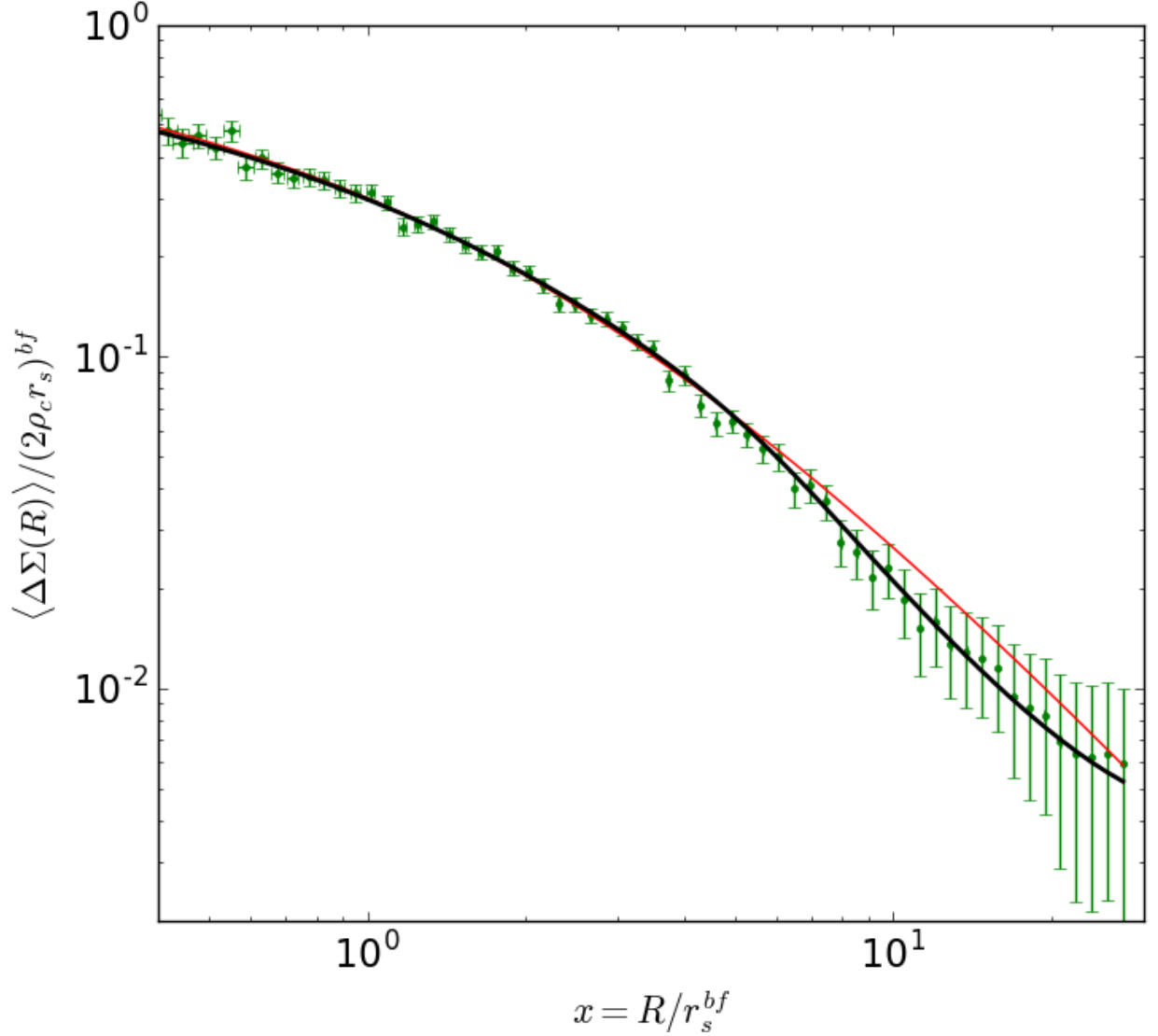


Figure 5.9: This plot uses realistic LSST-like clusters from the AGN 8.0 simulation but with added noise approximating that due to Large Scale Structure (σ_{LSS}). The green points are $\langle \Delta \Sigma(R) \rangle$ (stack with scaling, following Section 5.1), scaled by $(2\rho_c r_s)^{bf}$ (so we can compare with $F(x)$) with error bars as $\sigma_{\langle \epsilon \rangle} / (2\rho_c r_s)^{bf}$ (Equation 5.5) and $\sigma_{LSS} / (2\rho_c r_s)^{bf}$ added in quadrature. The thick black curve is the DK form, $F^{DK}(x)$, and the red curve is the NFW form, $F^{NFW}(x)$. It is clear that the stack is better represented by DK than NFW. The added noise is extremely crude (flat $\sigma_{LSS} = 0.004$), but is included in this plot to show the difficulty in distinguishing between the DK and NFW forms when Large Scale Structure is considered.

Table 5.2 is similar to Table 5.1, but with the addition of noise due to Large Scale Structure. Again we can see that the simulation haloes are more like DK, but it is difficult to tell if baryonic prescriptions have any effect on the shape of them.

Overall the DK profile is a good representation of stacks created without scaling, $\langle \Delta\Sigma(R) \rangle$, of the most massive clusters in the simulations with LSST-like or WtG-like parameters. These conclusions for samples such as WtG will be strengthened with larger samples.

In this section we showed one example of a LSST-like run over the AGN 8.0 simulation with noise levels determined in Sections 5.2 and 5.1. For this work, many variations of stacking with and without scaling, $\langle F(x) \rangle$ and $\langle \Delta\Sigma(R) \rangle$ respectively, have been tested against the DK and NFW forms, $F^{DK}(x, \vec{\pi})$ and $F^{NFW}(x)$ respectively. We see how the inclusion of ellipticity amplitude in the weight (Equation 5.3, as in Niikura et al. (2015)) and how using “true parameters” (or better estimated parameters) as opposed to weak lensing fit parameters effects the overall results. Using ellipticity amplitude in the weight, as in Niikura et al. (2015), has little effect on the χ^2 ratios. Using the “true parameters” does give better χ_{red}^2 values but the ratios and plots are qualitatively the same. We also explore increasing σ_ϵ , from 0 to 0.25, for the Gaussian distribution where we randomly choose the intrinsic ellipticities (see Section 4.1) to see how it effects stack with scaling, $\langle F(x) \rangle$. We find that stack with scaling results still aren’t represented by the DK form due to the parameters $\vec{\pi}$ dependency in $F^{DK}(x, \vec{\pi})$.

5.7 Application of Stacking Without Scaling to Extended Field-of-View WtG-like Data

For WtG-like runs we use $n_0 = 10$ gals/arcmin² instead of LSST-like runs, where $n_0 = 30$ gals/arcmin². The field-of-view used in our simulation is 30 Mpc, more than double that of typical clusters from the WtG survey. Figure 5.10 shows stack without scaling ($\langle \Delta\Sigma(R) \rangle$) in green for a WtG-like run for the AGN 8.0 simulation using the 50 most massive clusters,

Table 5.3: Ratios for DK and NFW profile, $\chi_{red}^2/\overline{\chi_{red}^2}$, for the WtG-like runs for AGN 8.0 and DMO simulations. The DK form has $\vec{\pi}$ as the free parameters and uses 64 radial bins for the analysis, so the *d.o.f.* = 64 – 2. The NFW form does not have any parameters in the form, so the *d.o.f.* = 64. The average χ_{red}^2 values for stack without scaling, $\langle\Delta\Sigma(R)\rangle$, for the ideal DK and NFW halo runs with WtG-like noise are $\overline{\chi_{red}^2} = 1.04$ and 1.13 respectively. The $\overline{\chi_{red}^2}$ values are calculated over eight WtG-like runs but over ideal DK or NFW haloes.

Runs	DK		NFW	
	AGN 8.0	DMO	AGN 8.0	DMO
1	1.33	1.35	1.14	2.12
2	1.37	0.95	1.21	1.72
3	1.05	1.26	2.18	1.54
4	0.73	1.21	1.47	1.28
Avg.	1.12	1.19	1.50	1.67

Table 5.4: Ratios for DK profile, $\chi_{red}^2/\overline{\chi_{red}^2}$, for the WtG-like runs for AGN 8.0 and DMO simulations. This table is similar to Table 5.3 but with Large Scale Structure noise $\sigma_{LSS} = 0.004$. The average χ_{red}^2 values for $\langle\Delta\Sigma(R)\rangle$ for the ideal DK and NFW halo runs with WtG-like noise are $\overline{\chi_{red}^2} = 0.66$ and 0.65 respectively. The $\overline{\chi_{red}^2}$ values are calculated over eight WtG-like runs.

Runs	DK		NFW	
	AGN 8.0	DMO	AGN 8.0	DMO
1	1.34	1.59	1.35	2.07
2	1.12	0.91	1.11	1.29
3	0.96	1.05	1.48	1.24
4	0.76	0.99	1.14	1.08
Avg.	1.05	1.14	1.27	1.42

compared to the DK and NFW forms, the thick black and red lines respectively. To show how the number density effects error bars, we exclude large scale structure noise. With a decrease in number of background sources, the error bars increase (compare with Figure 5.8, where the number density is $n_0 = 30$ gals/arcmin²), rendering the NFW and DK forms indistinguishable from the stack. In order to distinguish between the NFW and DK profiles, we need to either increase the number density of background galaxies or include more clusters.

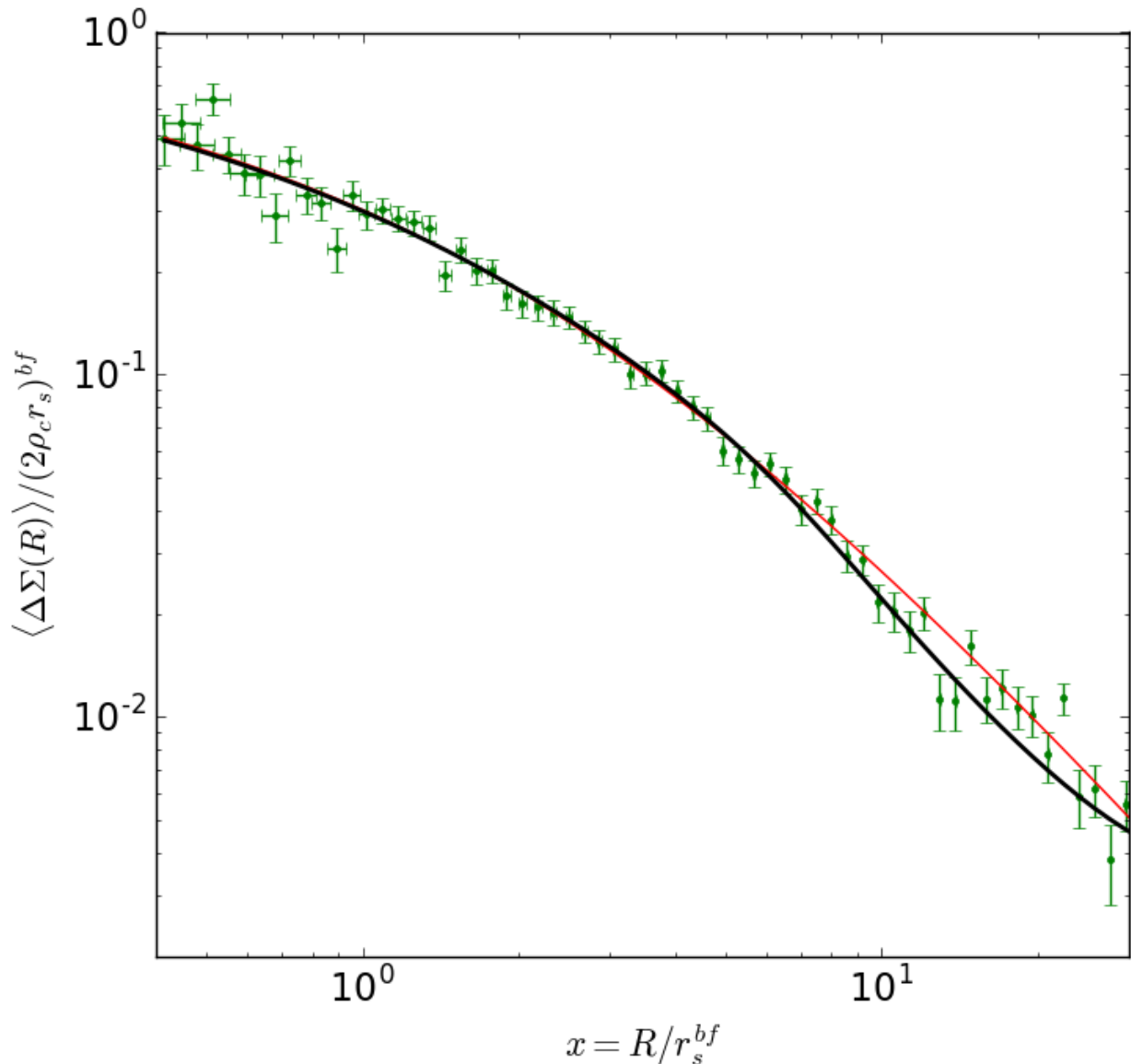


Figure 5.10: Here we plot stack without scaling ($\langle \Delta \Sigma(R) \rangle$, following Section 5.1) in green for a WtG-like run for the AGN 8.0 simulation using the 50 most massive clusters. The thick black and red curves are $F^{DK}(x, \vec{\pi})$ and $F^{NFW}(x)$, the DK and NFW forms, respectively. This shows that with a smaller number density of background galaxies, n_0 , the more difficult it is to distinguish between the NFW and DK forms (Compare with Figure 5.8, where the number density is $n_0 = 30$ gals/arcmin²). So in order to distinguish, we either need to increase the number of sources or include more cluster signals.

Tables 5.3 and 5.4 are similar to the LSST-like runs at the end of Section 5.5. Overall the results are that the DK profile performs better than the NFW when representing the

simulation stacks, though the differences between the ratios are somewhat smaller. So even though the smaller number density of sources and the large scale structure noise both make the χ_{red}^2 values larger, the ratios ($\chi_{red}^2/\overline{\chi_{red}^2} \approx 1$) can be used to show that the WtG-like simulations behave more closely to that of DK than NFW haloes.

Another way that the χ_{red}^2 values can be improved is to simply increase the number of clusters that go into the stack. Throughout this section we have used the 50 most massive clusters from the simulations. Here we show the results of the 300 most massive M_{200c}^{3D} values in the AGN 8.0 simulation for a WtG-like run ($n_0 = 10$ gals/arcmin²). $\langle M_{200c}^{3D} \rangle = 3.30 \times 10^{14} M_\odot$ with $1.97 < M_{200c}^{3D} [10^{14} M_\odot] < 17.35$. Here we exclude the noise due to large scale structure to show how the increase of number of clusters in the stack can effect the error bars. Figure 5.11 shows that, even with the large mass range and lower number density of sources, stacked shear can be used to show that haloes behave more like DK than NFW haloes on large scales, so long as there is a sufficient number of cluster signals to make up for the lower number density of sources (Compare with Figure 5.10, where there are 50 clusters in the stack). In this case we just use the χ_{red}^2 values; χ_{red}^2 are 0.97 and 1.33 for DK (*d.o.f.* = 64 – 2) and NFW (*d.o.f.* = 64) respectively.

Since there are fewer galaxy clusters in the CLASH sample than in the WtG sample, we concur with the conclusions Umetsu and Diemer (2017) regarding the CLASH sample. Even with a wider field of view for a sample such as WtG, it is unlikely that the large scale environment of the clusters could be studied at a level to distinguish between the DK and NFW profile.

5.8 Splashback Radius

In this section we show an example of the splashback radius, r_{sp} , which depends on DK parameters (see Section 2.2). The splashback radius is located at the minimum of the logarithmic derivative of the mass density profile described by the DK model (Diemer and

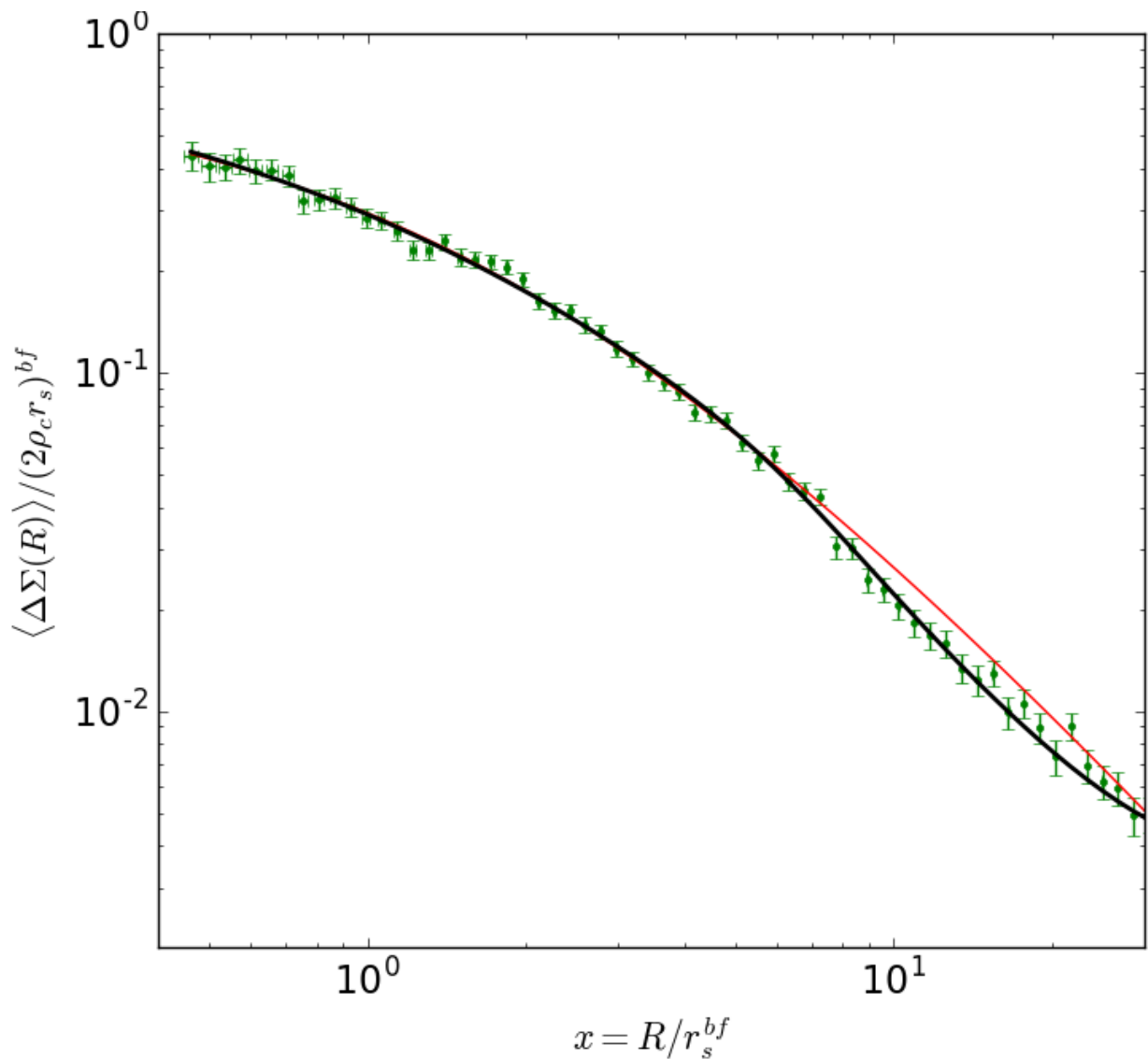


Figure 5.11: This figure is the same as Figure 5.10 but with 300 (as opposed to 50) of the most massive clusters from the AGN 8.0 simulation for a WtG-like run ($n_0 = 10$ gals/arcmin²). $\langle M_{200c}^{3D} \rangle = 3.30 \times 10^{14} M_\odot$ with $1.97 < M_{200c}^{3D} [10^{14} M_\odot] < 17.35$. This figure shows the results for a larger number of clusters with a much larger mass range, where χ_{red}^2 are 0.97 and 1.33 for DK ($d.o.f. = 64 - 2$) and NFW ($d.o.f. = 64$) respectively.

(Kravtsov, 2014). It is a physical boundary where accreted matter reaches its first orbital apocenter (More et al., 2015). This feature can be seen as a sharp drop off in the DK mass density profile and is a function of the mass accretion rate. Therefore studying the DK model and splashback radius can give us interesting information on the growth and other

properties of galaxy clusters (e.g., [More et al., 2015, 2016](#); [Chang et al., 2017](#); [Snaith et al., 2017](#); [Umetsu and Diemer, 2017](#)).

Figure [5.12](#) shows the the splashback radius of the DK profile. Here we use M_{200c}, c, s_e, b_e from fitting the DK model onto $\langle \Delta\Sigma(R) \rangle$ (stack without scaling, following Section [5.1](#)) for realistic LSST-like clusters from the AGN 8.0 simulation Cosmo-OWLS (see Section [5.5](#), Figure [5.8](#), and Table [5.1](#)). Plotted in the top, middle, and bottom panels are the exponential behavior of r for ρ, Σ , and g respectively. The dashed green line is the DK profile using the fit parameters and the solid green line is the NFW profile for reference. The Red dashed vertical line is the truncation radius $r_t = 3.02$ Mpc and the vertical black solid lines are the minimum of the logarithmic derivative of ρ with respect to r for each panel. The true r_{sp} is the minimum of the DK mass density profile (top panel), which is 2.72 Mpc. The middle and bottom panel minima are located at 1.80 and 6.20 Mpc respectively.

5.9 DK Mass Density and Stacking Conclusions

Gravitational lensing is an essential tool for probing the distribution of mass in galaxy clusters, most of which is dark matter. The most commonly used mass density profile to describe cluster scale structures is the NFW profile, which has stood two decades of scrutiny. Advances in the resolution of cosmological simulations, and in the incorporation of physical processes associated with baryonic matter - beyond gravity for dark matter only simulations, have resulted in refinements to the NFW model, for example that of [Diemer and Kravtsov \(2014\)](#).

Gravitational lensing estimates of cluster mass have rather a large scatter, with sources of noise including the finite sampling of the lensing potential by background galaxies which have an intrinsic distribution of shapes. Other factors include triaxiality in 3D, particularly when clusters are very elongated along the line of sight or in the plane of the sky. Besides boosting the lensing signal, and hence the quality of information on the average cluster mass

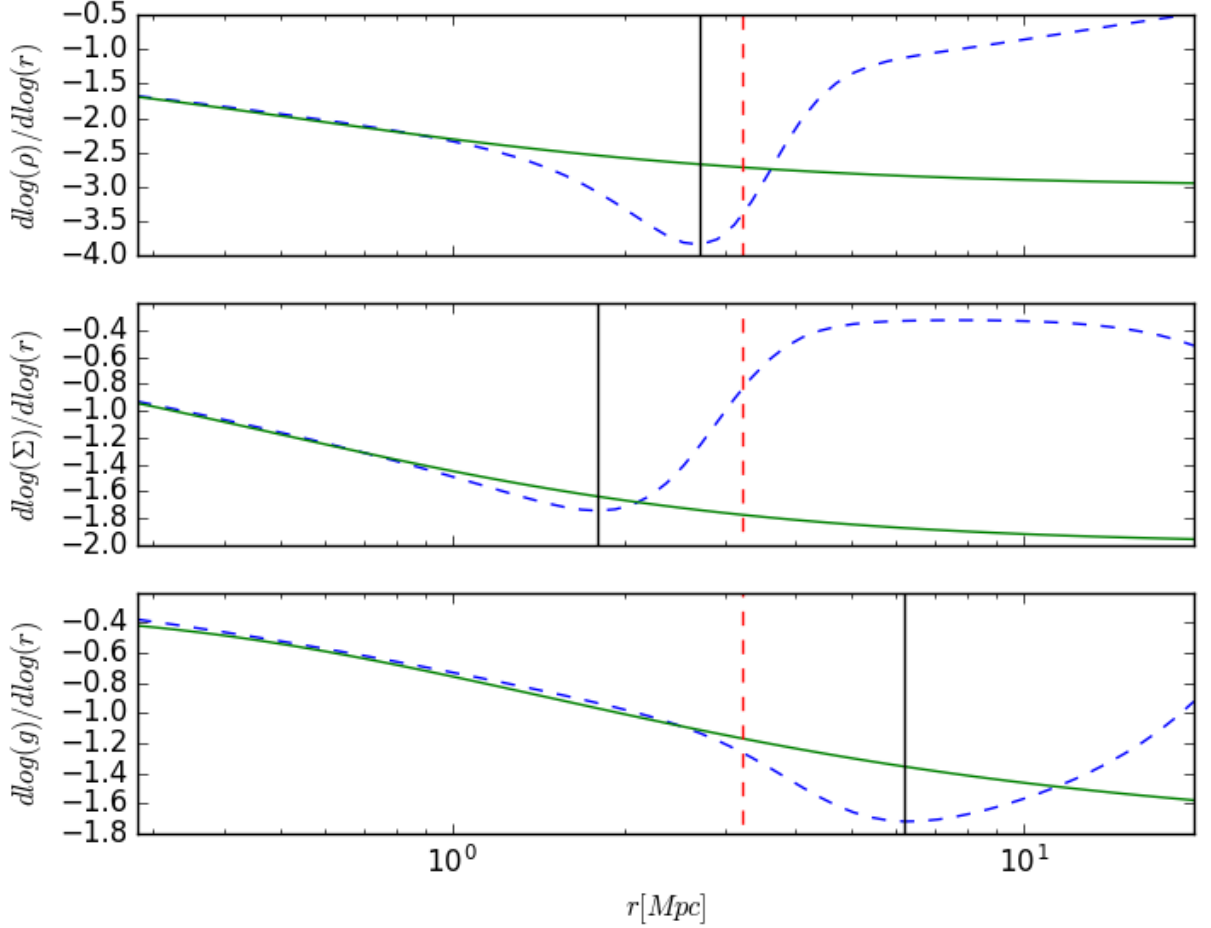


Figure 5.12: The splashback radius of the DK profile using M_{200c} , c , s_e , b_e fit parameters onto $\langle \Delta \Sigma(R) \rangle$ (stack without scaling, following Section 5.1) for realistic LSST-like clusters from the AGN 8.0 simulation Cosmo-OWLS (see Section 5.5, Figure 5.8, and Table 5.1). Plotted in the top, middle, and bottom panels are the exponential behavior of r for ρ , Σ , and g respectively. The dashed green line is the DK profile using the fit parameters and the solid green line is the NFW profile for reference. The Red dashed vertical line is the truncation radius $r_t = 3.02$ Mpc and the vertical black solid lines are the minimum of the exponential behavior of r for each panel. The true r_{sp} is the minimum of the DK mass density profile (top panel), which is 2.72 Mpc. The middle and bottom panel minima are located at 1.80 and 6.20 Mpc respectively.

profile, stacking averages the 3D structure of clusters, assuming that the sample is random on the sky.

In this section we used 50 clusters extracted the cosmological simulations from cosmo-OWLS Le Brun et al. (2014), specifically DMO and AGN 8.0 runs, the latter implementing

feedback from black holes and other baryonic physics. We considered synthetic weak lensing data with background galaxy number density characteristic of the Weighing The Giants survey, and future LSST surveys. Using two different stacking procedures, we compared the accuracy with which NFW and DK models describe the stacked lensing data, and the prospects for measuring a departure from the NFW form. On larger scales, and for stacked lensing data, the DK model gives a more accurate description of the azimuthally averaged shear from WtG-like and LSST-like surveys. In particular for the LSST-like surveys, assuming $n_0 = 30$ gals/arcmin² compared with the $n_0 = 10$ gals/arcmin² for WtG, there are good prospects for detecting features beyond the applicability of the NFW model, in particular the steepening of the mass density profile around the splashback radius. The conclusions are the same for the DMO and AGN 8.0 runs. This is consistent with detailed studies of the lensing signatures of individual clusters from these and other cosmo-OWLS runs (Lee et al., 2018).

The distinction between the lensing signals of NFW and DK models has interesting implications for the estimation of cluster mass, and constraints on the dark matter and other large scale structure surrounding them. As discussed in Diemer and Kravtsov (2014), the parameters of their model are sensitive to the rate at which matter is accreted onto clusters. With large enough samples of clusters, we may be able to identify subsets of those which are more or less rapidly accreting, based on some physical indicator such as blue stellar populations indicative of star formation, and test whether they have distinct DK parameters and the relationship between splashback radius and mass accretion rate. In future work we will stack synthetic and real lensing data sets aligned based on their longest axes on the sky, since filaments tend to preferentially occur close to the major axes of clusters. Preliminary simulations indicate that this will enable us to study the periphery of clusters, and the large scale structures in which they are embedded, in greater detail.

CHAPTER 6

THE IMPACT OF MASSIVE NEUTRINOS AND BARYONIC PHYSICS ON WEAK LENSING PEAK STATISTICS

The material in the section has been taken from our paper listed at the end of Section 1.5: the version on record (Fong et al., 2018).

In this chapter we present the first study that uses cosmological simulations, including both massive neutrinos and baryonic physics, to study weak lensing peak statistics.

6.1 Aperture Mass Statistic

In this section we outline the aperture mass statistic (Schneider, 1996) that we use to measure the weak lensing signal, and how we map the aperture mass over the synthetic surveys. Finally we describe how we determine the weak lensing peaks based on the aperture mass maps.

We can take advantage of the fact that the average shape of unlensed galaxies is circular for a large enough sample, or $\langle \epsilon^s \rangle = 0$. So if we take an ensemble of lensed galaxy shapes, we can recover the reduced shear, $\langle \epsilon \rangle = g$ (see Equation 2.9).

An important tool is the aperture mass (Schneider, 1996), which can be used to map dark and luminous matter. Although not employed in this dissertation, the variance of the aperture mass as a function of aperture scale can be used to constrain cosmological parameters (e.g., see Schneider, 2005, and references therein).

The aperture mass, M_{ap} , is constructed by integrating the weighted convergence within an aperture:

$$M_{\text{ap}}(\vec{\theta}_0) = \int d^2\theta U(\vec{\theta} - \vec{\theta}_0) \kappa(\vec{\theta}), \quad (6.1)$$

where θ_0 is the 2D location of the aperture centre, and U is a weight function that is compensated within the filter radius, smoothly goes to zero at a finite radius, and is zero outside

of that radius. It should be also localised in Fourier space with no oscillatory behaviour in the power spectrum (Leonard et al., 2012). Since the convergence and the shear are related (see Chapter 2), the aperture mass can be expressed as

$$M_{\text{ap}}(\vec{\theta}_0) = \int d^2\theta Q(\vec{\theta} - \vec{\theta}_0) \gamma_+(\vec{\theta}, \vec{\theta}_0), \quad (6.2)$$

where the shear weight function or filter function is $Q(\theta) = \frac{2}{\theta^2} \int_0^\theta d\theta' \theta' U(\theta') - U(\theta)$ and the tangential shear is $g_+ \approx \gamma_+$ in the weak lensing limit.

In practice for real or synthetic observations of lensed galaxies we express the integral in Equation 6.2 as a sum over discrete galaxies. The aperture mass then becomes the weighted sum over the tangential ellipticities:

$$M_{\text{ap}}(\vec{\theta}_0) = \frac{1}{N_{\text{gal}}} \sum_i^{N_{\text{gal}}} Q(\vec{\theta}_i - \vec{\theta}_0) \epsilon_t(\vec{\theta}_i, \vec{\theta}_0), \quad (6.3)$$

where N_{gal} is the total number of observed galaxies inside the aperture, and ϵ_+ is the observed tangential ellipticity and expressed as:

$$\epsilon_+(\vec{\theta}, \vec{\theta}_0) = -[\epsilon_1(\vec{\theta}) \cos(2\phi(\vec{\theta}, \vec{\theta}_0)) + \epsilon_2(\vec{\theta}) \sin(2\phi(\vec{\theta}, \vec{\theta}_0))]. \quad (6.4)$$

The filter functions are optimised for different applications (see for example Maturi et al. 2010). In this work we use a filter function that is optimised to detect NFW haloes taken from Schirmer et al. (2007):

$$Q_{\text{NFW}}(x) = \frac{1}{1 + e^{6-150x} + e^{-47+50x}} \frac{\tanh(x/x_c)}{x/x_c}, \quad (6.5)$$

where $x = \theta/\theta_{\text{ap}}$ is the angular distance from the aperture centre θ_0 scaled by the filter size θ_{ap} . x_c is analogous to the halo concentration in the NFW profile, and it was empirically set to $x_c = 0.15$ in Hettterscheidt et al. (2005). This is consistent with Martinet et al. (2018). Figure 6.1 is a plot of the filter function, $Q_{\text{NFW}}(x)$ (Equation 6.5), used in this work. Note that the filter function downweights galaxies towards the centre of the aperture, which excludes contamination by the presence of a bright central galaxy in a cluster and the strong lensing regime. The filter function is truncated at $\theta = \theta_{\text{ap}}$ and the aperture mass is calculated within the filter size, θ_{ap} .

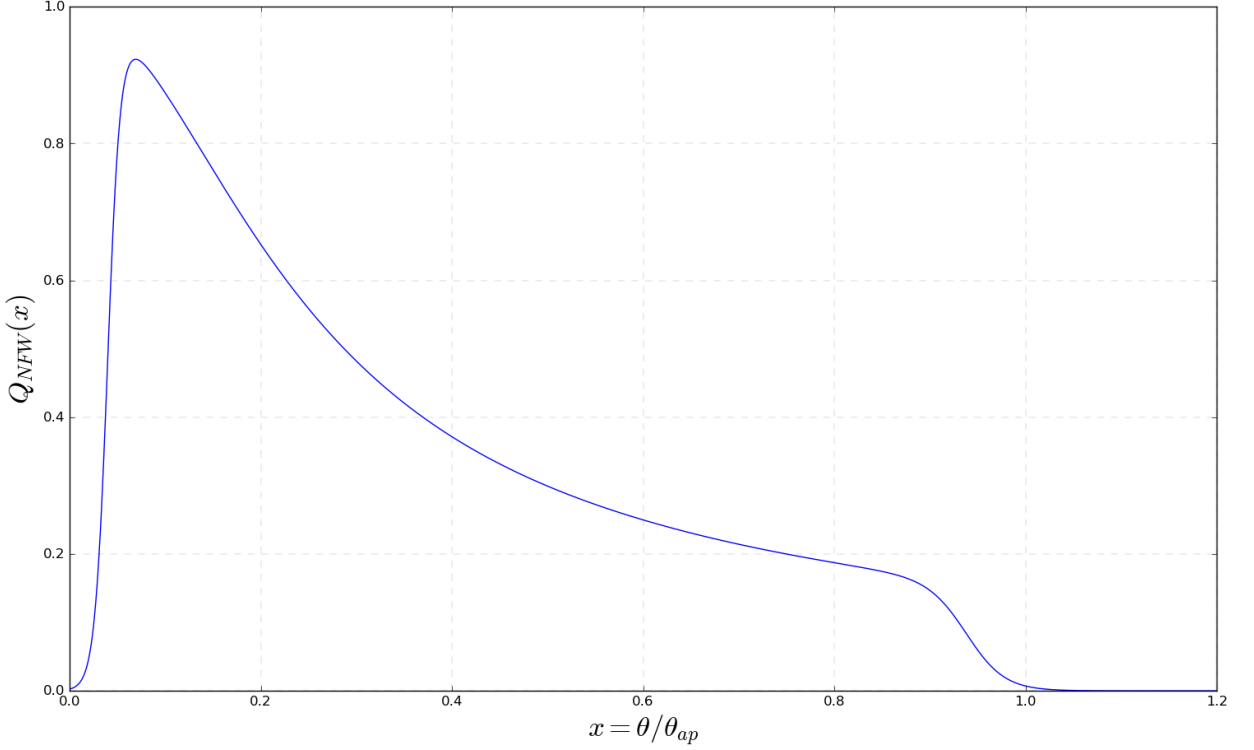


Figure 6.1: $Q_{\text{NFW}}(x)$ is the aperture mass filter function used in this work (Equation 6.5), taken from Schirmer et al. (2007). The aperture mass calculated in Equation 6.3 cuts off at the filter size, $\theta = \theta_{\text{ap}}$ and the falloff towards the centre down-weights the bright central galaxy and the strong lensing regime.

6.2 S/N Peaks

To calculate the S/N ratio for the aperture mass statistic we proceed as in Martinet et al. (2018), where the standard deviation of the aperture mass in the absence of shear is given by:

$$\sigma(M_{\text{ap}}(\vec{\theta}_0)) = \frac{1}{\sqrt{2}N_{\text{gal}}} \left(\sum_i^{N_{\text{gal}}} |\epsilon(\vec{\theta}_i)|^2 Q^2(\vec{\theta}_i - \vec{\theta}_0) \right)^{\frac{1}{2}}. \quad (6.6)$$

The S/N ratio for an aperture measurement is:

$$\frac{S}{N}(\vec{\theta}_0) = \frac{\sqrt{2} \sum_i^{N_{\text{gal}}} Q(\vec{\theta}_i - \vec{\theta}_0) \epsilon_t(\vec{\theta}_i, \vec{\theta}_0)}{\sqrt{\sum_i^{N_{\text{gal}}} |\epsilon(\vec{\theta}_i)|^2 Q^2(\vec{\theta}_i - \vec{\theta}_0)}}. \quad (6.7)$$

Here we use publicly available software, developed by [Bard et al. \(2012\)](#), which implements GPU computing for fast calculation of the aperture mass. The algorithm scans grid points over the synthetic weak lensing data and returns the aperture mass, variance, and S/N values. We ran the code on the synthetic data from Section [4.2](#) using filter sizes $\theta_{\text{ap}} = 8.0, 10.0, 12.5,$ and 15.0 arcmin. For a compromise between the computational efficiency and resolution, the resolution of the aperture maps is set to 512×512 pixels which is 0.5859 arcmin per pixel, similar to [Martinet et al. \(2018\)](#). Figure [6.2](#) shows a sample of the direct overlay of the S/N contour lines (lower limit of S/N at 0 and contour lines increase by increment of 1) on top of the original convergence map (grey scale) of the simulation. The triangles are the S/N peak locations ($S/N > 2$) obtained by a peak detection Python script which examines if each pixel of the S/N map has a higher value than the 8 nearest neighboring pixels. The cross marks are the locations of galaxy clusters taken directly from the BAHAMAS Friends-of-Friends (FoF) catalogues.

In this work we study the impact of the different baryonic prescriptions and summed neutrino masses, the relationship between higher S/N peaks, and the presence of massive clusters.

We use the natural log of the ratio-of-means (RoM) to quantify the difference in the peak counts and to properly propagate errors for relative comparisons. This method was introduced in [Friedrich et al. \(2008\)](#) to compare characteristics such as bias and statistical power using simulated data sets. For our purpose, we calibrate the mean of the peak counts of 5 different noise realisations per each simulation in order to avoid potential bias to one particular noise realisation. Then the natural log of the RoM, $\ln(\mu_x/\mu_0)$, of each bin is calibrated with the variance:

$$\begin{aligned} \text{Var} \left[\ln \left(\frac{\mu_x}{\mu_0} \right) \right] &= \text{Var} [\ln(\mu_x) - \ln(\mu_0)] \\ &= \frac{1}{n_x} \left(\frac{\sigma_x}{\mu_x} \right)^2 + \frac{1}{n_0} \left(\frac{\sigma_0}{\mu_0} \right)^2, \end{aligned} \tag{6.8}$$

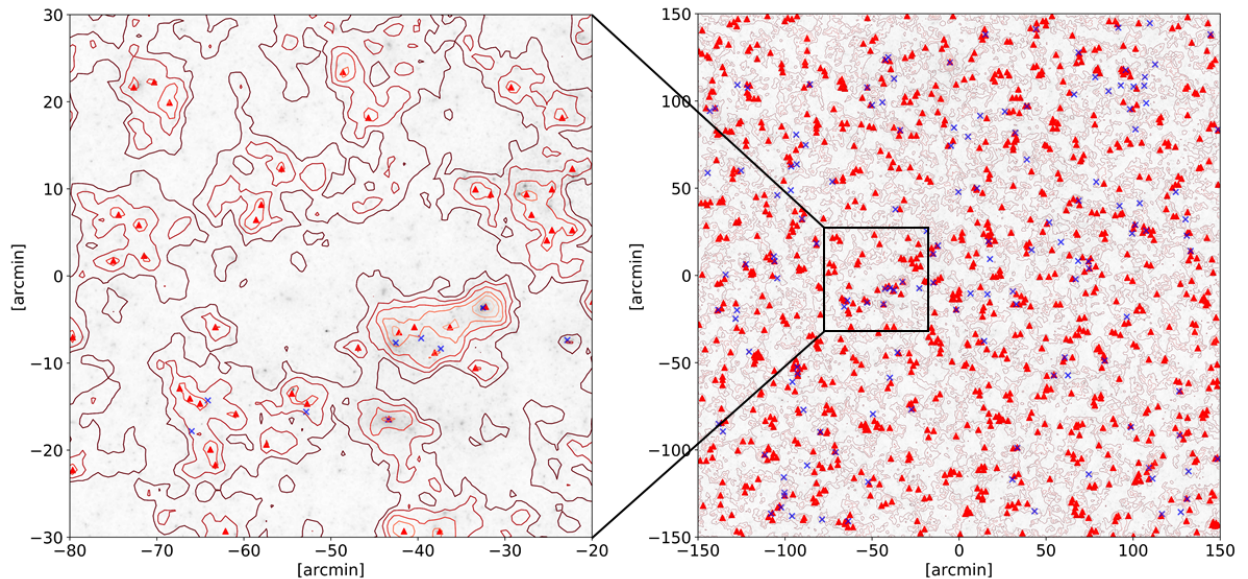


Figure 6.2: A 60×60 arcmin² sub-region of a 5×5 deg² aperture mass map for source number density 9 gal/arcmin². The aperture size is 12.5 arcmin, and the S/N contour lines are plotted from 0 with an increment of 1. The field in grey scale in the background is the original BAHAMAS convergence map, and the cross marks are the locations of clusters from the BAHAMAS friends-of-friends catalogues, where the lowest mass cut is $10^{14}M_{\odot}$ and the upper limit redshift cut is at $z=0.5$. The triangles are the peak locations above $S/N=2$.

where μ_x is the mean of the peak counts of the different realisations for each of the simulation suites with varying AGN feedback and summed neutrino mass, and μ_0 is the mean of the peak counts from the standard simulation suite that will be used for comparison. Similarly σ_x and σ_0 are the standard deviations of the corresponding distributions. Note as an approximation, when interpreting plots of the $\ln(RoM)$ and $\ln(RoM) \ll 1$, $RoM \approx 1 + \ln(RoM)$.

Note that [Martinet et al. \(2018\)](#) used dark matter only simulations to investigate the impact of a much wider range of cosmologies (particularly Ω_m and σ_8) on peak counts for comparison with KiDS data. In this work, as noted in the introduction, we focus on investigating the impact of baryonic processes (including star formation, AGN feedback and supernova feedback) and massive neutrinos on the peak statistics.

6.3 Dependence of Weak Lensing Peak Counts on Baryonic Physics and Summed Neutrino Mass

In our work with Miyoung Choi we consider synthetic surveys with different source redshift distributions and effective number density of sources from which lensing shear can be measured, KiDS, DGB, and DSB as outlined in Section 4.2. The plots shown in this section have the filter size fixed at 12.5 arcmin, for consistency with Martinet et al. (2018), and use the 625 deg² field-of-view for the DGB source redshift distribution simulations ($n_{eff} = 30$ gal/arcmin²) in WMAP9 cosmology.

Figure 6.3 shows the S/N peak distributions for different baryonic physics prescriptions in the top panel. The bottom panel shows the $\ln(RoM)$ compared to the DMONLY peak count. All of these models do not include massive neutrinos. The low S/N peak counts tend to be boosted by up to about 6 percent in comparison with DMONLY. For KiDS (9 gal/arcmin²) we found that the low S/N peaks show a modest boost from baryons resulting in only a few percent deviation from DMONLY. According to the discussion in Martinet et al. (2018), much of the constraining power of peak counts for cosmological models comes from the lower S/N range. Our results indicate that when baryonic processes are accounted for in the error budget, care should be taken to calibrate the impact of baryons as a function of the source number density.

In DMONLY simulations higher S/N peak values are more likely to be produced by more massive clusters, although there is an additional complication due to the dependence of peak height on cluster redshift for a given source population (e.g., Figure 17 of Hamana et al., 2004). The impact of baryons is more significant at higher S/N, where higher peak values are more likely to arise from massive haloes (Hennawi and Spergel, 2005). The massive haloes are more likely to have greater AGN feedback strength that cause the mass density profiles to be flatter and less concentrated (Mummery et al., 2017), thereby returning lower S/N values than the DMONLY case and having a larger effect on the high S/N peaks. This

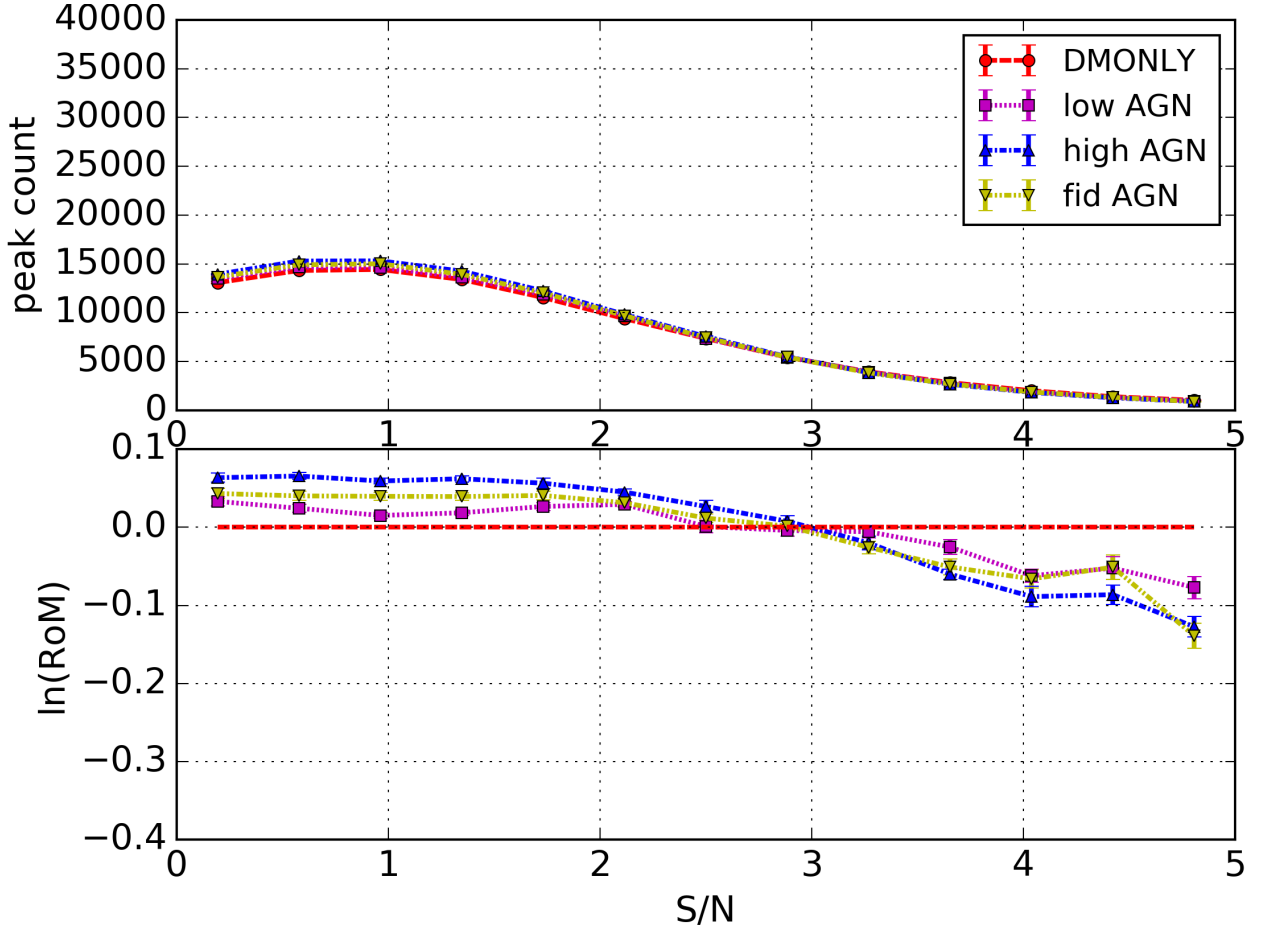


Figure 6.3: The S/N peak counts for the different baryonic physics prescriptions and the DMONLY case, all without massive neutrinos. The bottom panel shows the $\ln(RoM)$ compared to the DMONLY peak count.

also tends to push matter out from the centre of massive haloes and into the environment, contributing to the lower S/N distribution. In Table 3.1 the S_8 values do not vary with AGN temperature, yet these plots show that increasing AGN temperature changes the peak distribution similar to decreasing S_8 (see Martinet et al., 2018). In agreement with previous work (e.g., Osato et al., 2015), this implies that estimating cosmological parameters when using cosmological simulations without baryonic processes can lead to a bias. This is also true for the summed neutrino mass, as discussed below. Additionally, the deviation among the higher S/N peak counts with different AGN feedback strength is hard to resolve, even

though the error bars due to scatter from the different shape noise realisations are tighter than those for the lower number density of sources (as anticipated).

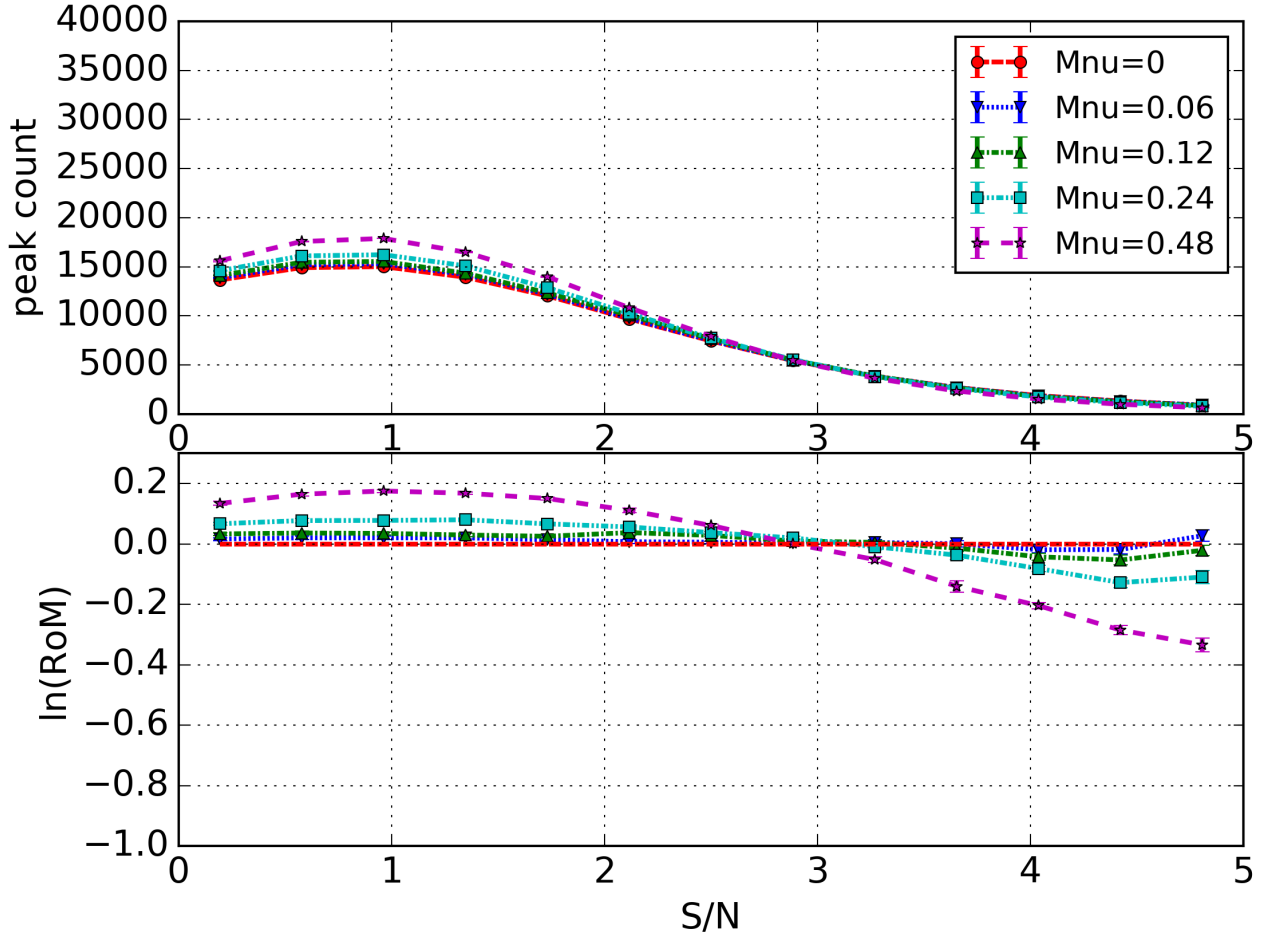


Figure 6.4: The S/N peak counts with varying summed neutrino mass, all with fiducial baryonic physics prescription, for DGB data. The bottom panel shows the $\ln(RoM)$ compared to the zero summed neutrino mass peak count.

The top panel of Figure [6.4](#) shows the S/N peak distributions for different summed neutrino mass, where all models here include the underlying fiducial baryonic physics prescription. The bottom shows the $\ln(RoM)$ compared to the zero summed neutrino mass peak count. These figures show that increasing summed neutrino mass also suppresses (boosts) the high (low) S/N peak counts. This is expected as free-streaming neutrinos impede the growth of LSS and therefore have a larger impact on more massive haloes, suppressing the

high end of the halo mass function more significantly with increasing neutrino mass (e.g., Costanzi et al., 2013; Mummery et al., 2017). Free-streaming neutrinos also spreads matter more uniformly in the Universe, which contributes to the low S/N peak counts. Furthermore, in Table 3.1 increasing summed neutrino mass corresponds to decreasing $S_8 = \sigma_8 \sqrt{\Omega_m/0.3}$. Reducing Ω_m or σ_8 decreases the matter content of the Universe or clustering of structure, producing less massive haloes and high S/N peaks. When this happens it also adds more to the random Gaussian noise in the distribution (see discussion in Martinet et al., 2018 for more details), boosting the low S/N peaks counts.

Note the similarity of the suppression (boosting) in high (low) S/N peak counts due to AGN feedback and massive neutrinos. This can make differentiating baryonic physics and massive neutrinos based purely on S/N peak counts quite difficult. One avenue that can potentially be used to help break this degeneracy, using peak counts alone, is the dependence of the peak counts on redshift, which could be measured using tomographic information (e.g., Hildebrandt et al., 2017). Furthermore Mummery et al. (2017) shows that the halo mass function is effected by baryonic physics prescription and summed neutrino mass differently for different redshifts. This is beyond the scope of this chapter and will be included in future work.

The impact of *WMAP* 9 and *Planck* 2015 cosmologies for $M_\nu = 0.06, 0.12, 0.24,$ and 0.48 eV summed neutrino mass models (all with fiducial baryonic physics) are compared with *WMAP* 9 $M_\nu = 0.00$ eV, as a reference model, in Figures 6.5a and 6.5b, for 9 and 30 gal/arcmin² respectively. Note that we exclude the *WMAP* 9 $M_\nu = 0.48$ eV model as it is well outside of the range of the *Planck* 2015 models (see Figure 6.4). The S/N peak counts with the *WMAP* 9 cosmology show that there is a negative (positive) difference for the higher (lower) S/N peaks for all of the M_ν models (with the exception of the last S/N peak bin in the 0.06 eV model, where the statistics in this bin are poor). Furthermore increasing M_ν suppresses (boosts) the higher (lower) S/N peaks. The peak counts with the *Planck* 2015

cosmology show that there is a positive (negative) difference for the higher (lower) S/N peaks for the M_ν 0.06 to 0.24 eV models. Furthermore the *Planck* 2015 $M_\nu = 0.24$ and 0.48 eV models clearly bracket the *WMAP* 9 $M_\nu = 0.00, 0.06,$ and 0.12 eV models for both KiDS and DGB. This suggests degeneracy between summed neutrino mass and other cosmological parameters in the framework of fiducial baryonic physics. The S/N peak counts are roughly ordered with respect to the S_8 values (see Table 3.1), in agreement with Martinet et al. (2018).

For DGB the weak lensing peak counts with $M_\nu = 0.12$ eV for *WMAP* 9 and *Planck* 2015 have an absolute maximum relative difference of ~ 5 and ~ 11 percent respectively (up to S/N of 5) compared with the *WMAP* 9 zero neutrino mass model. As can be seen from Figure 6.5b, the differences between the peak counts for suites with summed neutrino masses 0.06 and 0.12 eV inside the *WMAP* 9 and *Planck* 2015 cosmologies are smaller than the differences between the counts across the cosmologies. However for higher summed neutrino mass, models across cosmologies but with similar S_8 values have peak counts that are difficult to distinguish. For example the *WMAP* 9 $M_\nu = 0.00$ (0.24) eV model has similar peak counts to the *Planck* 2015 $M_\nu = 0.24$ (0.48) eV model.

Figure 6.6 (corresponding values listed in Table 6.1) compares the peak counts in *WMAP* 9 $M_\nu = 0.0, 0.06, 0.12, 0.24,$ and 0.48 eV models (all with fiducial baryonic physics) to DMONLY, for DGB data. Assuming that baryonic physics and massive neutrinos act independently (Mummery et al., 2017): at lower summed neutrino mass, 0.06 and 0.12 eV, the impact of fiducial baryonic physics on the peak counts tends to be comparable to that of massive neutrinos up to S/N ~ 5 ; at higher summed neutrino mass, 0.24 and 0.48 eV, the presence of massive neutrinos tends to be more important than fiducial baryonic physics. These conclusions are also sensitive to the source number density and intrinsic galaxy ellipticity dispersion.

Table 6.1: The relative percentage differences in S/N peak counts for the DGB survey (these values are taken from Figures 6.4 and 6.6). The values are in units of percent (%) and compare the five different simulations ($M_\nu = 0.0, 0.06, 0.12, 0.24,$ and 0.48 eV, all with fiducial baryonic physics) per S/N bin with the DMONLY simulation.

S/N	M_ν [eV]				
	0.00	0.06	0.12	0.24	0.48
0-1	4.1	6.1	7.7	12.2	21.8
1-2	4.1	5.8	7.3	11.9	22.0
2-3	1.9	2.6	4.6	6.0	9.0
3-4	-3.6	-3.8	-4.1	-5.7	-11.9
4-5	-7.4	-8.2	-11.4	-17.4	-30.0
5-6	-6.3	-13.0	-16.5	-26.3	-42.4
6-7	-12.3	-19.8	-23.5	-33.3	-53.0
7-8	-11.4	-15.6	-21.7	-39.0	-56.0
8-9	-12.7	-21.8	-21.9	-38.9	-63.2
9-10	-16.2	-15.4	-26.8	-42.3	-67.5

6.4 High S/N Weak Lensing Peaks

In this section, we focus on the high S/N peaks for the *Planck* 2015 cosmology with fiducial baryonic physics and varying neutrino mass. We discuss: (1) how summed neutrino mass effects the cluster mass function and also give some examples of the differences in mass for specific clusters. (2) S/N peak dependence on survey characteristics and noise. (3) How filter size impacts on the detection of high S/N peaks. (4) Using cluster positions to find

nearby S/N peaks, within an aperture size, to study the correlation between cluster mass and S/N peaks. This would be analogous to targeting clusters (for example known clusters or clusters selected using another technique) and measuring their aperture mass signal. (5) Using S/N peak locations to find nearby clusters, analogous to carrying out a blind weak lensing survey.

We use the light-cone catalogues from the simulation selecting objects with masses $M_{200c} \geq 10^{14} M_{\odot}$ and $z \leq 0.9$. Clusters are identified by running a friends-of-friends (FoF) algorithm on the full simulation snapshot data. Spherical overdensity masses for the FoF groups are calculated using the SUBFIND algorithm. An overdensity of 200 with respect to the critical density at the snapshot redshift of the FoF group is used (i.e., M200c).

In Figure 6.7 we plot the number counts of clusters for each neutrino mass suite on the top panel. For the bottom panels we take the ratios with respect to the $M_{\nu} = 0.06$ eV distribution. Taken directly from the BAHAMAS light-cones, Figure 6.7 shows that as summed neutrino mass increases, the number count of massive haloes, $N(M_{200c})$, becomes suppressed.¹ These results are consistent with the findings of e.g., Costanzi et al. (2013); Castorina et al. (2014); Mummery et al. (2017); Hagstotz et al. (2018).

The reason for this trend is that neutrinos can free-stream out of overdense regions which inhibits the growth of structure. Increasing the mass in the neutrino component means that a larger fraction of the total mass can free-stream out. The ratio becomes noisy at high masses, due to their rarity. With a larger survey area and sample of high-mass clusters we expect this feature to be smoothed out. We also studied the impact of summed neutrino mass on cluster shapes by analysing their moment of inertia tensors, finding that their axis ratios have no significant change but the overall sizes are altered. This will be a subject of a future project.

¹Note that the light-cone catalogue masses only depend on the simulation, so the distributions are unchanged for varying filter sizes and noise realisations.

Figure 6.8 shows the same field-of-view for four different simulations, where they only differ by neutrino mass. The four panels are M_ν [eV] = 0.06, 0.12, 0.24, and 0.48 for the top left, top right, bottom left, and bottom right panels respectively. The grey scale is the convergence map and \times s are the cluster locations. The smaller the \times the higher the cluster’s redshift. The values next to the \times s are the cluster masses in units of $10^{14}M_\odot$. This shows that with increasing summed neutrino mass most cluster masses decrease (See Figure 6.7), though not all. Note that we only show cluster masses $M_{200c} \geq 10^{14} M_\odot$, and some clusters drop below this limit.

6.4.1 Noise Realisations

We study a total of five shape noise realisations of weak lensing on 625 deg^2 , for the *Planck* 2015 cosmology with $M_\nu = 0.06 \text{ eV}$. Each noise realisation has a different set of random seeds for intrinsic galaxy ellipticities (see Section 4.2). The galaxy positions are the same for each run. In this section we consider cluster-mass objects and high peak values ($S/N \geq 3$).

For KiDS (DGB) data with $n_{\text{eff}} = 9$ (30) gal/arcmin² Figure 6.9a (Figure 6.9b) shows the impact of different shape noise realisations on the aperture mass maps and S/N peaks. Each panel shows the same field-of-view ($1 \times 1 \text{ deg}^2$). The grey scale and \times markers are the convergence maps and cluster locations respectively. The line contours and triangles are the aperture mass S/N and S/N peaks (≥ 3) respectively. A smaller triangle or \times corresponds to a lower S/N peak value or a higher cluster redshift, respectively. \times markers and the convergence maps do not change between noise realisations because they are taken directly from the BAHAMAS simulation. Figures 6.9a and 6.9b show that aperture mass S/N maps and therefore peak locations depend heavily on the noise realisation, but are more consistent with a higher effective number density of source galaxies. The match between S/N peaks and cluster locations is in rough agreement with Martinet et al. (2018, Figure 3), where peaks are not always associated with clusters.

6.4.2 Filter Sizes

Even though we use a fiducial filter size of 12.5 arcmin (see [Martinet et al. \(2018\)](#)) throughout most of this chapter, in this subsection we highlight the well-known impact of filter size (e.g., [Hettterscheidt et al., 2005](#); [Schirmer et al., 2007](#); [Martinet et al., 2018](#)). We focus on the 0.06 eV model. In practice for a real observational survey the filter size would be adjusted depending on the noise properties of the survey and the science goals.

Figure [6.10](#) shows how the S/N peak distribution varies with filter size. The lines represent $\theta_{\text{ap}} = 8.0, 10.0, 12.5$ and 15.0 arcmin. The top sub-panels show the S/N peak value distributions and the bottom sub-panels show the logarithmic ratio of means of the distributions relative to $\theta_{\text{ap}} = 12.5$ arcmin. This shows that increasing aperture size suppresses the S/N peak counts for lower S/N values while boosting counts for higher values. The larger filter sizes tend to be more sensitive to larger structures (contributing more to the higher S/N values) and less sensitive to smaller structures (suppressing lower S/N counts). This is consistent with works which have sought to optimise the aperture mass filter functions or have employed other optimal filtering techniques (e.g., [Hennawi and Spergel, 2005](#); [Schirmer et al., 2007](#); [Maturi et al., 2010](#)). [Martinet et al. \(2018\)](#) found that a filter size of 12.5 arcmin maximises the number of peaks above a S/N of 3 for the KiDS data. However our synthetic catalogues are not constructed in exactly the same manner. For example we have a different intrinsic shape noise and the optimal filter size can also change as a function of number density (see Figures [6.5a](#) and Figure [6.5b](#)).

6.4.3 Summed Neutrino Mass and S/N vs. Cluster Mass

In Section [6.3](#) we discuss how summed neutrino mass impacts on the S/N peak distribution, in particular we find that increasing summed neutrino mass suppresses the high S/N peaks. In the beginning of this section (Section [6.4](#)) we discussed how increasing summed neutrino mass tends to decrease the masses of clusters, consistent with the authors mentioned above.

In this subsection we study the relationship between S/N peak values and cluster mass, and the dependence on summed neutrino mass.

First we study the correlation between S/N peaks and cluster locations. Note that given the redshift distribution of KiDS, it is not likely that clusters with redshifts above $z = 0.5$ will be significantly detected with lensing. We also limit the lower bound S/N peak values to 3 for consistency with the regime dominated by clusters rather than large-scale structure in a KiDS-like survey (Martinet et al., 2018).

The clusters and any associated S/N peak locations can then be used to investigate how well S/N peaks trace cluster mass. We do this by taking circular areas of radius θ_{ap} centred on cluster centres to identify nearby S/N peaks. Note that there may not be any S/N peaks within the circles (See Figure 6.9). When there are multiple S/N peaks enclosed, we allow for two options: either choose the closest S/N peak or the highest value enclosed. In this chapter we will show only the results for choosing the closest S/N peaks.² We also allow S/N peaks to be chosen by multiple clusters.³

In the case of assuming known cluster locations and choosing the closest S/N peak, in Figure 6.11 we plot S/N peak values vs. M_{200c} for the four different summed neutrino masses, M_ν [eV] = 0.06, 0.12, 0.24, and 0.48, with the upper and lower panels showing the results for KiDS and DGB respectively. Note that in these panels the clusters are not segregated into redshift bins. This means that the lensing efficiencies are not accounted for when comparing S/N peaks to cluster mass. The Pearson correlation coefficient (PCC) measures the linear relationship between two datasets, where the value can range from -1 to $+1$. $PCC = 0$ means there is no linear correlation and $+1(-1)$ means there is a positive(negative) linear relationship. The PCC values for each sub-panel are (M_ν, PCC) , for KiDS: (0.06 eV, 0.28),

²When choosing the highest S/N peaks *some* points in the plot of S/N against M_{200c} are shifted to higher S/N values, but the distributions for choosing by closest and highest are mostly the same.

³When we allow S/N peaks to be associated with only one cluster, there is a potential bias in fields where there are multiple clusters.

(0.12 eV, 0.30), (0.24 eV, 0.30), (0.48 eV, 0.31); and for DGB: (0.06 eV, 0.46), (0.12 eV, 0.46), (0.24 eV, 0.46), (0.48 eV, 0.49). The plots show that increasing summed neutrino mass tends to decrease cluster masses and S/N peak height (see Figures [6.7](#) and [6.4](#)).

Figure [6.12](#) shows the S/N values vs. M_{200c} segregated into different redshift bins for KiDS and DGB (upper and lower panels respectively). The simulations are for $M_\nu = 0.06$ eV. The lines are the average of the S/N values in logarithmic mass bins and the error bars show the variance of S/N inside the mass bins (note that there is a limit at S/N = 3, which impacts on the error bars in particular for the higher redshifts). The Pearson Correlation Coefficient values are (z_{bin}, PCC) , for KiDS: ([0.1, 0.2], 0.63), ([0.2, 0.3], 0.67), ([0.3, 0.4], 0.43), ([0.4, 0.5], 0.24), ([0.5, 0.6], 0.04), ([0.6, 0.7], -0.05), ([0.7, 0.8], -0.03), ([0.8, 0.9], -0.06); and for DGB: ([0.1, 0.2], 0.67), ([0.2, 0.3], 0.71), ([0.3, 0.4], 0.64), ([0.4, 0.5], 0.56), ([0.5, 0.6], 0.36), ([0.6, 0.7], 0.31), ([0.7, 0.8], 0.15), ([0.8, 0.9], 0.04). For both KiDS and DGB the PCC values decrease with increasing redshift. This figure and corresponding PCC values show that there is not only a greater correlation between S/N peaks and M_{200c} for the lower redshift bins, but that increasing the number density of background sources also has a significant impact on the correlation. The redshifts of the clusters enter into the lensing geometry, while increasing the number density of background sources tends to increase the aperture mass signal. In the highest redshift bins there are fewer sources that are background to the clusters, again decreasing the lensing signal. The differences in cosmology between the different summed neutrino mass models also have a slight impact on cosmological distance measures, which enter into Equation [4.3](#).

6.4.4 Summary of Weak Lensing Peak Statistics for Varying Survey Characteristics

In this sub-section, as well as KiDS and DGB, we also consider a deeper survey (DSB, $n_{\text{eff}} = 60$ gal/arcmin²) to show how lensing source number densities effect the correspondence

between high S/N peaks and clusters. For particular survey characteristics, ray-tracing through simulations with a reasonable prescription for baryonic physics and summed neutrino mass can be used to calibrate the correspondence between S/N peaks and clusters or other features in the LSS.

Figure 6.13 is the S/N peak distribution for KiDS, DGB, and DSB (dashed, solid, and dash-dotted curves respectively). As n_{eff} increases, the number of S/N peaks is significantly increased for $S/N \geq 3$. Furthermore, the increase in number density of background sources can produce extremely high S/N peak values. Note that we use a filter function that down-weights the strong lensing regime when centred on a cluster (Equation 6.5 and Figure 6.1). In practice we would apply corrections for factors such as intrinsic alignment of galaxies, and the boost factor in dense regions, as in for example Kacprzak et al. (2016); Martinet et al. (2018). However, intrinsic alignment is thought to have negligible impact on S/N peaks (see discussion in Shan et al., 2018) and BAHAMAS doesn't have the resolution to measure and establish the intrinsic alignments of galaxies directly.

In Figure 6.14 we determine the fraction of cluster-mass objects in our catalogue that enclose a S/N peak (≥ 3) within radius θ_{ap} , or $N_{S/N}/N_{\text{total}}$. KiDS, DGB, and DSB are represented by the dashed, solid, and dash-dotted curves, respectively. For DSB, the fraction is almost 1 for the entire cluster mass range considered here, so the vast majority of clusters are detected at high significance by weak lensing.

Figure 6.15 shows the fraction of S/N peaks (≥ 3) that enclose a cluster-mass object within radius $\theta_{\text{ap}} = 12.5$ arcmin. The dashed, solid, and dash-dotted curves are for KiDS, DGB, and DSB source number densities respectively. Note that this plot differs from Figure 6.14 because there is a different number of S/N peaks than cluster-mass haloes, and we are using those as the centres of our circles when searching for nearby masses, for example see Figure 6.9. Identifying clusters around S/N peaks is similar to using a blind weak lensing survey to search for massive objects (e.g., Hettterscheidt et al., 2005).

High S/N peaks arise from clusters but also from features in the LSS. For a given cluster, increasing the source number density increases the S/N with which the cluster is detected (see Figure [6.12](#)) and can also increase the number of peaks associated with a particular cluster (see Figure [6.9](#)). Caution should be used when interpreting this figure. For example, at a $S/N \approx 5$, 95% of S/N peaks are associated with clusters for KiDS, however there are far fewer S/N peaks on the KiDS maps (see Figure [6.13](#)) and hence many clusters go undetected (see Figure [6.14](#)).

6.5 S/N Peak Conclusions

In this chapter we have quantified the impact of baryonic physics and massive neutrinos on weak lensing peak statistics. We have considered a range of prescriptions for the baryonic physics (with zero neutrino mass) and summed neutrino mass ($M_\nu = 0.06, 0.12, 0.24, 0.48$ eV, for the fiducial baryonic physics model) implemented in the BAHAMAS simulations ([McCarthy et al., 2018](#)). Our results for baryonic physics and massive neutrinos can guide the error budget when deriving cosmological parameters from WL peak statistics. Different assumptions are made for the redshift distributions of the galaxy source populations in the synthetic surveys, and the number densities of sources on the sky from which weak lensing shear can be measured (9, 30 and 60 gal/arcmin²). We have also considered the correspondence between high S/N peaks and galaxy clusters for a fiducial baryonic physics prescription while varying summed neutrino mass.

The WL peak statistics were determined from synthetic aperture mass S/N maps calculated from shape noise realisations of simulated WL data fields. Calculation of the convergence assumed different source redshift distributions, and we use source number densities roughly corresponding to the KiDS data and the expectation for LSST and Euclid. We also considered a higher source number density corresponding to space-based observations, such as *HST*. Aperture mass S/N maps were determined using the aperture mass filter function

optimized to the NFW profile (Schirmer et al., 2007) with the publicly available code from Bard et al. (2012). We use a filter size of 12.5 arcmin for consistency with Martinet et al. (2015).

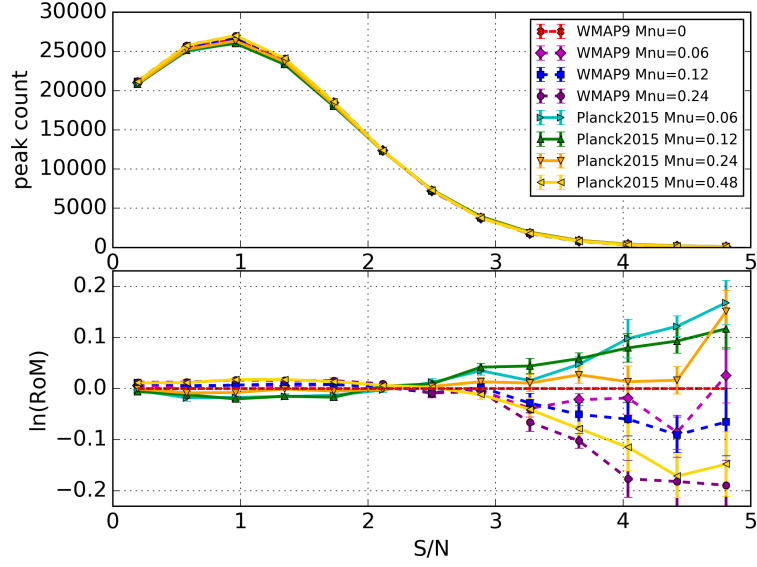
In summary we find that:

- Considering the *WMAP* 9 cosmology, the impact of baryonic physics (in addition to the gravity of DM) boosts (suppresses) the peak counts for low (high) S/N. The low S/N peaks are consistently boosted by less than a few percent with the KiDS survey, whereas for deeper DGB data the low S/N peaks are boosted by about 2-6 percent relative to DMONLY case. With DGB number density, the lower S/N peak statistics are more sensitive to baryonic physics. The high S/N peaks become more suppressed with increasing S/N value. We explain this suppression using the fact that AGN feedback changes the shape of the mass density profiles of massive clusters. Baryonic physics is roughly degenerate with the impact of S_8 seen in Martinet et al. (2018) as well as with massive neutrinos.
- Free-streaming neutrinos during the early epoch of the Universe hinder formation of LSS and result in changing S_8 and, therefore, impact the WL peak distribution. For the *WMAP* 9 cosmology 0.06 and 0.12 eV summed neutrino mass models, the impact of massive neutrinos (at fixed fiducial baryonic physics) on the peak counts compared with DMONLY (collisionless dynamics) tends to be less significant than that of baryonic physics. For higher 0.24 and 0.48 eV summed neutrino mass models, the impact of massive neutrinos tends to be greater than that of baryonic physics. The lowest source density (9 gal/arcmin²) peak distributions for the 0.06 and 0.12 eV models are not significantly different, but higher summed neutrino mass models become more distinguishable from the DMONLY model, even at this low source number density. For deeper surveys the peak distributions have greater power to differentiate between summed neutrino mass models.

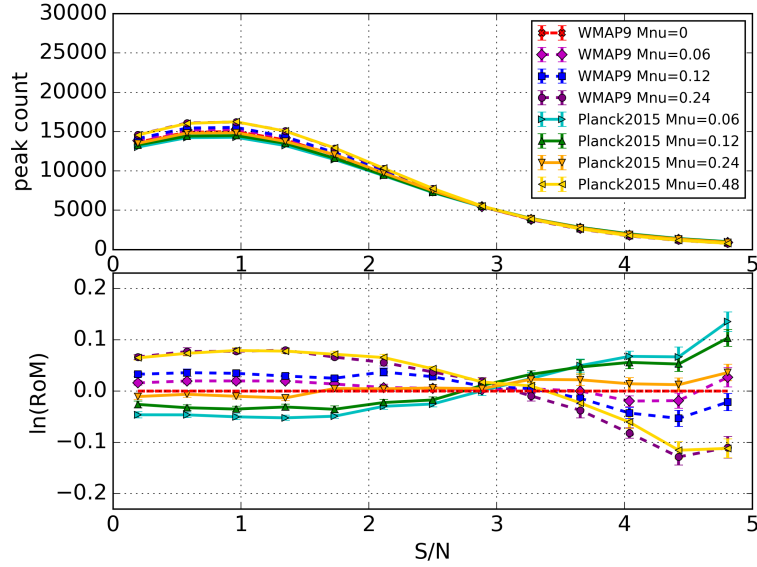
- Different cosmological parameters based on *WMAP* 9 and *Planck* 2015 surveys were compared, using models with summed neutrino mass 0.06, 0.12, 0.24, and 0.48 eV, all with fiducial baryonic physics. The peak distributions show clear differences for the *WMAP* 9 and *Planck* 2015 cosmologies if restricted to the 0.06 and 0.12 eV models; the peak distributions of *Planck* 2015 at low S/N are suppressed consistently by ~ 5 percent for the 30 gal/arcmin² source number density case, and the high S/N peaks are boosted by ~ 5 to ~ 10 percent, compared to the *WMAP* 9 peak distributions. However considering higher summed neutrino mass (0.24 and 0.48 eV), models across cosmologies but with similar S_8 values have peak counts that are difficult to distinguish. For example the *WMAP* 9 $M_\nu = 0.00$ (0.24) eV model has similar peak counts to the *Planck* 2015 $M_\nu = 0.24$ (0.48) eV model.
- Impact of massive neutrinos on high S/N peaks and massive clusters: consistent with Costanzi et al. (2013); Castorina et al. (2014); Mummery et al. (2017); Hagstotz et al. (2018), the cluster mass function is suppressed when including baryonic physics and non-zero neutrino mass. Increasing the summed neutrino mass typically, although not always, reduces the masses and S/N peak heights of individual galaxy clusters. For a fixed prescription of baryonic physics in the *Planck* 2015 cosmology, higher neutrino mass reduces the number of high S/N peaks.
- Efficiency of cluster detection for $M_\nu = 0.06$ eV and fiducial baryonic physics: even for the most massive clusters ($\geq 10^{14}M_\odot$), a weak lensing S/N peak is not always present at the lowest source number density, 9 gal/arcmin². For example, in Figure 6.14, at $M_{200c} \approx 8 \times 10^{14}M_\odot$ there is ≈ 80 percent likelihood that a cluster has a corresponding weak lensing peak (≥ 3). Note that the random distribution of intrinsic background galaxy shapes from which the shear is measured has an impact on the detection of a foreground cluster using aperture mass peaks. At higher source number

density (30 gal/arcmin²) we find that more than 90 percent of clusters have a detected weak lensing peak. For the highest number density 60 gal/arcmin², we find that nearly all clusters have significant weak lensing peaks. These statements on the detection of massive clusters for different source densities hold for the range of summed neutrino masses considered. However, the number of clusters decreases as a function of summed neutrino mass. The ability to study the peak statistics for intermediate redshift galaxy clusters relies on deeper lensing data. This can be seen in the differences between Figures [6.12a](#) and [6.12b](#).

- Figure [6.6](#) and Table [6.1](#) encapsulates the main findings of this chapter. For the *WMAP* 9 cosmology, the percentage difference between the S/N peak counts in comparison with the DMONLY (collisionless dynamics) model is shown for summed neutrino mass 0.00, 0.06, 0.12, 0.24 and 0.48 eV models (all with fiducial baryonic physics). Assuming that baryonic physics and massive neutrinos act independently ([Mummery et al., 2017](#)): for lower (non-zero) summed neutrino mass models 0.06 and 0.12 eV, baryonic physics tends to have a greater impact on the results than massive neutrinos; for higher summed neutrino mass models 0.24 and 0.48 eV, massive neutrinos can change the peak counts by more than fiducial baryonic physics. We have considered a range of models for baryonic physics and summed neutrino mass; the precise impact will depend on the true baryonic physics and summed neutrinos mass, as well as on the characteristics of the survey itself.



(a) 9 gal/arcmin²



(b) 30 gal/arcmin²

Figure 6.5: The impact of different cosmologies (*WMAP* 9 and *Planck* 2015) on the weak lensing peak statistics with aperture filter size fixed at 12.5 arcmin. The number densities shown here are 9 and 30 gal/arcmin², corresponding to KiDS and DGB respectively. The bottom panels show the $\ln(RoM)$ compared to *WMAP* 9 with fiducial AGN feedback and the error bars show the variance of the five different shape noise realisations. The dashed horizontal line shows where the ratio is unity. Note that we exclude the *WMAP* 9 $M_\nu = 0.48$ eV model as it is well outside of the range of the *Planck* 2015 models (see Figure 6.4). All of the models have fiducial baryonic physics.

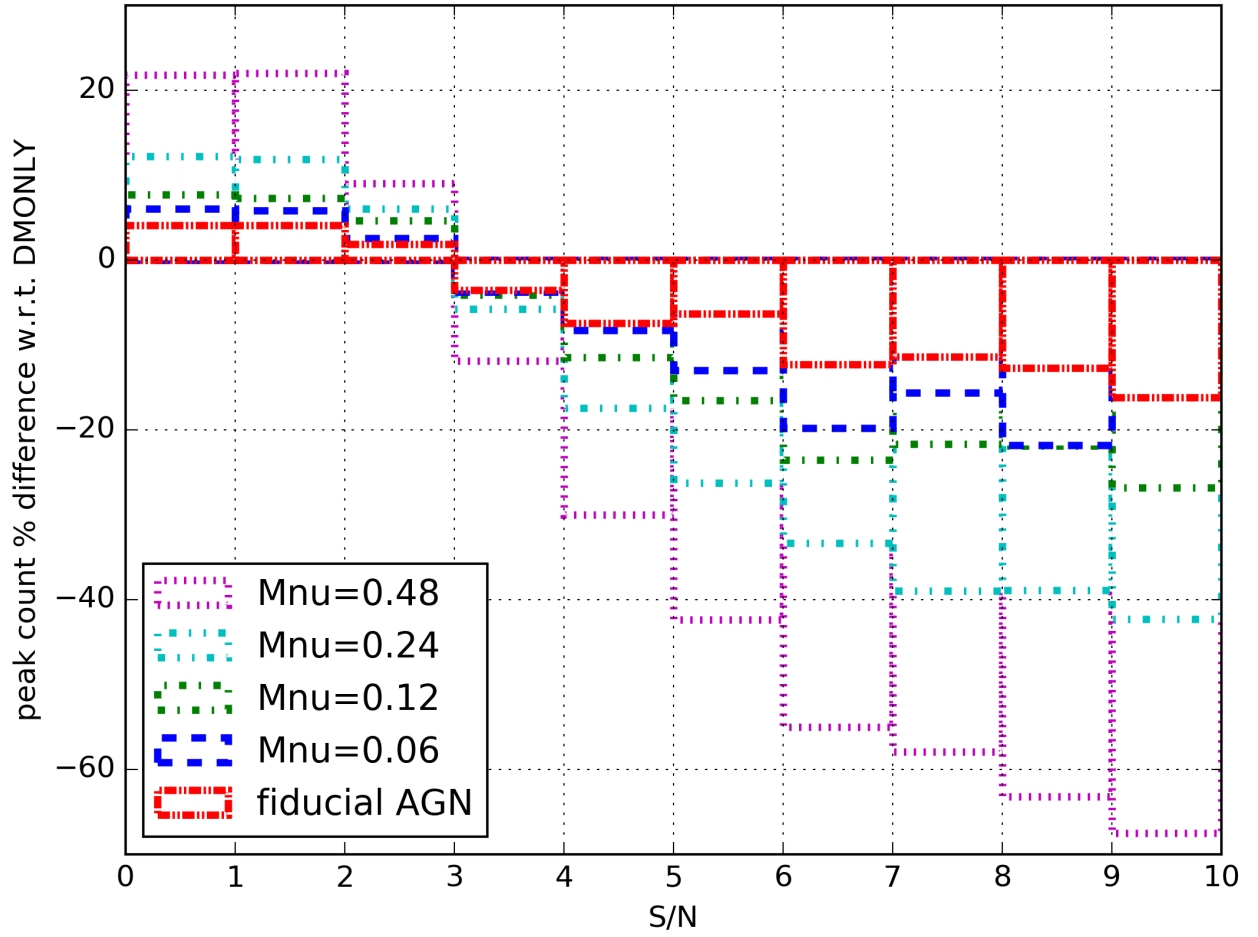


Figure 6.6: Relative percentage differences in peak counts with respect to the DMONLY peak count distribution (Figure 6.4). For the DGB survey, five models ($M_\nu = 0.00, 0.06, 0.12, 0.24,$ and 0.48 eV, all with fiducial baryonic physics) of the *WMAP* 9 cosmology are compared with the DMONLY model in order to determine percentage differences in each interval of S/N.

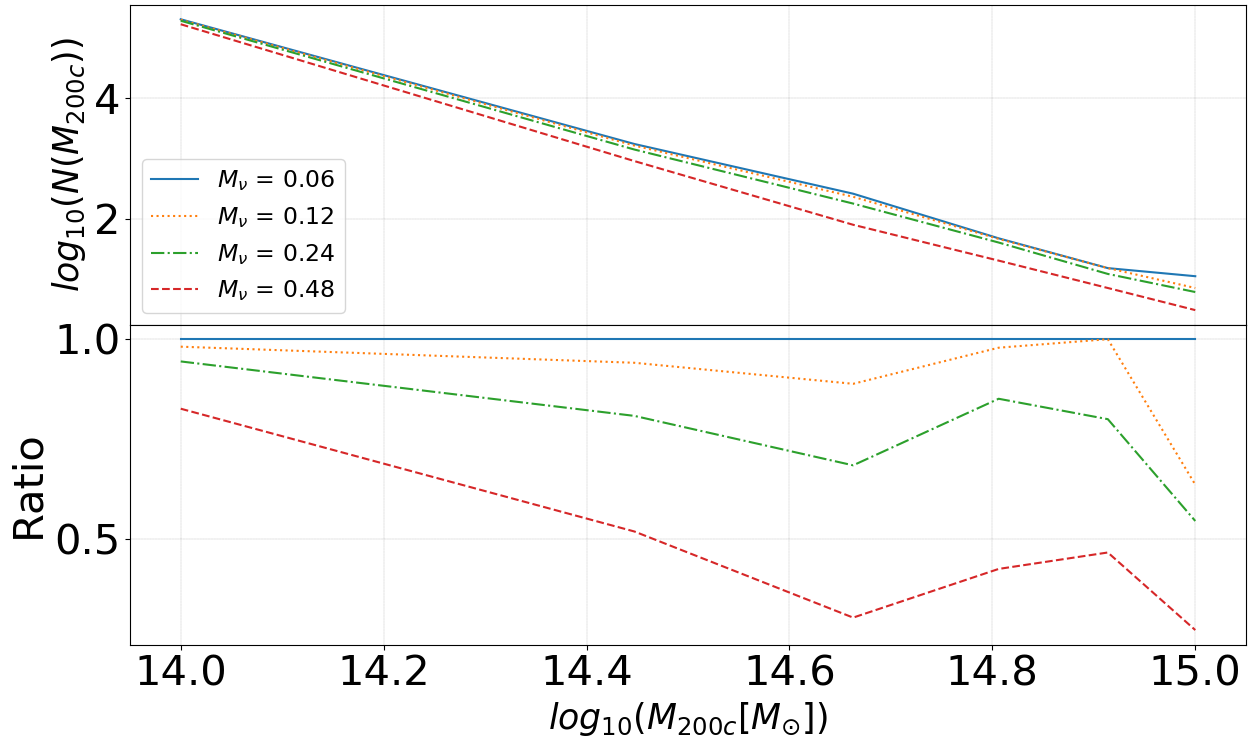


Figure 6.7: The cluster counts as a function of mass for different summed neutrino mass runs. The solid, dotted, dash-dotted, and dashed lines correspond to M_{ν} [eV] = 0.06, 0.12, 0.24, and 0.48. These results are for $\theta_{\text{ap}} = 12.5$ arcmin, and $n_{\text{eff}} = 9$ gal/arcmin². The bottom panel shows the ratio of the number counts between the different massive neutrino simulations in comparison with the 0.06 eV model.

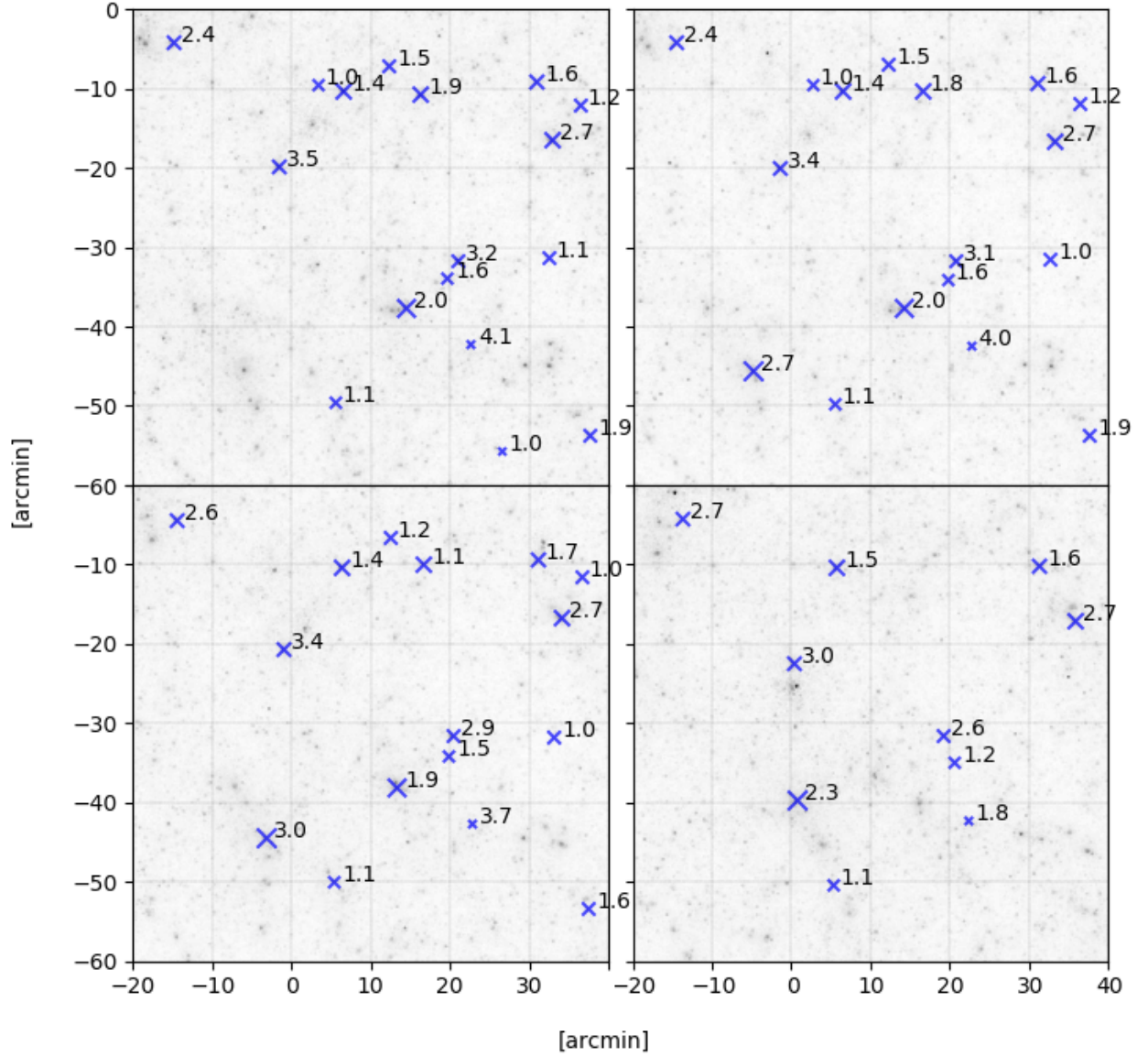
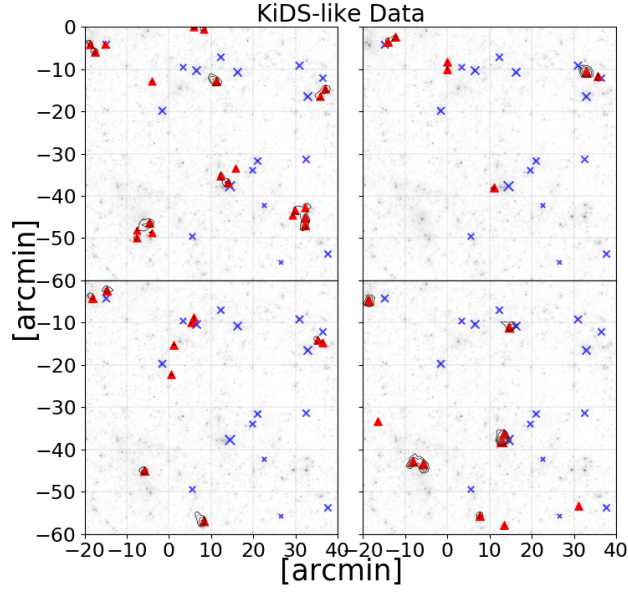
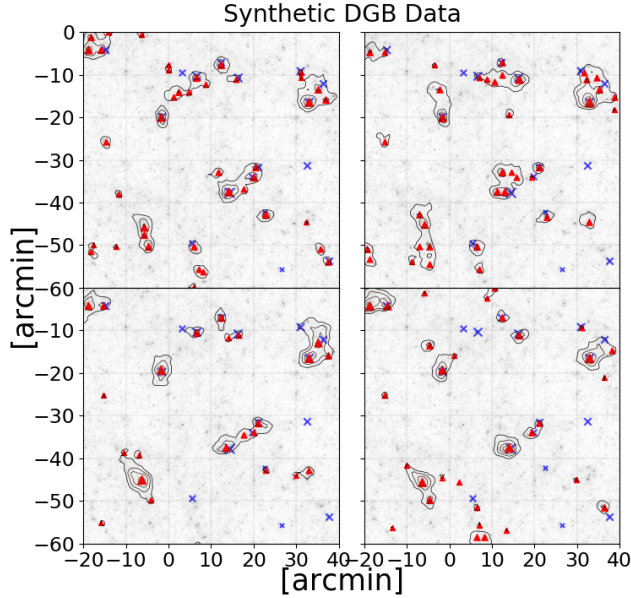


Figure 6.8: The locations of clusters on the convergence maps for different summed neutrino mass. This is the same field-of-view for four different simulations in the *Planck* 2015 cosmology with $n_{\text{eff}} = 9$ gal/arcmin². The four panels have M_ν [eV] = 0.06, 0.12, 0.24, and 0.48 for the top left, top right, bottom left, and bottom right panels respectively. The grey scale is the convergence map and \times s are the cluster locations. The smaller the \times the higher the cluster redshift. The values next to the \times s are the cluster masses in units of $10^{14} M_\odot$.

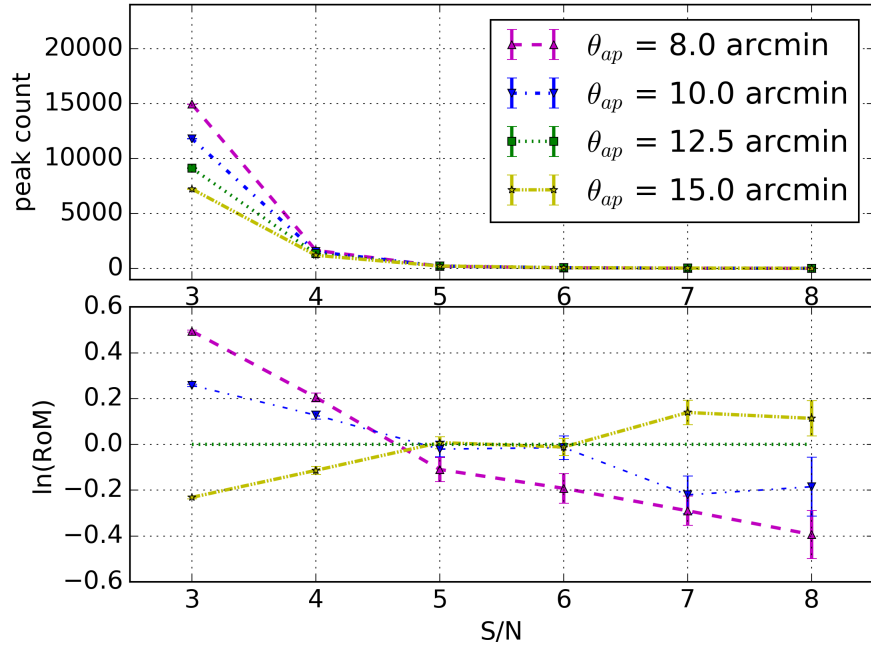


(a) 9 gal/arcmin²

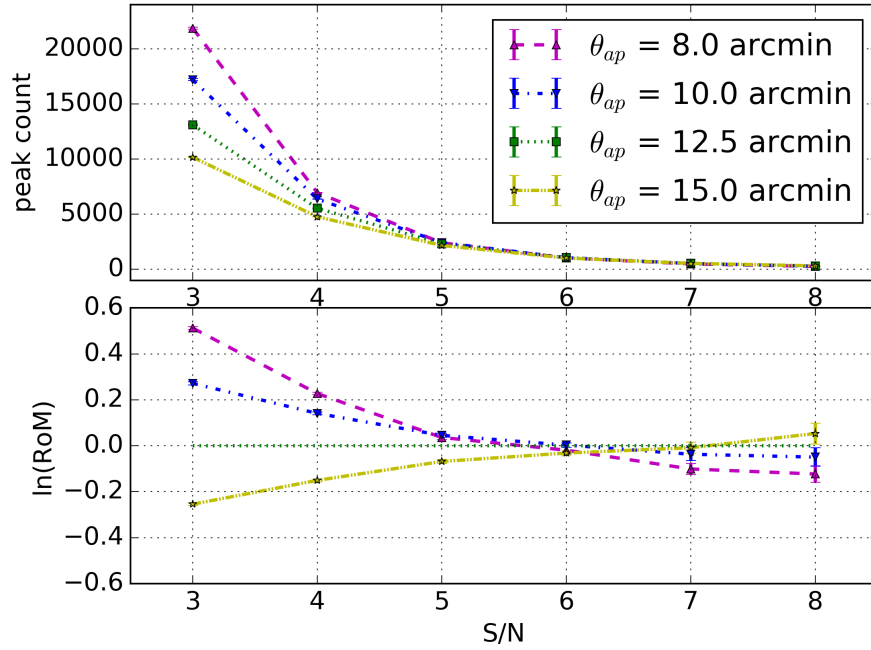


(b) 30 gal/arcmin²

Figure 6.9: The correspondence between the locations of S/N peaks and massive dark matter haloes for four sets of shape noise realisations for KiDS and DGB surveys. The grey scale is the convergence map, the line contours are the S/N of the aperture mass map, triangle markers are the S/N peaks, and \times markers are cluster locations from the halo finder catalogue. A smaller triangle or \times corresponds to a lower S/N peak value or a higher cluster redshift, respectively. All four panels show the same field-of-view ($1 \times 1 \text{ deg}^2$) with the *Planck* 2015 cosmology and $M_\nu = 0.06 \text{ eV}$.



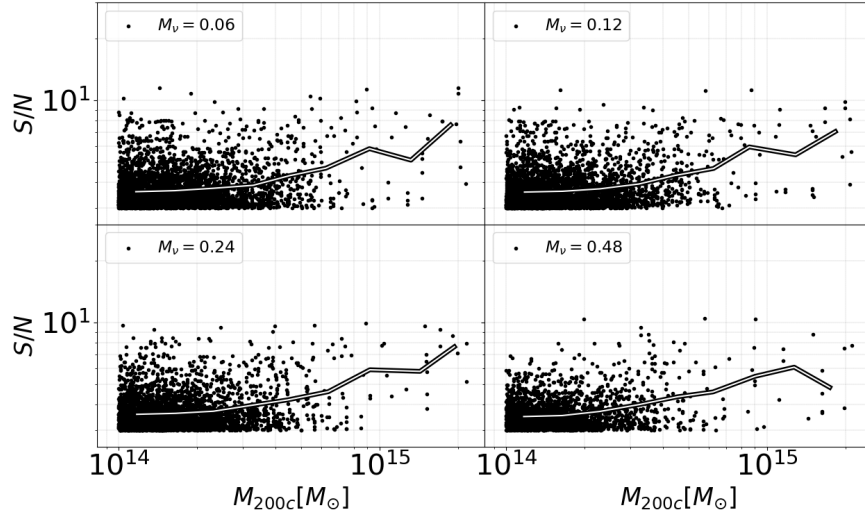
(a) 9 gal/arcmin²



(b) 30 gal/arcmin²

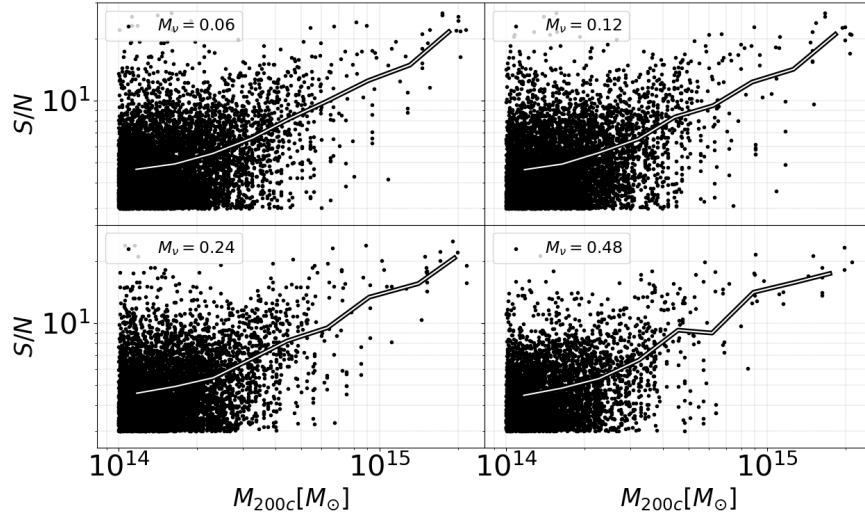
Figure 6.10: The distribution by S/N for various aperture sizes for KiDS and DGB, top and bottom panels respectively. The lines represent $\theta_{ap} = 8.0, 10.0, 12.5,$ and 15.0 arcmin. The top sub-panels show the S/N distribution while the bottom sub-panels show the logarithmic ratio of means for the distributions relative to $\theta_{ap} = 12.5$ arcmin. The error bars show the variance of the five different shape noise realisations.

KiDS-like Data



(a) 9 gal/arcmin²

DGB-like Data



(b) 30 gal/arcmin²

Figure 6.11: The S/N peaks vs. M_{200c} for different summed neutrino mass for KiDS and DGB (left and right panels respectively). The different sub-panels correspond to different summed neutrino mass M_ν [eV] = 0.06, 0.12, 0.24, and 0.48. This shows the S/N peaks closest to the cluster centres. The points are the S/N values plotted against cluster mass, while the line shows the mean S/N in logarithmic mass bins. The Pearson Correlation Coefficient (PCC) is calculated for each sub-panel (see text for details). The PCC values for each sub-panel are (M_ν, PCC) , for KiDS: (0.06 eV, 0.28), (0.12 eV, 0.30), (0.24 eV, 0.30), (0.48 eV, 0.31); and for DGB: (0.06 eV, 0.46), (0.12 eV, 0.46), (0.24 eV, 0.46), (0.48 eV, 0.49).

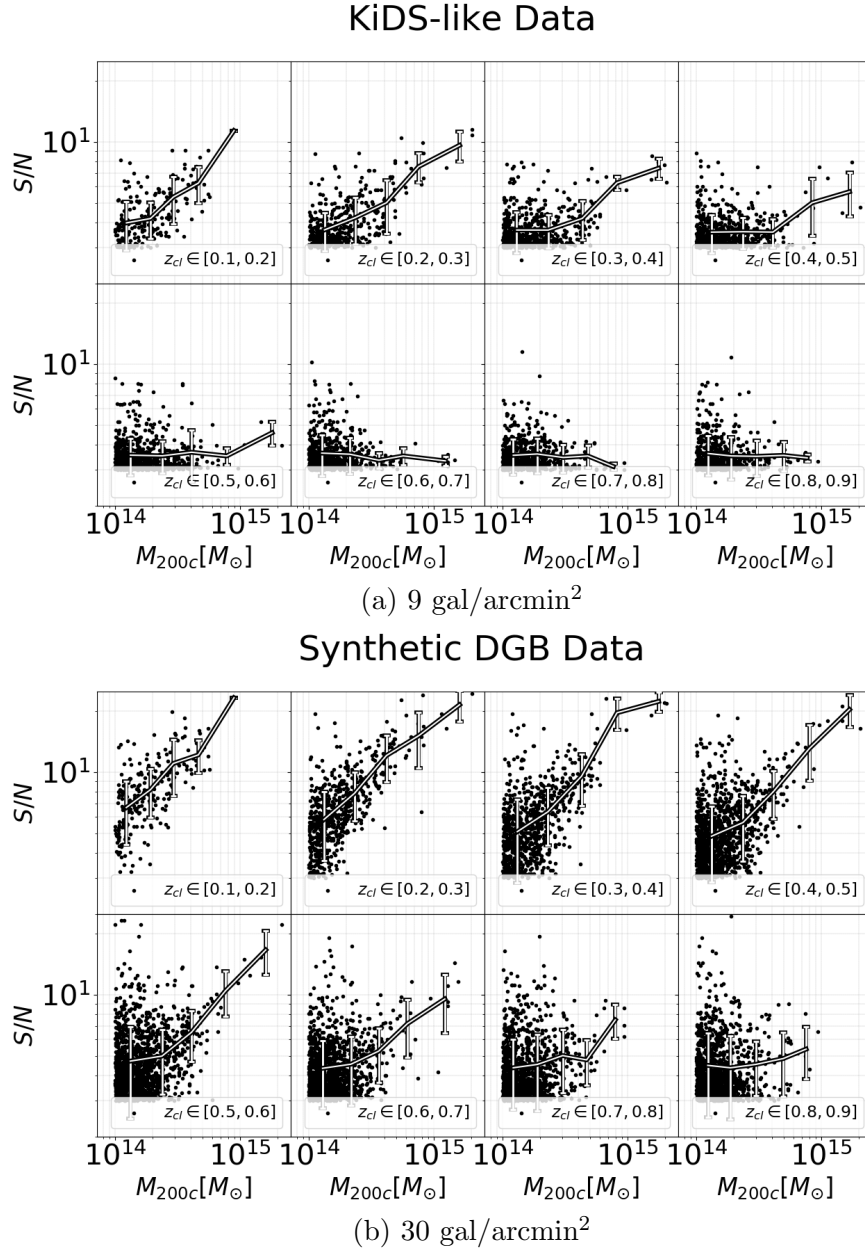


Figure 6.12: The S/N peaks vs. M_{200c} in different redshift bins for KiDS and DGB (upper and lower panels respectively). The points are the S/N peak values (≥ 3) closest to the massive objects; the lines are the average of the S/N values in logarithmic mass bins and the error bars show the variance (note that there is a limit at S/N = 3). This plot is for $M_\nu = 0.06$ eV. The Pearson Correlation Coefficient values are (z_{bin}, PCC) , for KiDS: ([0.1, 0.2], 0.63), ([0.2, 0.3], 0.67), ([0.3, 0.4], 0.43), ([0.4, 0.5], 0.24), ([0.5, 0.6], 0.04), ([0.6, 0.7], -0.05), ([0.7, 0.8], -0.03), ([0.8, 0.9], -0.06); and for DGB: ([0.1, 0.2], 0.67), ([0.2, 0.3], 0.71), ([0.3, 0.4], 0.64), ([0.4, 0.5], 0.56), ([0.5, 0.6], 0.36), ([0.6, 0.7], 0.31), ([0.7, 0.8], 0.15), ([0.8, 0.9], 0.04).

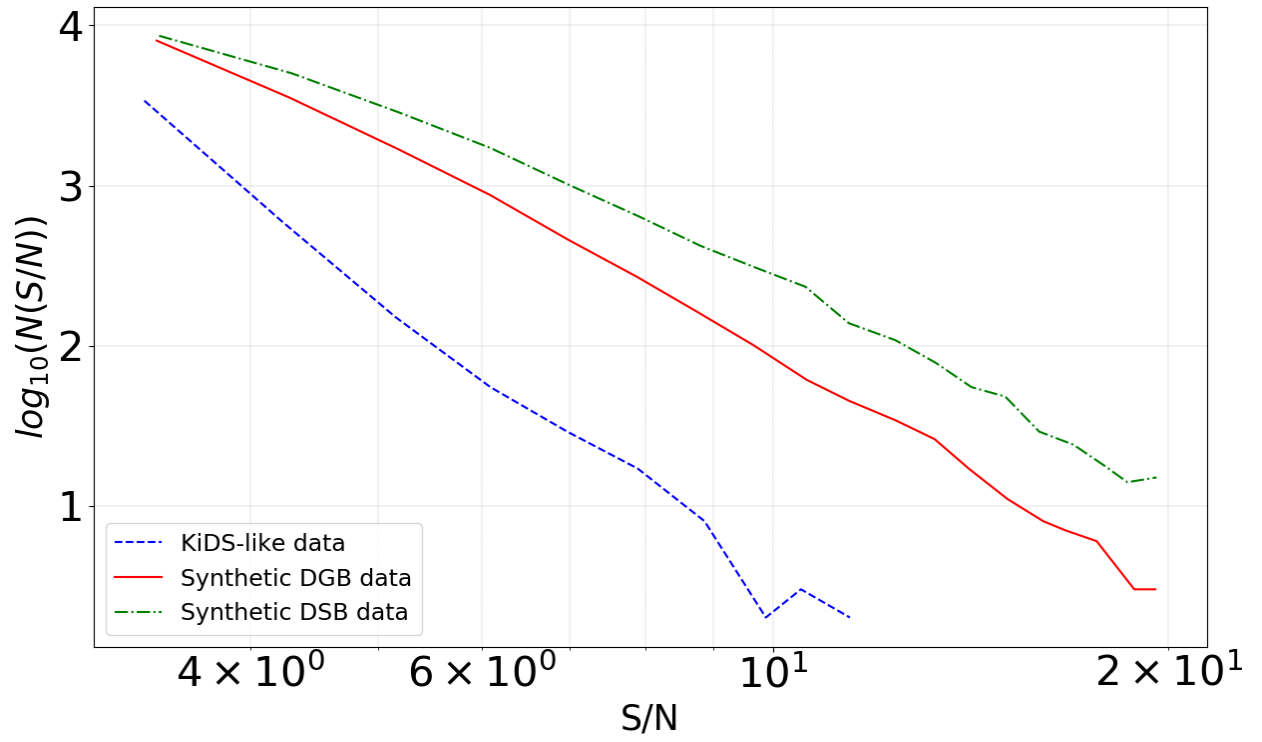


Figure 6.13: The high S/N peak distribution for $n_{\text{eff}} = 9, 30, \text{ and } 60 \text{ gal/arcmin}^2$ (dashed, solid, and dash-dotted curves respectively).

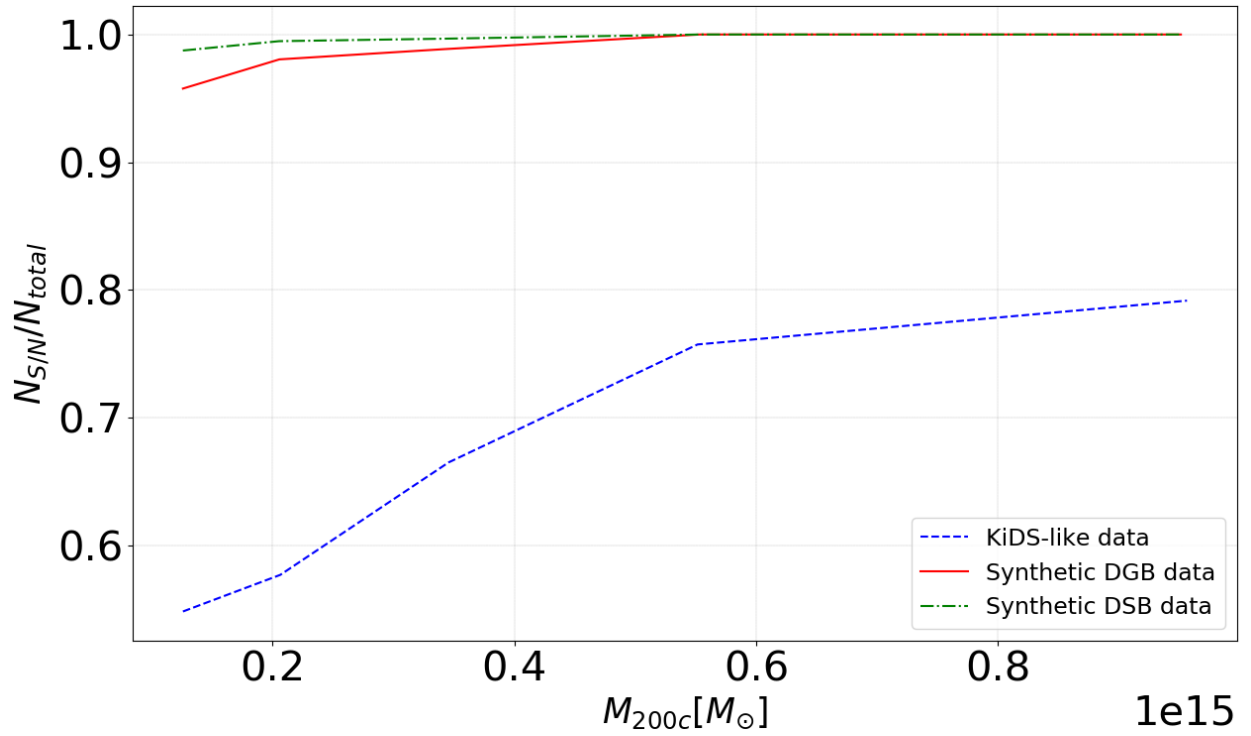


Figure 6.14: The fraction of clusters that have an associated S/N peak as a function of cluster mass. Source number densities $n_{\text{eff}} = 9, 30,$ and 60 gal/arcmin^2 are represented by the dashed, solid, and dash-dotted curves, respectively.

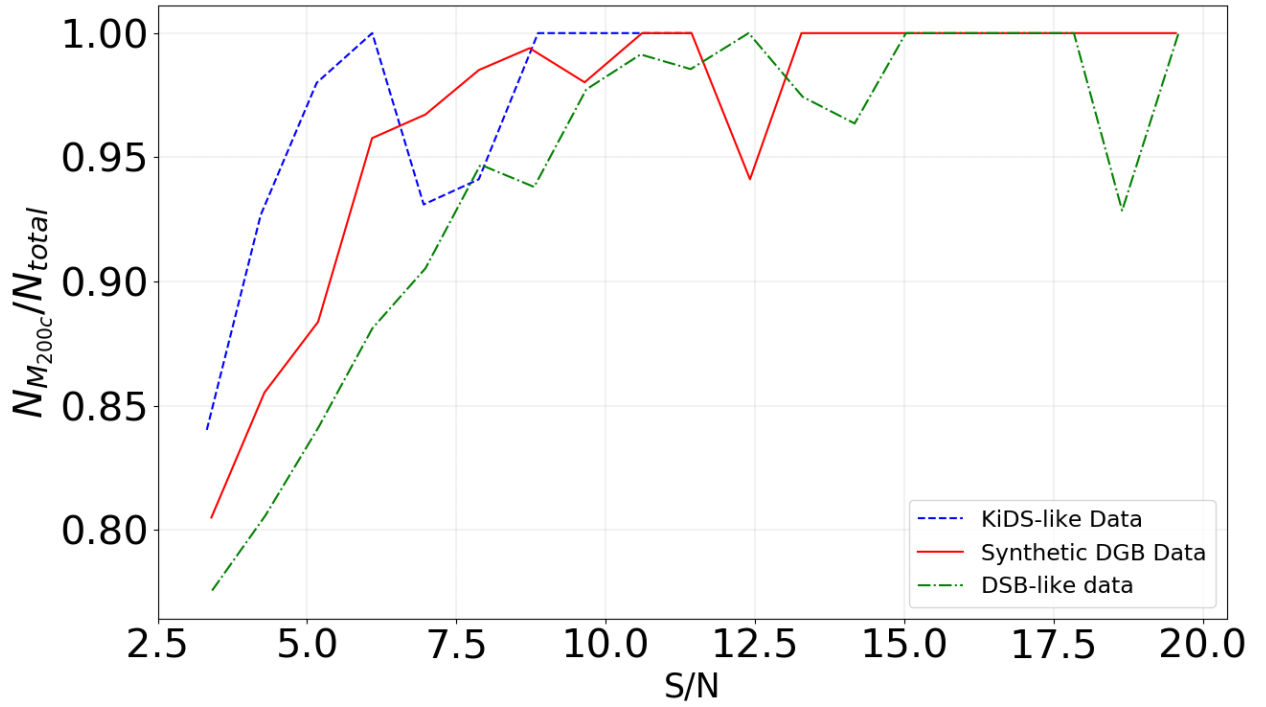


Figure 6.15: The fraction of S/N peaks (≥ 3) that have a nearby cluster within radius $\theta_{ap} = 12.5$ arcmin, for different galaxy number densities $n_{eff} = 9, 30,$ and 60 gal/arcmin² (represented by the dashed, solid, and dash-dotted curves, respectively).

CHAPTER 7

CURRENT AND FUTURE WORK

7.1 Cluster Shapes

High resolution simulations of galaxy cluster formation carried out since the ground-breaking work of [Navarro et al. \(1997\)](#) confirm that the shapes of cluster-scale dark matter haloes often significantly depart from spherical symmetry. Haloes are mostly (football-shaped) prolate halos, with axis ratios between the shortest and longest axis as small as 0.4 (e.g., [Jing and Suto, 2002](#); [Shaw et al., 2006](#); [Bett et al., 2007](#); [Despali et al., 2014](#)). In fact, triaxial haloes are a direct consequence of initial mass density fluctuations that are described by a Gaussian random field undergoing gravitational collapse (e.g., [Doroshkevich, 1970](#)).

The degree to which cluster shapes differ from spherical symmetry also depends on the mass and redshift (e.g., [Despali et al., 2014](#)). If dark matter is in particle form, the shape of cluster haloes also reflects the interaction cross-section for dark matter particles (e.g., [Peter et al., 2013](#)). Galaxy clusters can also exhibit very complex structure due to merger activity (e.g., Abell 2146 [King et al., 2016](#)).

Understanding the shapes of galaxy clusters has a wide range of applications, which will be outlined below and further discussed in the Future Work Chapter.

Rachel Bowyer was an REU student at the Maria Mitchell Observatory NSF-REU program, advised by MF and LJK, and she continued working with us on her senior dissertation at Rice University. Using the Cosmo-OWLS moment of inertia tensors determined from the bound particles of each cluster, we obtained the Eigenvectors and Eigenvalues for each cluster. These were then used to give the true projected major axis and 3D orientation angle. These are our true values, to which we compared the projected orientation angles obtained from different methods. These results can be found in Figures [7.1](#), [7.2](#), [7.3](#), and [7.4](#).

Using cluster weak lensing shear data we can map out the signal-to-noise for real or synthetic data sets. These maps have the advantage of not being restricted to a specific

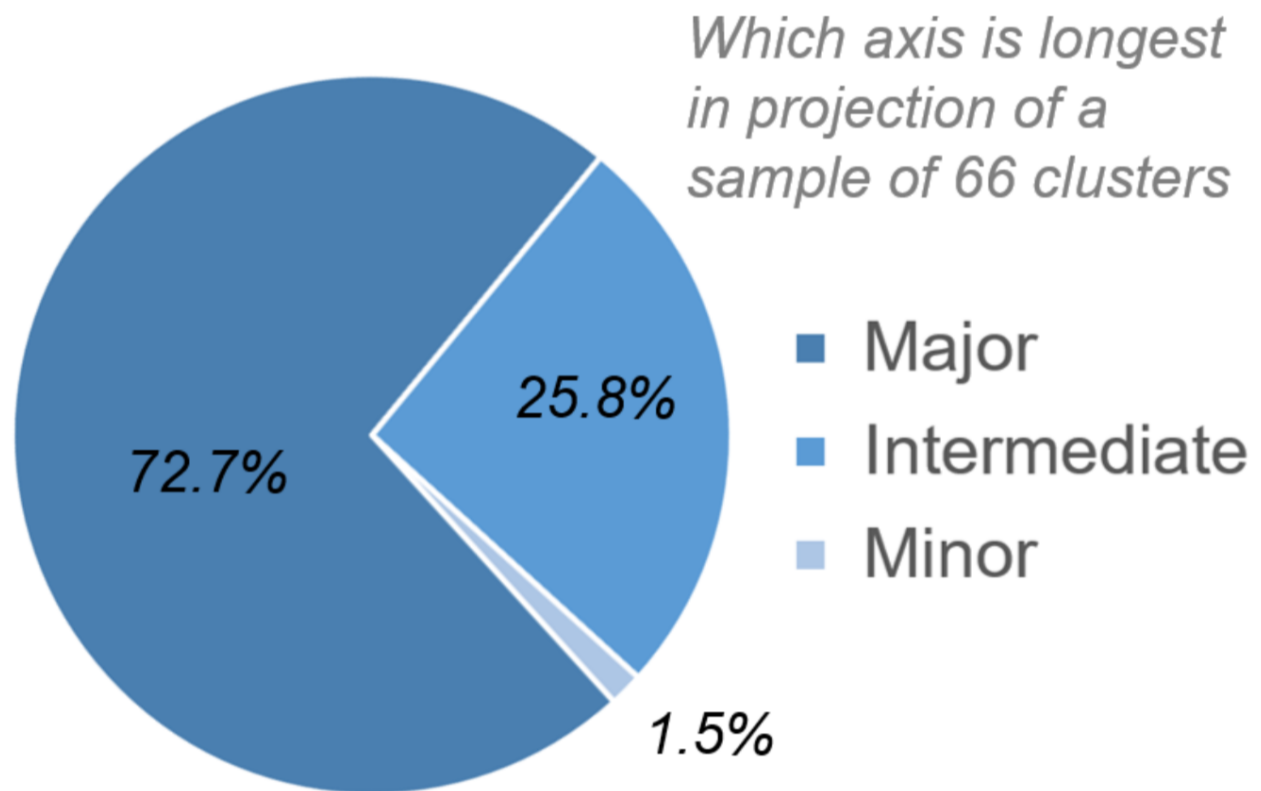


Figure 7.1: This shows, for 66 simulated clusters, how many true 3D major, intermediate, and minor axis are aligned with the projected major axis.

parametric form, and give us an estimate of the projected shapes of the clusters causing the lensing signals. This has been implemented by Miyoung Choi, Victoria Catlett (advised by MF and LJK) and Moutaz Haq (advised by MF and LJK) on a local machine and on a supercomputer at Texas Advanced Computing Center. From here we can fit to the aperture mass maps of clusters and determine the projected axis ratios and orientations, as outlined in the next paragraph. However, care must be taken, since different filter sizes may have an effect on the aperture maps, which can be seen in Figure [7.5](#).

Peter Gibson (Williamette University) was an REU student at the Maria Mitchell Observatory NSF-REU program, advised by MF and LJK. He created a code to obtain projected cluster axis ratios and orientation angles from Cosmo-OWLS clusters, by fitting ellipses to

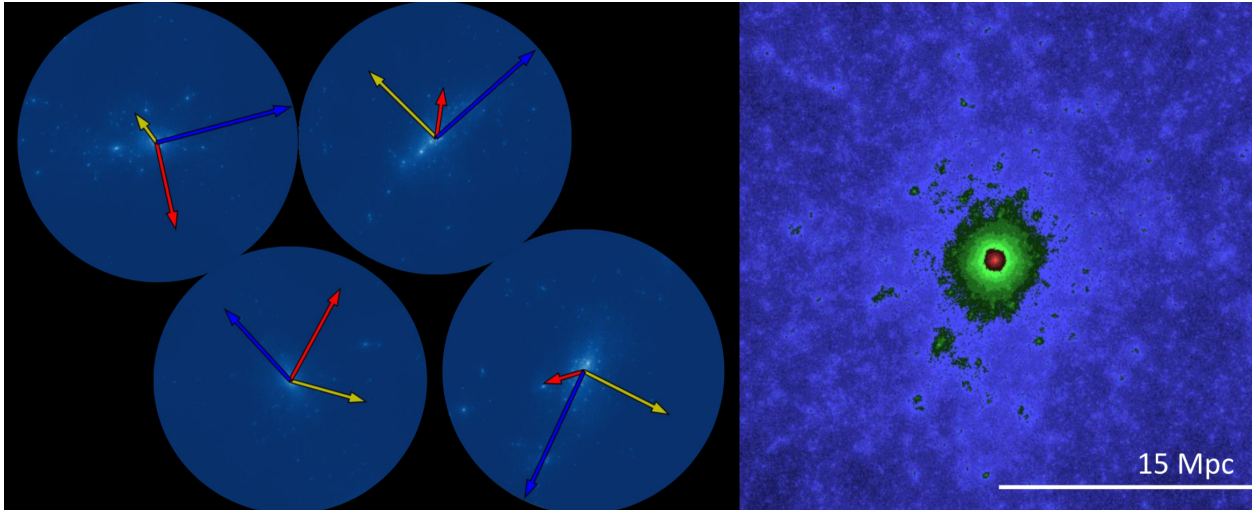


Figure 7.2: This shows stacked kappa maps for clusters without any orientation adjustments. The clusters here are extracted with line-of-sight along the z -direction, all sharing common x and y -hat directions. The blue, red, and yellow arrows represent the projected 3D major, intermediate, and minor axes of the moment of inertia of the cluster, respectively, where the 3D lengths are normalized to the radius of the circle. The longer the arrow, the smaller the angle between the axis and the lens plane, or x and y -hat directions. The stacked kappa maps here look spherical, as we'd expect.

the convergence and S/N contours. This was done by fitting over various bands of (real) convergence and of (reconstructed) S/N for each cluster to determine the orientation angles from the centers to the outskirts of clusters. Examples of the orientation fits on S/N and their comparisons with the true projected ellipsoid axes can be seen in Figures [7.6](#), [7.7](#), and [7.8](#).

Our research with Peter has also found many clusters that have very different orientation fits for the 10 different S/N bands. This suggests that the inner regions of those clusters have shapes that are very different from the outer regions, in other words mass isodensity twisting. By extracting the halo merger trees of these objects, which shows their formation history from smaller objects, we can correlate isodensity twisting with clusters that have gone through major mergers, such that two distinct clusters are no longer distinguishable on optical images. Hence this investigation of cosmological simulations might enable us to

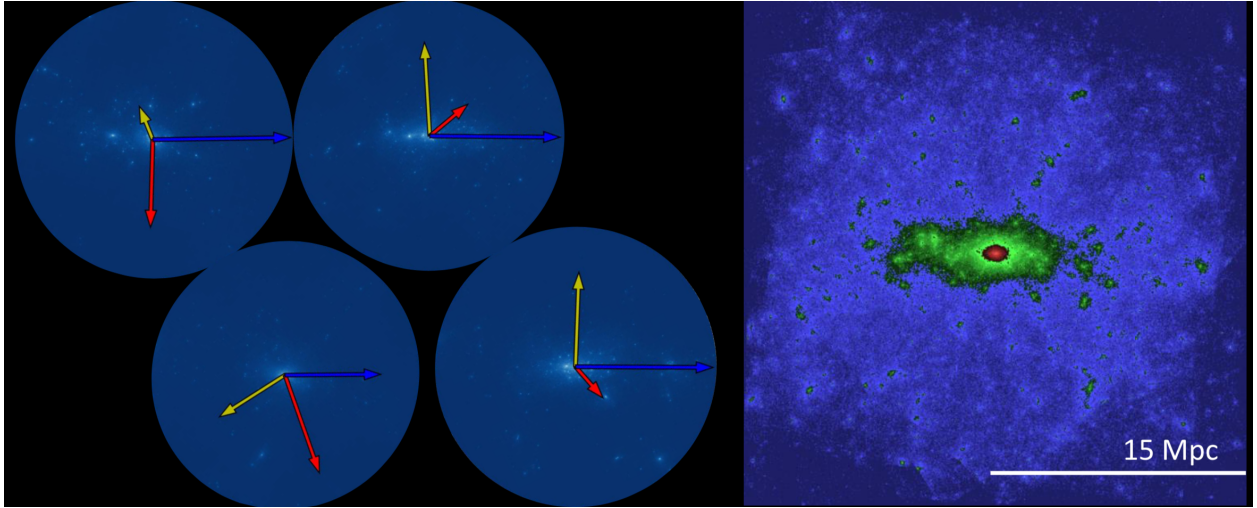


Figure 7.3: This shows stacked kappa maps for clusters while aligning their true 3D major axis. The blue, red, and yellow arrows represent the projected 3D major, intermediate, and minor axes of the moment of inertia of the cluster, respectively, where the 3D lengths are normalized to the radius of the circle. The longer the arrow, the smaller the angle between the axis and the lens plane, or x and y -hat directions. The clusters are similar to Figure 7.2, but with their orientation angle set to zero. The stack shows a stronger signal along the x -axis, where we'd expect a stronger shear signal. Using the shear signal along this axis, we may get better insight on how clusters are related to filaments.

identify a new means to detect clusters that have undergone major mergers via their lensing properties.

Along with Victoria Catlett, an undergraduate student at UTD (advised by MF and LJK) we are investigating how summed neutrino mass affects cluster shapes, assuming fiducial baryonic physics that best reproduces the observed properties of clusters. We were originally going to include this study into the Fong, Choi, Catlett et al. (2019) paper but we decided to make it a separate publication. Using BAHAMAS we have calculated the moment of inertia tensors at the present day ($z = 0$) for the most massive 2,000 clusters, for each of the runs with neutrino mass of 0.06, 0.12, 0.24, and 0.48 eV. With the moment of inertia data we compare the axis ratios of the clusters in Figure 7.9. This will be the first detailed study of cluster shapes in cosmological simulations that self consistently include baryonic physics and massive neutrinos.

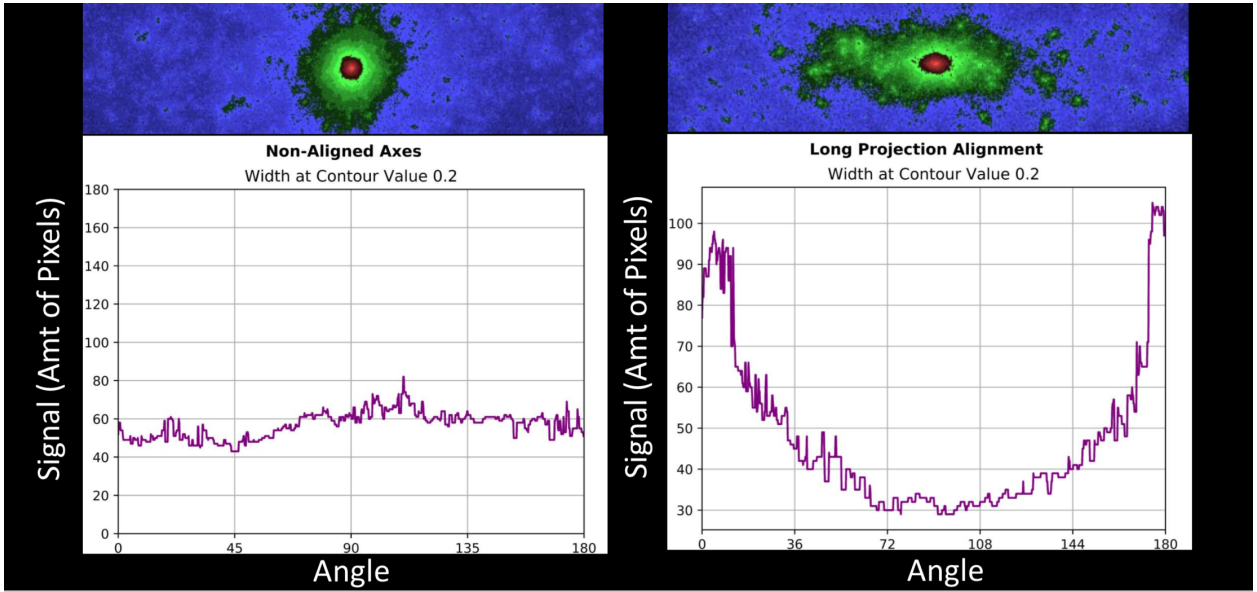


Figure 7.4: These plots show the pixel distance, to a contour value of 0.2, against the angle starting from the x-axis. For the left panel, this shows that the stack kappa drops to 0.2 at almost a constant pixel distance from the center. For the right panel, this shows that the stack kappa drops to 0.2 further out for the angles along the x-direction as opposed the the others.

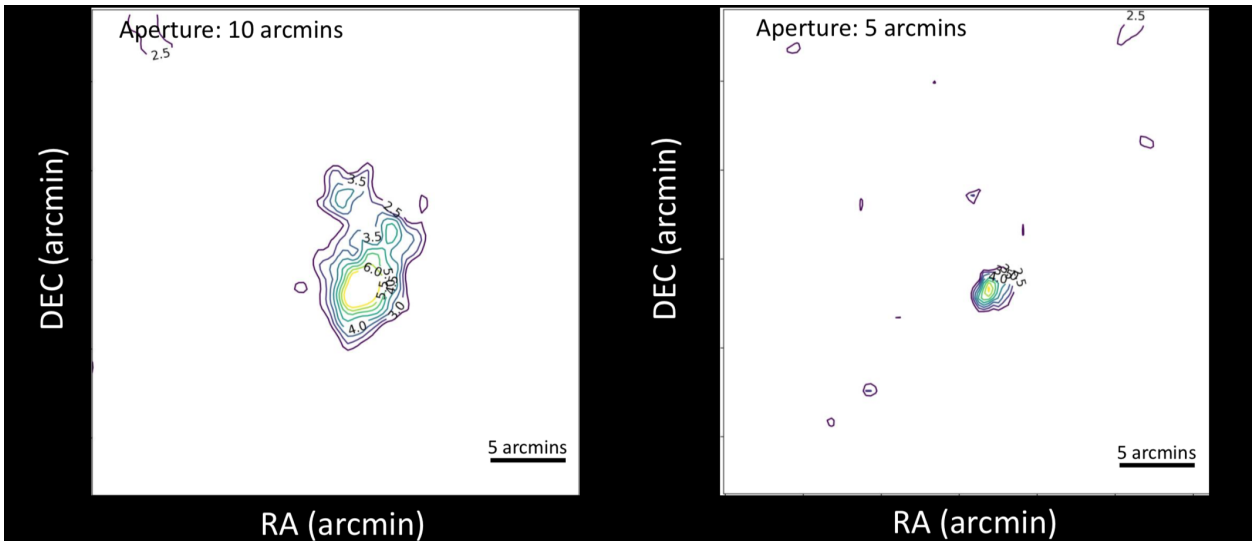


Figure 7.5: These plots show the aperture mass signal-to-noise maps of the same cluster, but with different aperture mass sizes. The left panel shows an aperture size of 10 arcmin while the right shows 5 arcmin. If an ellipse is applied to these maps, we may obtain slightly different orientation angles. So we will need to study how aperture sizes effects the shape and orientation of the maps. This can be done by comparing the orientations to the true orientation values found in Rachel's work.

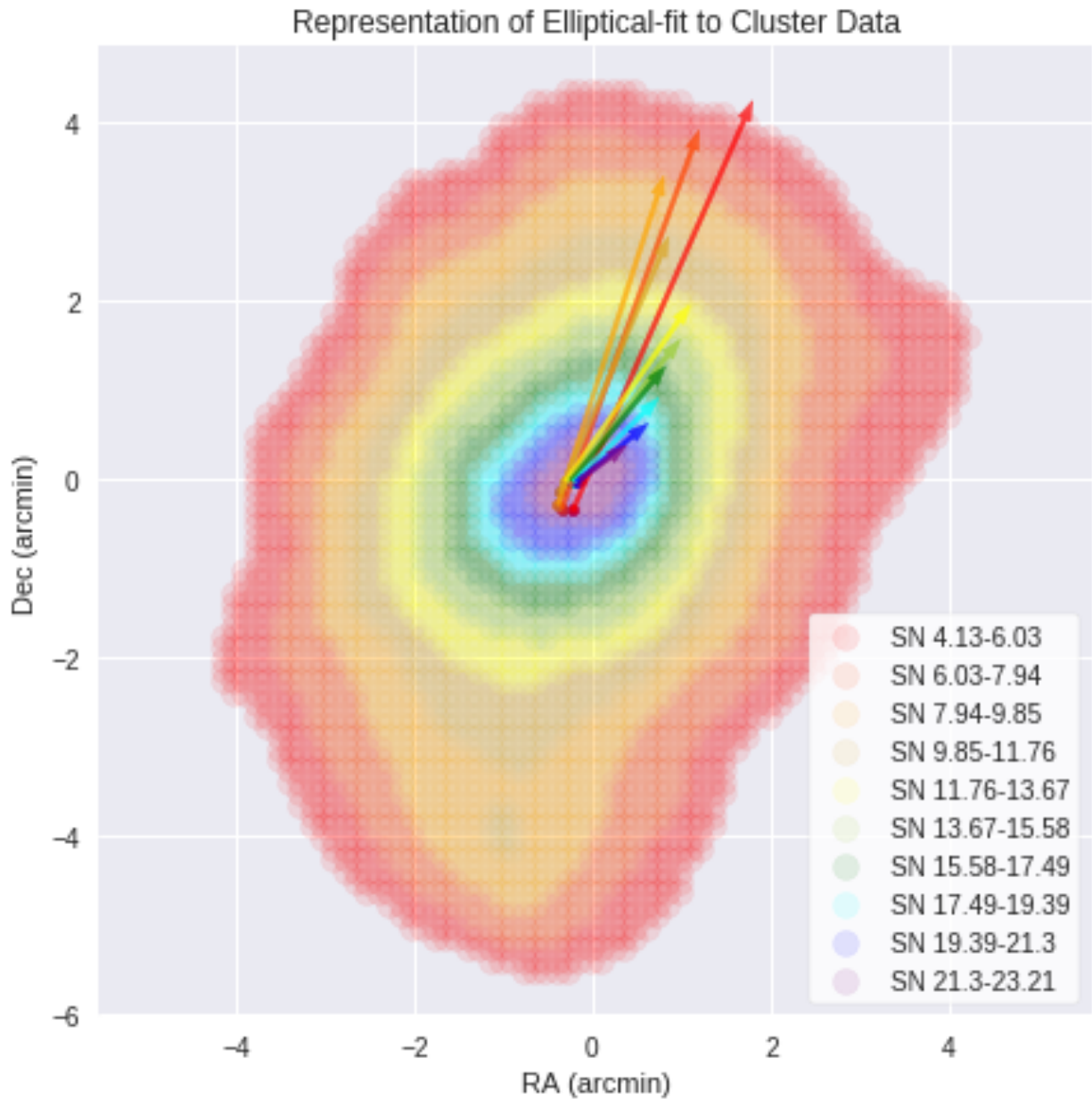


Figure 7.6: This plot shows an example of ellipse orientation fit results for 10 S/N band for a particular cluster (FoF ID 6). The orientation results vary depending on which S/N band is used. Note that the S/N values are very large in this example because we are using ideal shear in this example and not adding any shape noise to the ellipticities before calculating the aperture mass, or S/N map.

We are currently developing a Python pipeline to fit triaxial mass models to galaxy cluster data. We will use this pipeline to carry out an analysis of the CLASH sample

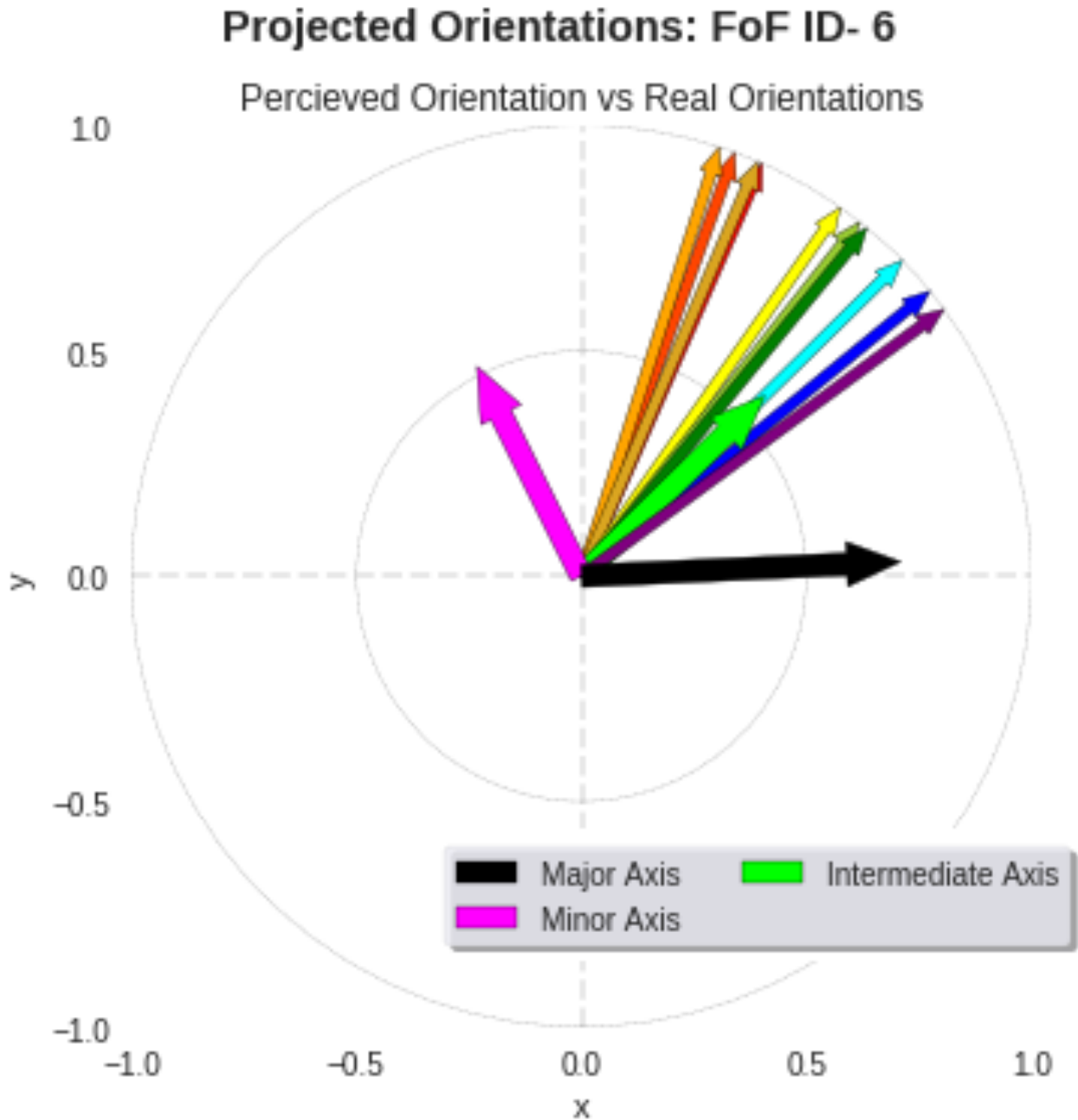


Figure 7.7: A comparison of the orientation angles (colors corresponding to the 10 S/N bands, See Figure 7.6) and the true projected major, intermediate, and minor axis of the ellipsoid of the cluster, determined from the moment of inertia (FoF ID 6). In this case most ellipse orientations do not agree with the projected major axis.

(Postman et al., 2012) using their weak lensing, strong lensing, X-ray, and SZ data. I am continuing Brandyn Lee's work on triaxiality, developing Python code that produces

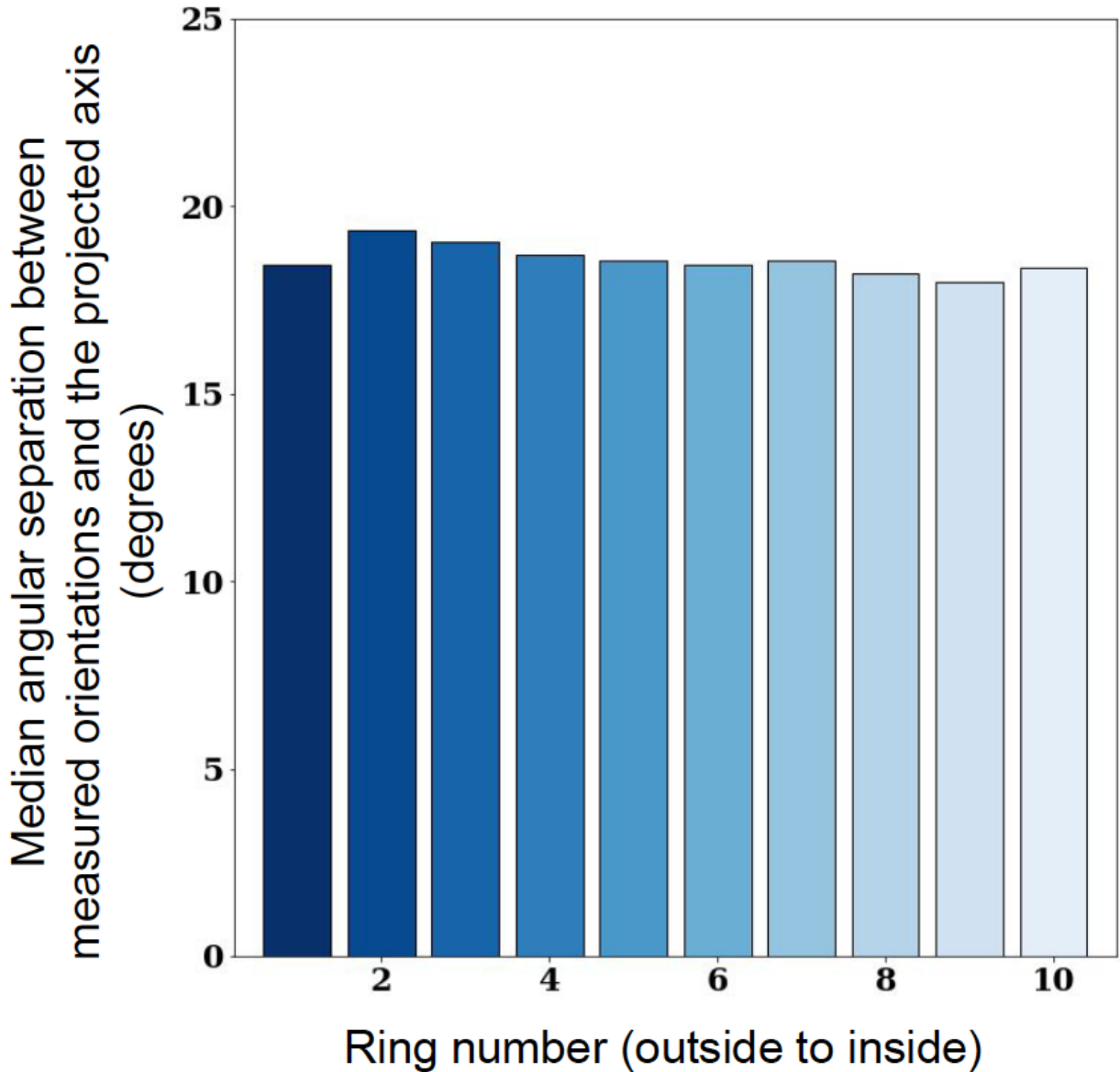


Figure 7.8: The median angular separation, between the orientation angle and the projected major axis for the 10 rings, for the most massive clusters. All S/N rings on average have similar orientation predictability.

a triaxial NFW mass density (Stark, 1977; Binney, 1985; Oguri et al., 2003) to represent clusters beyond spherical shapes. Brandyn wrote Python code using the MCMC algorithm to fit over weak lensing data using X-ray, SZ, and strong lensing priors. This can potentially be a very powerful tool in estimating cluster parameters, being more accurate than the

Density of Halo Axis Ratio Values

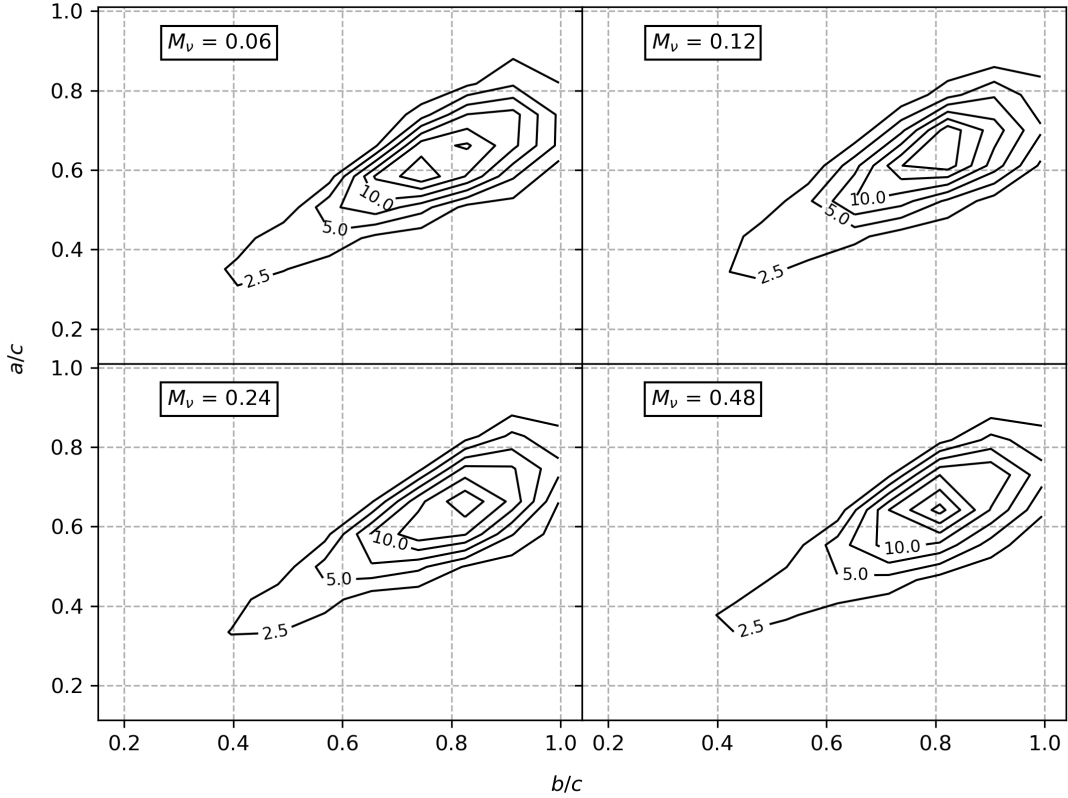


Figure 7.9: The contours are the lines of constant distribution density of a/c vs. b/c distributions for varying summed neutrino mass (eV). The values plotted are the contour values.

spherical NFW model. For example, assuming a spherical NFW to fit onto a prolate cluster can result in a 50% difference in mass (Corless and King, 2007). Examples of the triaxial NFW for the 3D density, convergence, and reduced shear can be seen in Figures 7.10, 7.11, and 7.12 respectively. The cluster mass function is sensitive to cosmological parameters. We will eventually investigate how well spherical vs. triaxial NFW cluster mass fits will do in deriving the cluster mass function and constraining cosmological parameters σ_8 and Ω_m . Although lower mass clusters will be stacked to obtain an average lensing signal, which will greatly minimize the impact of cluster shape on cosmological parameter determination from

the cluster mass function, there are other statistics which rely on the most massive rare clusters where individual triaxial masses with accurate error bars.

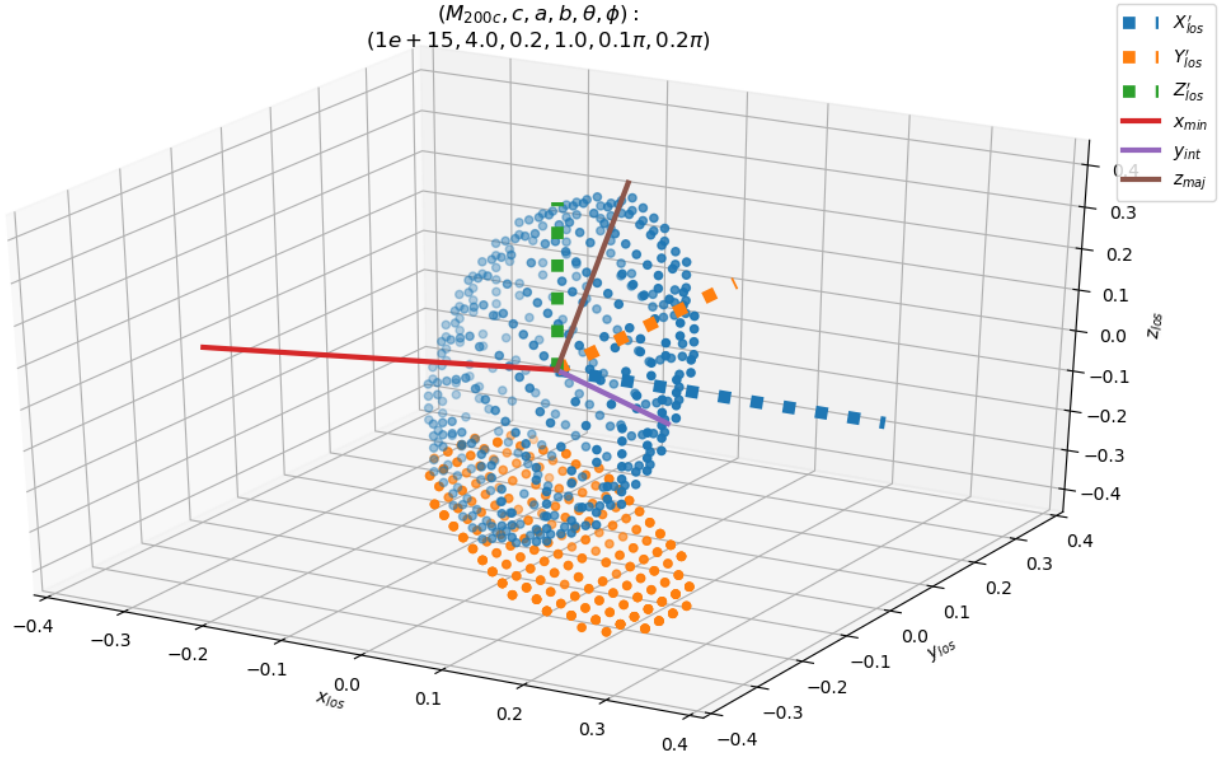


Figure 7.10: An example 3D map of the triaxial NFW density. Plotted here is a small band of density for the triaxial NFW model, shown in blue dots. Projecting the points along the Z'_{los} -direction gives an idea of how the convergence shape should appear on the $X'_{\text{los}}-Y'_{\text{los}}$ plane, shown as orange dots. The dashed lines are the X'_{los} , Y'_{los} , and Z'_{los} the line-of-sight orthogonal coordinates, and the solid lines are the minor, intermediate, and major axis of the triaxial halo, x_{min} , y_{int} , and z_{maj} respectively. The parameters M_{200c} , c , a , b , θ , ϕ are the triaxial NFW parameters. M_{200c} and c are the NFW mass and concentration, a and b are the minor and intermediate axes scaled by the major axis, θ is the angle between Z'_{los} and z_{maj} , and ϕ is the angle between the projected Z'_{los} (onto the $x_{\text{min}}-y_{\text{int}}$ plane) and $-X'_{\text{los}}$, where X'_{los} is constrained to be in the $x_{\text{min}}-y_{\text{int}}$ plane.

The triaxial NFW model has 6 parameters and the time to generate the convergence and shear is non-negligible. Therefore any tightening on the priors for the MCMC process will significantly improve our constraints and computation time. In addition to using X-ray, SZ priors, and strong lensing priors, we can use our work with Peter Gibson on fitting

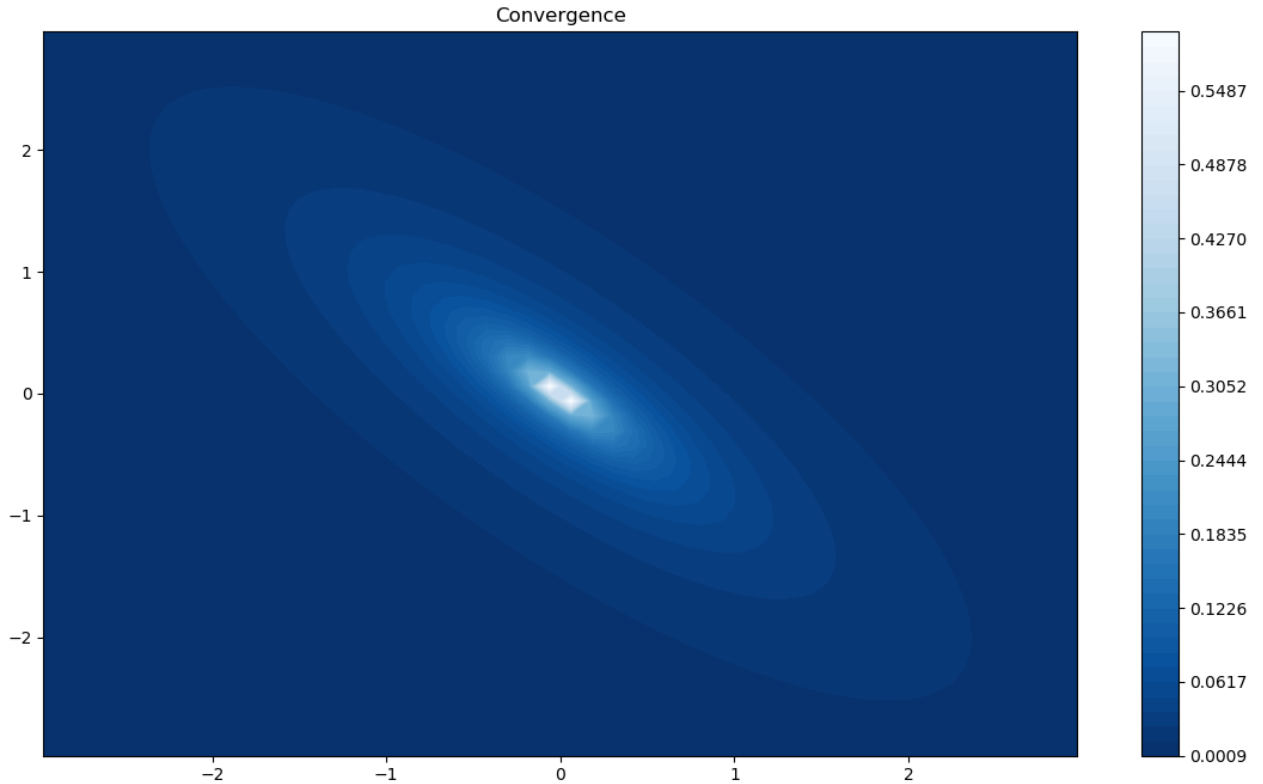


Figure 7.11: The convergence of the triaxial NFW halo shown in Figure [7.10](#).

ellipses onto shear maps, to restrict the parameter space being explored. We will eventually train Peter’s ellipse fitting code onto BAHAMAS clusters incorporating full line-of-sight structure with specific survey characteristics, as opposed to Cosmo-OWLS clusters, to obtain appropriate error bars on orientation estimates. These results will then be used to motivate the uncertainties on CLASH cluster projected orientation angles.

7.2 Other Future Work

Throughout my graduate career, I have worked closely with LSST/DESC. We worked in the CLMM (Cluster Mass Models) working group to create a module that produces weak lensing shear profiles for any input spherical mass density profile. The CLMM module will be developed to fit a large volume of cluster weak lensing data from LSST.

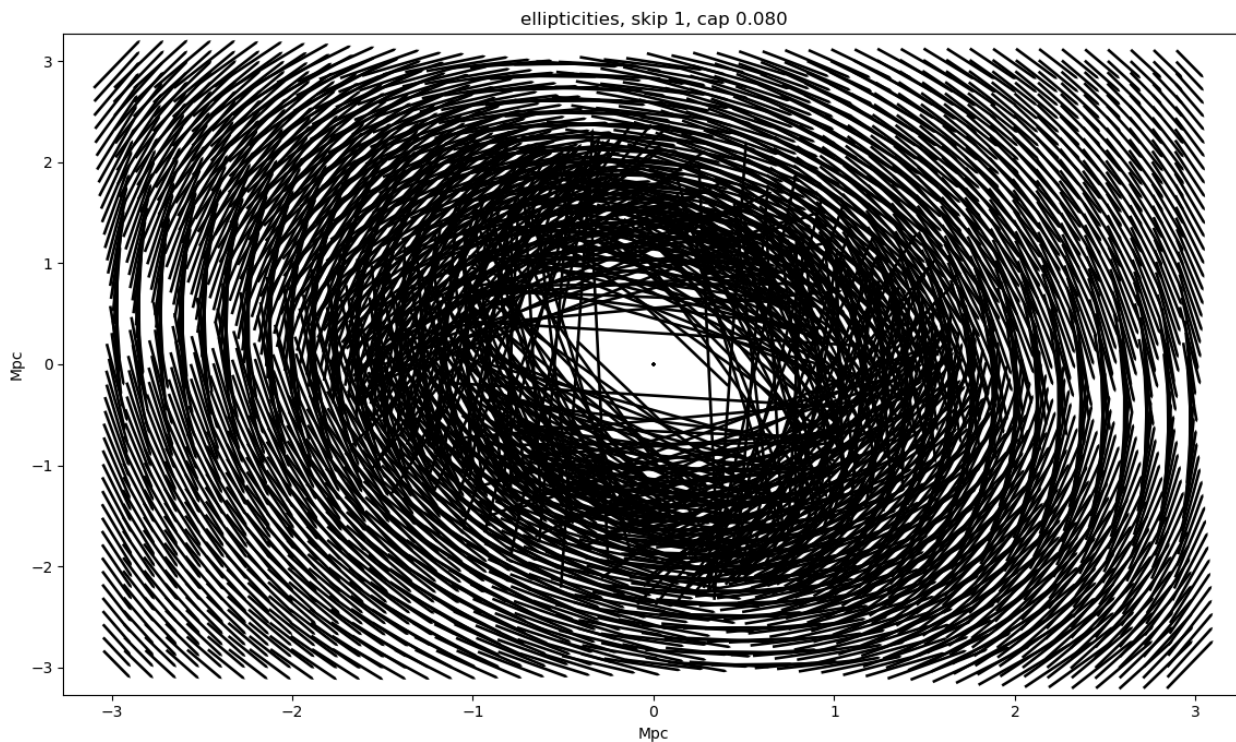


Figure 7.12: The reduced shear of the triaxial NFW halo shown in Figure [7.10](#).

Now that we have access to BAHAMAS light-cones (where we have also been incorporating cosmic shear into our results), it will be very interesting to studying how the splashback radius, r_{sp} parameterized by the DK profile ([Diemer and Kravtsov, 2014](#)), changes with summed neutrino mass. In other words, we can properly study how neutrino mass impacts on the rates at which matter falls into clusters, or the evolution of clusters. It would also be interesting to investigate cluster formation and evolution in more detail, in particular the (average) lensing signatures of clusters in simulations grouped by redshift, baryonic prescriptions, and neutrino mass.

In our work above we study the spherical DK model after stacking weak lensing signals of many clusters. This gives us an idea of how cluster densities fall off to the mean matter density of the Universe and tells us the rate at which the clusters accrete matter from their surroundings. However, if we wish to study clusters in context of the cosmic web, we will attempt to wedge out the shear signals that aren't due to the filaments. An issue is that

the filaments feeding from the web into a cluster have a very small impact on the shear signal. However, the major axis of clusters tends to align with filaments (Hahn et al., 2007; Ganeshiah Veena et al., 2018). So we can boost the signal-to-noise of the shear due to filaments by aligning the major axes of the clusters and stack their shear signals. The orientation angle of clusters, as discussed just above, will be crucial in stacking cluster weak lensing data by their projected major axis. After stacking the shear maps with their orientations aligned, we will fit the DK profile onto the stacked shear map with alignment to study the impact on parameters such as the splashback radius along the major axis. This will tell us how the rate of matter infalling towards clusters major axes (with a higher probability being along filaments) differs from the general environment.

REFERENCES

- Addison, G. E., Y. Huang, D. J. Watts, C. L. Bennett, M. Halpern, G. Hinshaw, and J. L. Weiland (2016, feb). QUANTIFYING DISCORDANCE IN THE 2015planckcmb SPECTRUM. *The Astrophysical Journal* 818(2), 132.
- Allen, S. W., A. E. Evrard, and A. B. Mantz (2011, September). Cosmological Parameters from Observations of Galaxy Clusters. *ARA&A* 49, 409–470.
- Alpher, R. A. and R. Herman (1948, November). Evolution of the Universe. *Nature* 162, 774–775.
- Amendola, L., S. Appleby, A. Avgoustidis, D. Bacon, T. Baker, M. Baldi, N. Bartolo, A. Blanchard, C. Bonvin, S. Borgani, E. Branchini, C. Burrage, S. Camera, C. Carbone, L. Casarini, M. Cropper, C. de Rham, J. P. Dietrich, C. Di Porto, R. Durrer, A. Ealet, P. G. Ferreira, F. Finelli, J. García-Bellido, T. Giannantonio, L. Guzzo, A. Heavens, L. Heisenberg, C. Heymans, H. Hoekstra, L. Hollenstein, R. Holmes, Z. Hwang, K. Jahnke, T. D. Kitching, T. Koivisto, M. Kunz, G. La Vacca, E. Linder, M. March, V. Marra, C. Martins, E. Majerotto, D. Markovic, D. Marsh, F. Marulli, R. Massey, Y. Mellier, F. Montanari, D. F. Mota, N. J. Nunes, W. Percival, V. Pettorino, C. Porciani, C. Quercellini, J. Read, M. Rinaldi, D. Sapone, I. Sawicki, R. Scaramella, C. Skordis, F. Simpson, A. Taylor, S. Thomas, R. Trotta, L. Verde, F. Vernizzi, A. Vollmer, Y. Wang, J. Weller, and T. Zlosnik (2018, April). Cosmology and fundamental physics with the Euclid satellite. *Living Reviews in Relativity* 21, 2.
- Applegate, D. E., A. von der Linden, P. L. Kelly, M. T. Allen, S. W. Allen, P. R. Burchat, D. L. Burke, H. Ebeling, A. Mantz, and R. G. Morris (2014, March). Weighing the Giants - III. Methods and measurements of accurate galaxy cluster weak-lensing masses. *MNRAS* 439, 48–72.
- Bard, D., M. Bellis, M. T. Allen, H. Yepremyan, and J. M. Kratochvil (2012, Aug). Cosmological Calculations on the GPU. *arXiv e-prints*, arXiv:1208.3658.
- Bartelmann, M. (1996, September). Arcs from a universal dark-matter halo profile. *A&A* 313, 697–702.
- Bashinsky, S. and U. Seljak (2004, April). Signatures of relativistic neutrinos in CMB anisotropy and matter clustering. *Phys. Rev. D* 69, 083002.
- Battye, R. A. and A. Moss (2014, February). Evidence for Massive Neutrinos from Cosmic Microwave Background and Lensing Observations. *Physical Review Letters* 112(5), 051303.

- Bett, P., V. Eke, C. S. Frenk, A. Jenkins, J. Helly, and J. Navarro (2007, March). The spin and shape of dark matter haloes in the Millennium simulation of a Λ cold dark matter universe. *MNRAS* *376*, 215–232.
- Bhattacharya, D., R. Misra, A. R. Rao, and P. Sreekumar (2013, May). The uncorrelated long-term γ -ray and X-ray variability of blazars and its implications on disc-jet coupling. *MNRAS* *431*, 1618–1624.
- Binney, J. (1985, February). Testing for triaxiality with kinematic data. *MNRAS* *212*, 767–781.
- Bird, S., M. Viel, and M. G. Haehnelt (2012, March). Massive neutrinos and the non-linear matter power spectrum. *MNRAS* *420*, 2551–2561.
- Blumenthal, G. R., S. M. Faber, J. R. Primack, and M. J. Rees (1984). Formation of galaxies and large-scale structure with cold dark matter. *Nature* *311*, 517–525.
- Bond, J. R., G. Efstathiou, and J. Silk (1980). Massive neutrinos and the large-scale structure of the universe. *Phys. Rev. Lett.* *45*.
- Booth, C. M. and J. Schaye (2009, September). Cosmological simulations of the growth of supermassive black holes and feedback from active galactic nuclei: method and tests. *MNRAS* *398*, 53–74.
- Bullock, J. S., T. S. Kolatt, Y. Sigad, R. S. Somerville, A. V. Kravtsov, A. A. Klypin, J. R. Primack, and A. Dekel (2001, March). Profiles of dark haloes: evolution, scatter and environment. *MNRAS* *321*, 559–575.
- Castorina, E., E. Sefusatti, R. K. Sheth, F. Villaescusa-Navarro, and M. Viel (2014, February). Cosmology with massive neutrinos II: on the universality of the halo mass function and bias. *Journal of Cosmology and Astro-Particle Physics* *2014*, 049.
- Chang, C., E. Baxter, B. Jain, C. Sánchez, S. Adhikari, T. N. Varga, Y. Fang, E. Rozo, E. S. Rykoff, A. Kravtsov, D. Gruen, E. M. Huff, M. Jarvis, A. G. Kim, J. Prat, N. MacCrann, T. McClintock, A. Palmese, D. Rapetti, R. P. Rollins, S. Samuroff, E. Sheldon, M. A. Troxel, R. H. Wechsler, Y. Zhang, J. Zuntz, T. M. C. Abbott, F. B. Abdalla, S. Allam, J. Annis, K. Bechtol, A. Benoit-Lévy, G. M. Bernstein, D. Brooks, E. Buckley-Geer, A. Carnero Rosell, M. Carrasco Kind, J. Carretero, C. B. D’Andrea, L. N. da, C. Davis, S. Desai, H. T. Diehl, J. P. Dietrich, A. Drlica-Wagner, T. F. Eifler, B. Flaugher, P. Fosalba, J. Frieman, J. García-Bellido, E. Gaztanaga, D. W. Gerdes, R. A. Gruendl, J. Gschwend, G. Gutierrez, K. Honscheid, D. J. James, T. Jeltema, E. Krause, K. Kuehn, O. Lahav, M. Lima, M. March, J. L. Marshall, P. Martini, P. Melchior, F. Menanteau, R. Miquel, J. J. Mohr, B. Nord, R. L. C. Ogando, A. A. Plazas, E. Sanchez, V. Scarpine, R. Schindler, M. Schubnell, I. Sevilla-Noarbe, R. C. Smith, M. Smith, M. Soares-Santos,

- F. Sobreira, E. Suchyta, M. E. C. Swanson, G. Tarle, and J. Weller (2017, October). The Splashback Feature around DES Galaxy Clusters: Galaxy Density and Weak Lensing Profiles. *ArXiv e-prints*.
- Chang, C., M. Jarvis, B. Jain, S. M. Kahn, D. Kirkby, A. Connolly, S. Krughoff, E.-H. Peng, and J. R. Peterson (2013, September). The effective number density of galaxies for weak lensing measurements in the LSST project. *MNRAS* *434*, 2121–2135.
- Clowe, D., G. De Lucia, and L. King (2004, May). Effects of asphericity and substructure on the determination of cluster mass with weak gravitational lensing. *MNRAS* *350*, 1038–1048.
- Cooray, A. and R. Sheth (2002, December). Halo models of large scale structure. *Phys. Rep.* *372*, 1–129.
- Corless, V. L. and L. J. King (2007, September). A statistical study of weak lensing by triaxial dark matter haloes: consequences for parameter estimation. *MNRAS* *380*, 149–161.
- Costanzi, M., F. Villaescusa-Navarro, M. Viel, J.-Q. Xia, S. Borgani, E. Castorina, and E. Sefusatti (2013, December). Cosmology with massive neutrinos III: the halo mass function and an application to galaxy clusters. *Journal of Cosmology and Astro-Particle Physics* *2013*, 012.
- Cusworth, S. J., S. T. Kay, R. A. Battye, and P. A. Thomas (2014, April). Impact of baryons on the cluster mass function and cosmological parameter determination. *MNRAS* *439*, 2485–2493.
- Dalla Vecchia, C. and J. Schaye (2008, July). Simulating galactic outflows with kinetic supernova feedback. *MNRAS* *387*, 1431–1444.
- Despali, G., C. Giocoli, and G. Tormen (2014, Oct). Some like it triaxial: the universality of dark matter halo shapes and their evolution along the cosmic time. *MNRAS* *443*, 3208–3217.
- Di Valentino, E., A. Melchiorri, E. V. Linder, and J. Silk (2017, Jul). Constraining dark energy dynamics in extended parameter space. *Phys. Rev. D* *96*, 023523.
- Diemer, B. (2017, December). COLOSSUS: A python toolkit for cosmology, large-scale structure, and dark matter halos. *ArXiv e-prints*.
- Diemer, B. and A. V. Kravtsov (2014, July). Dependence of the Outer Density Profiles of Halos on Their Mass Accretion Rate. *ApJ* *789*, 1.
- Diemer, B. and A. V. Kravtsov (2015, January). A Universal Model for Halo Concentrations. *ApJ* *799*, 108.

- Dietrich, J. P. and J. Hartlap (2010, February). Cosmology with the shear-peak statistics. *MNRAS* *402*, 1049–1058.
- Dodelson, S. (2004, July). CMB-cluster lensing. *Phys. Rev. D* *70*(2), 023009.
- Dolag, K., S. Borgani, G. Murante, and V. Springel (2009, October). Substructures in hydrodynamical cluster simulations. *MNRAS* *399*, 497–514.
- Doroshkevich, A. G. (1970, October). Spatial structure of perturbations and origin of galactic rotation in fluctuation theory. *Astrophysics* *6*, 320–330.
- Dubois, Y., C. Pichon, C. Welker, D. Le Borgne, J. Devriendt, C. Laigle, S. Codis, D. Pogosyan, S. Arnouts, K. Benabed, E. Bertin, J. Blaizot, F. Bouchet, J.-F. Cardoso, S. Colombi, V. de Lapparent, V. Desjacques, R. Gavazzi, S. Kassin, T. Kimm, H. McCracken, B. Milliard, S. Peirani, S. Prunet, S. Rouberol, J. Silk, A. Slyz, T. Sousbie, R. Teyssier, L. Tresse, M. Treyer, D. Vibert, and M. Volonteri (2014, October). Dancing in the dark: galactic properties trace spin swings along the cosmic web. *MNRAS* *444*, 1453–1468.
- Duffy, A. R., J. Schaye, S. T. Kay, and C. Dalla Vecchia (2008, October). Dark matter halo concentrations in the Wilkinson Microwave Anisotropy Probe year 5 cosmology. *MNRAS* *390*, L64–L68.
- Dutton, A. A. and A. V. Macciò (2014, July). Cold dark matter haloes in the Planck era: evolution of structural parameters for Einasto and NFW profiles. *MNRAS* *441*, 3359–3374.
- Einasto, J. (1965). On the Construction of a Composite Model for the Galaxy and on the Determination of the System of Galactic Parameters. *Trudy Astrofizicheskogo Instituta Alma-Ata* *5*, 87–100.
- Einstein, A. (1916). Die Grundlage der allgemeinen Relativitätstheorie. *Annalen der Physik* *354*, 769–822.
- Fan, Z., H. Shan, and J. Liu (2010, August). Noisy Weak-lensing Convergence Peak Statistics Near Clusters of Galaxies and Beyond. *ApJ* *719*, 1408–1420.
- Feeney, S. M., D. J. Mortlock, and N. Dalmaso (2018, May). Clarifying the Hubble constant tension with a Bayesian hierarchical model of the local distance ladder. *MNRAS* *476*, 3861–3882.
- Fong, M., R. Bowyer, A. Whitehead, B. Lee, L. King, D. Applegate, and I. McCarthy (2018, Aug). Prospects for determining the mass distributions of galaxy clusters on large scales using weak gravitational lensing. *MNRAS* *478*, 5366–5378.

- Friedrich, J. O., N. Adhikari, and J. Beyene (2008, May). The ratio of means method as an alternative to mean differences for analyzing continuous outcome variables in meta-analysis: A simulation study. *BMC Medical Research Methodology* 8(1), 32.
- Fukushige, T. and J. Makino (2001, August). Structure of Dark Matter Halos from Hierarchical Clustering. *ApJ* 557, 533–545.
- Ganeshiah Veena, P., M. Cautun, R. van de Weygaert, E. Tempel, B. J. T. Jones, S. Rieder, and C. S. Frenk (2018, November). The Cosmic Ballet: spin and shape alignments of haloes in the cosmic web. *MNRAS* 481, 414–438.
- Gratton, S., A. Lewis, and G. Efstathiou (2008, April). Prospects for constraining neutrino mass using Planck and Lyman- α forest data. *Phys. Rev. D* 77, 083507.
- Haardt, F. and P. Madau (2001). Modelling the UV/X-ray cosmic background with CUBA. pp. 64.
- Hagstotz, S., M. Costanzi, M. Baldi, and J. Weller (2018, June). Joint halo mass function for modified gravity and massive neutrinos I: simulations and cosmological forecasts. *arXiv e-prints*, arXiv:1806.07400.
- Hahn, O., C. M. Carollo, C. Porciani, and A. Dekel (2007, October). The evolution of dark matter halo properties in clusters, filaments, sheets and voids. *MNRAS* 381, 41–51.
- Hamana, T., M. Oguri, M. Shirasaki, and M. Sato (2012, September). Scatter and bias in weak lensing selected clusters. *MNRAS* 425, 2287–2298.
- Hamana, T., M. Takada, and N. Yoshida (2004, May). Searching for massive clusters in weak lensing surveys. *MNRAS* 350, 893–913.
- Hannestad, S., H. Tu, and Y. Y. Wong (2006, June). Measuring neutrino masses and dark energy with weak lensing tomography. *Journal of Cosmology and Astro-Particle Physics* 2006, 025.
- Hayashi, E. and S. D. M. White (2008, July). Understanding the halo-mass and galaxy-mass cross-correlation functions. *MNRAS* 388, 2–14.
- Hennawi, J. F. and D. N. Spergel (2005, May). Shear-selected Cluster Cosmology: Tomography and Optimal Filtering. *ApJ* 624, 59–79.
- Henson, M. A., D. J. Barnes, S. T. Kay, I. G. McCarthy, and J. Schaye (2017, March). The impact of baryons on massive galaxy clusters: halo structure and cluster mass estimates. *MNRAS* 465, 3361–3378.

- Hetterscheidt, M., T. Erben, P. Schneider, R. Maoli, L. van Waerbeke, and Y. Mellier (2005, October). Searching for galaxy clusters using the aperture mass statistics in 50 VLT fields. *A&A* *442*, 43–61.
- Heymans, C., L. Van Waerbeke, L. Miller, T. Erben, H. Hildebrandt, H. Hoekstra, T. D. Kitching, Y. Mellier, P. Simon, C. Bonnett, J. Coupon, L. Fu, J. Harnois Déraps, M. J. Hudson, M. Kilbinger, K. Kuijken, B. Rowe, T. Schrabback, E. Semboloni, E. van Uitert, S. Vafaei, and M. Velander (2012, November). CFHTLenS: the Canada-France-Hawaii Telescope Lensing Survey. *MNRAS* *427*, 146–166.
- Hildebrandt, H., M. Viola, C. Heymans, S. Joudaki, K. Kuijken, C. Blake, T. Erben, B. Joachimi, D. Klaes, L. Miller, C. B. Morrison, R. Nakajima, G. Verdoes Kleijn, A. Amon, A. Choi, G. Covone, J. T. A. de Jong, A. Dvornik, I. Fenech Conti, A. Grado, J. Harnois-Déraps, R. Herbonnet, H. Hoekstra, F. Köhlinger, J. McFarland, A. Mead, J. Merten, N. Napolitano, J. A. Peacock, M. Radovich, P. Schneider, P. Simon, E. A. Valentijn, J. L. van den Busch, E. van Uitert, and L. Van Waerbeke (2017, February). KiDS-450: cosmological parameter constraints from tomographic weak gravitational lensing. *MNRAS* *465*, 1454–1498.
- Hinshaw, G., D. Larson, E. Komatsu, D. N. Spergel, C. L. Bennett, J. Dunkley, M. R. Nolte, M. Halpern, R. S. Hill, N. Odegard, L. Page, K. M. Smith, J. L. Weiland, B. Gold, N. Jarosik, A. Kogut, M. Limon, S. S. Meyer, G. S. Tucker, E. Wollack, and E. L. Wright (2013, October). Nine-year Wilkinson Microwave Anisotropy Probe (WMAP) Observations: Cosmological Parameter Results. *ApJ* *208*, 19.
- Hoekstra, H. (2003, March). How well can we determine cluster mass profiles from weak lensing? *MNRAS* *339*, 1155–1162.
- Hu, W. (2001, August). Mapping the Dark Matter through the Cosmic Microwave Background Damping Tail. *ApJl* *557*, L79–L83.
- Hu, W. and S. Dodelson (2002). Cosmic Microwave Background Anisotropies. *ARA&A* *40*, 171–216.
- Hu, W., D. J. Eisenstein, and M. Tegmark (1998, June). Weighing Neutrinos with Galaxy Surveys. *Phys. Rev. Lett.* *80*, 5255–5258.
- Hubble, E. (1929, March). A Relation between Distance and Radial Velocity among Extra-Galactic Nebulae. *Proceedings of the National Academy of Science* *15*, 168–173.
- Jain, B. and L. V. Waerbeke (2000, feb). Statistics of dark matter halos from gravitational lensing. *The Astrophysical Journal* *530*(1), L1–L4.
- Jing, Y. P. and Y. Suto (2000, February). The Density Profiles of the Dark Matter Halo Are Not Universal. *ApJl* *529*, L69–L72.

- Jing, Y. P. and Y. Suto (2002, August). Triaxial Modeling of Halo Density Profiles with High-Resolution N-Body Simulations. *ApJ* 574, 538–553.
- Kacprzak, T., D. Kirk, O. Friedrich, A. Amara, A. Refregier, L. Marian, J. P. Dietrich, E. Suchyta, J. Aleksić, D. Bacon, M. R. Becker, C. Bonnett, S. L. Bridle, C. Chang, T. F. Eifler, W. G. Hartley, E. M. Huff, E. Krause, N. MacCrann, P. Melchior, A. Nicola, S. Samuroff, E. Sheldon, M. A. Troxel, J. Weller, J. Zuntz, T. M. C. Abbott, F. B. Abdalla, R. Armstrong, A. Benoit-Lévy, G. M. Bernstein, R. A. Bernstein, E. Bertin, D. Brooks, D. L. Burke, A. Carnero Rosell, M. Carrasco Kind, J. Carretero, F. J. Castander, M. Crocce, C. B. D’Andrea, L. N. da Costa, S. Desai, H. T. Diehl, A. E. Evrard, A. F. Neto, B. Flaugher, P. Fosalba, J. Frieman, D. W. Gerdes, D. A. Goldstein, D. Gruen, R. A. Gruendl, G. Gutierrez, K. Honscheid, B. Jain, D. J. James, M. Jarvis, K. Kuehn, N. Kuropatkin, O. Lahav, M. Lima, M. March, J. L. Marshall, P. Martini, C. J. Miller, R. Miquel, J. J. Mohr, R. C. Nichol, B. Nord, A. A. Plazas, A. K. Romer, A. Roodman, E. S. Rykoff, E. Sanchez, V. Scarpine, M. Schubnell, I. Sevilla-Noarbe, R. C. Smith, M. Soares-Santos, F. Sobreira, M. E. C. Swanson, G. Tarle, D. Thomas, V. Vikram, A. R. Walker, Y. Zhang, and DES Collaboration (2016, December). Cosmology constraints from shear peak statistics in Dark Energy Survey Science Verification data. *MNRAS* 463, 3653–3673.
- King, L. J., D. I. Clowe, J. E. Coleman, H. R. Russell, R. Santana, J. A. White, R. E. A. Canning, N. J. Deering, A. C. Fabian, B. E. Lee, B. Li, and B. R. McNamara (2016, June). The distribution of dark and luminous matter in the unique galaxy cluster merger Abell 2146. *MNRAS* 459, 517–527.
- Klypin, A., G. Yepes, S. Gottlöber, F. Prada, and S. Heß (2016, April). MultiDark simulations: the story of dark matter halo concentrations and density profiles. *MNRAS* 457, 4340–4359.
- Klypin, A. A., S. Trujillo-Gomez, and J. Primack (2011, October). Dark Matter Halos in the Standard Cosmological Model: Results from the Bolshoi Simulation. *ApJ* 740, 102.
- Komatsu, E., K. M. Smith, J. Dunkley, C. L. Bennett, B. Gold, G. Hinshaw, N. Jarosik, D. Larson, M. R.olta, L. Page, D. N. Spergel, M. Halpern, R. S. Hill, A. Kogut, M. Limon, S. S. Meyer, N. Odegard, G. S. Tucker, J. L. Weiland, E. Wollack, and E. L. Wright (2011, February). Seven-year Wilkinson Microwave Anisotropy Probe (WMAP) Observations: Cosmological Interpretation. *ApJs* 192, 18.
- Kratochvil, J. M., Z. Haiman, and M. May (2010, February). Probing cosmology with weak lensing peak counts. *Phys. Rev. D* 81, 043519.
- Kravtsov, A. V. and S. Borgani (2012, September). Formation of Galaxy Clusters. *Annual Review of Astronomy and Astrophysics* 50, 353–409.

- Kruse, G. and P. Schneider (1999, February). Statistics of dark matter haloes expected from weak lensing surveys. *MNRAS* 302, 821–829.
- Kruse, G. and P. Schneider (2000, October). The non-Gaussian tail of cosmic-shear statistics. *MNRAS* 318, 321–328.
- Lahav, O., A. Kiakotou, F. B. Abdalla, and C. Blake (2010, June). Forecasting neutrino masses from galaxy clustering in the Dark Energy Survey combined with the Planck measurements. *MNRAS* 405, 168–176.
- Laureijs, R., J. Amiaux, S. Arduini, J. L. Auguères, J. Brinchmann, R. Cole, M. Cropper, C. Dabin, L. Duvet, A. Ealet, B. Garilli, P. Gondoin, L. Guzzo, J. Hoar, H. Hoekstra, R. Holmes, T. Kitching, T. Maciaszek, Y. Mellier, F. Pasian, W. Percival, J. Rhodes, G. Saavedra Criado, M. Sauvage, R. Scaramella, L. Valenziano, S. Warren, R. Bender, F. Castander, A. Cimatti, O. Le Fèvre, H. Kurki-Suonio, M. Levi, P. Lilje, G. Meylan, R. Nichol, K. Pedersen, V. Popa, R. Rebolo Lopez, H. W. Rix, H. Rottgering, W. Zeilinger, F. Grupp, P. Hudelot, R. Massey, M. Meneghetti, L. Miller, S. Paltani, S. Paulin-Henriksson, S. Pires, C. Saxton, T. Schrabback, G. Seidel, J. Walsh, N. Aghanim, L. Amendola, J. Bartlett, C. Baccigalupi, J. P. Beaulieu, K. Benabed, J. G. Cuby, D. Elbaz, P. Fosalba, G. Gavazzi, A. Helmi, I. Hook, M. Irwin, J. P. Kneib, M. Kunz, F. Mannucci, L. Moscardini, C. Tao, R. Teyssier, J. Weller, G. Zamorani, M. R. Zapatero Osorio, O. Boulade, J. J. Fomond, A. Di Giorgio, P. Guttridge, A. James, M. Kemp, J. Martignac, A. Spencer, D. Walton, T. Blümchen, C. Bonoli, F. Bortoletto, C. Cerna, L. Corcione, C. Fabron, K. Jahnke, S. Ligori, F. Madrid, L. Martin, G. Morgante, T. Pampونا, E. Prieto, M. Riva, R. Toledo, M. Trifoglio, F. Zerbi, F. Abdalla, M. Douspis, C. Grenet, S. Borgani, R. Bouwens, F. Courbin, J. M. Delouis, P. Dubath, A. Fontana, M. Frailis, A. Grazian, J. Koppenhöfer, O. Mansutti, M. Melchior, M. Mignoli, J. Mohr, C. Neissner, K. Noddle, M. Poncet, M. Scodreggio, S. Serrano, N. Shane, J. L. Starck, C. Surace, A. Taylor, G. Verdoes-Kleijn, C. Vuerli, O. R. Williams, A. Zacchei, B. Altieri, I. Escudero Sanz, R. Kohley, T. Oosterbroek, P. Astier, D. Bacon, S. Bardelli, C. Baugh, F. Bellagamba, C. Benoist, D. Bianchi, A. Biviano, E. Branchini, C. Carbone, V. Cardone, D. Clements, S. Colombi, C. Conselice, G. Cresci, N. Deacon, J. Dunlop, C. Fedeli, F. Fontanot, P. Franzetti, C. Giocoli, J. Garcia-Bellido, J. Gow, A. Heavens, P. Hewett, C. Heymans, A. Holland, Z. Huang, O. Ilbert, B. Joachimi, E. Jennins, E. Kerins, A. Kiessling, D. Kirk, R. Kotak, O. Krause, O. Lahav, F. van Leeuwen, J. Lesgourgues, M. Lombardi, M. Magliocchetti, K. Maguire, E. Majerotto, R. Maoli, F. Marulli, S. Maurogordato, H. McCracken, R. McLure, A. Melchiorri, A. Merson, M. Moresco, M. Nonino, P. Norberg, J. Peacock, R. Pello, M. Penny, V. Pettorino, C. Di Porto, L. Pozzetti, C. Quercellini, M. Radovich, A. Rassat, N. Roche, S. Ronayette, E. Rossetti, B. Sartoris, P. Schneider, E. Semboloni, S. Serjeant, F. Simpson, C. Skordis, G. Smadja, S. Smartt, P. Spano, S. Spiro, M. Sullivan, A. Tilquin, R. Trotta, L. Verde, Y. Wang, G. Williger, G. Zhao, J. Zoubian, and E. Zucca (2011, October). Euclid Definition Study Report. *ArXiv e-prints*, arXiv:1110.3193.

- Le Brun, A. M. C., I. G. McCarthy, J. Schaye, and T. J. Ponman (2014, June). Towards a realistic population of simulated galaxy groups and clusters. *MNRAS* *441*, 1270–1290.
- Lee, B. E., A. M. C. Le Brun, M. E. Haq, N. J. Deering, L. J. King, D. Applegate, and I. G. McCarthy (2018, May). The relative impact of baryons and cluster shape on weak lensing mass estimates of galaxy clusters. *MNRAS*.
- Leonard, A., S. Pires, and J.-L. Starck (2012, July). Fast calculation of the weak lensing aperture mass statistic. *MNRAS* *423*, 3405–3412.
- Lesgourgues, J. and S. Pastor (2006, July). Massive neutrinos and cosmology. *Phys. Rep.* *429*, 307–379.
- Li, Z., J. Liu, J. M. Zorrilla Matilla, and W. R. Coulton (2018, October). Constraining neutrino mass with tomographic weak lensing peak counts. *ArXiv e-prints*.
- Lin, C.-A. and M. Kilbinger (2015, November). A new model to predict weak-lensing peak counts. II. Parameter constraint strategies. *A&A* *583*, A70.
- Liu, J. and Z. Haiman (2016, August). Origin of weak lensing convergence peaks. *Phys. Rev. D* *94*, 043533.
- Liu, X., B. Li, G.-B. Zhao, M.-C. Chiu, W. Fang, C. Pan, Q. Wang, W. Du, S. Yuan, L. Fu, and Z. Fan (2016, July). Constraining $f(R)$ Gravity Theory Using Weak Lensing Peak Statistics from the Canada-France-Hawaii-Telescope Lensing Survey. *Phys. Rev. Lett.* *117*, 051101.
- Martinet, N., J. G. Bartlett, A. Kiessling, and B. Sartoris (2015, September). Constraining cosmology with shear peak statistics: tomographic analysis. *A&A* *581*, A101.
- Martinet, N., P. Schneider, H. Hildebrandt, H. Shan, M. Asgari, J. P. Dietrich, J. Harnois-Déraps, T. Erben, A. Grado, C. Heymans, H. Hoekstra, D. Klaes, K. Kuijken, J. Merten, and R. Nakajima (2018, February). Kids-450: cosmological constraints from weak-lensing peak statistics - ii: Inference from shear peaks using n-body simulations. *MNRAS* *474*, 712–730.
- Maturi, M., C. Angrick, F. Pace, and M. Bartelmann (2010, September). An analytic approach to number counts of weak-lensing peak detections. *A&A* *519*, A23.
- McCarthy, I. G., S. Bird, J. Schaye, J. Harnois-Déraps, A. S. Font, and L. van Waerbeke (2018, May). The bahamas project: the cmb-large-scale structure tension and the roles of massive neutrinos and galaxy formation. *MNRAS* *476*, 2999–3030.
- McCarthy, I. G., J. Schaye, S. Bird, and A. M. C. Le Brun (2017, March). The bahamas project: calibrated hydrodynamical simulations for large-scale structure cosmology. *MNRAS* *465*, 2936–2965.

- Moore, B., S. Ghigna, F. Governato, G. Lake, T. Quinn, J. Stadel, and P. Tozzi (1999, October). Dark Matter Substructure within Galactic Halos. *ApJ* 524, L19–L22.
- More, S., B. Diemer, and A. V. Kravtsov (2015, September). The Splashback Radius as a Physical Halo Boundary and the Growth of Halo Mass. *ApJ* 810, 36.
- More, S., H. Miyatake, M. Takada, B. Diemer, A. V. Kravtsov, N. K. Dalal, A. More, R. Murata, R. Mandelbaum, E. Rozo, E. S. Rykoff, M. Oguri, and D. N. Spergel (2016, July). Detection of the Splashback Radius and Halo Assembly Bias of Massive Galaxy Clusters. *ApJ* 825, 39.
- Moscardini, L., M. Baldi, and C. Giocoli (2018, 09). Weak lensing light-cones in modified gravity simulations with and without massive neutrinos. *Monthly Notices of the Royal Astronomical Society* 481(2), 2813–2828.
- Mummery, B. O., I. G. McCarthy, S. Bird, and J. Schaye (2017, October). The separate and combined effects of baryon physics and neutrino free streaming on large-scale structure. *MNRAS* 471, 227–242.
- Namikawa, T., S. Saito, and A. Taruya (2010, December). Probing dark energy and neutrino mass from upcoming lensing experiments of CMB and galaxies. *Journal of Cosmology and Astro-Particle Physics* 2010, 027.
- Navarro, J. F., C. S. Frenk, and S. D. M. White (1997, December). A Universal Density Profile from Hierarchical Clustering. *ApJ* 490, 493–508.
- Navarro, J. F., E. Hayashi, C. Power, A. R. Jenkins, C. S. Frenk, S. D. M. White, V. Springel, J. Stadel, and T. R. Quinn (2004, April). The inner structure of Λ CDM haloes - III. Universality and asymptotic slopes. *MNRAS* 349, 1039–1051.
- Navarro, J. F., A. Ludlow, V. Springel, J. Wang, M. Vogelsberger, S. D. M. White, A. Jenkins, C. S. Frenk, and A. Helmi (2010, February). The diversity and similarity of simulated cold dark matter haloes. *MNRAS* 402, 21–34.
- Newville, M., T. Stensitzki, D. B. Allen, and A. Ingargiola (2014, September). LMFIT: Non-Linear Least-Square Minimization and Curve-Fitting for Python.
- Niikura, H., M. Takada, N. Okabe, R. Martino, and R. Takahashi (2015, December). Detection of universality of dark matter profile from Subaru weak lensing measurements of 50 massive clusters. *PASJ* 67, 103.
- Oguri, M., J. Lee, and Y. Suto (2003, December). Arc Statistics in Triaxial Dark Matter Halos: Testing the Collisionless Cold Dark Matter Paradigm. *ApJ* 599, 7–23.
- Okabe, N. and G. P. Smith (2016, October). LoCuSS: weak-lensing mass calibration of galaxy clusters. *MNRAS* 461, 3794–3821.

- Okabe, N., M. Takada, K. Umetsu, T. Futamase, and G. P. Smith (2010, June). LoCuSS: Subaru Weak Lensing Study of 30 Galaxy Clusters. *PASJ* 62, 811–870.
- Osato, K., M. Shirasaki, and N. Yoshida (2015, June). Impact of Baryonic Processes on Weak-lensing Cosmology: Power Spectrum, Nonlocal Statistics, and Parameter Bias. *ApJ* 806, 186.
- Peel, A., C.-A. Lin, F. Lanusse, A. Leonard, J.-L. Starck, and M. Kilbinger (2017, March). Cosmological constraints with weak-lensing peak counts and second-order statistics in a large-field survey. *A&A* 599, A79.
- Peel, A., V. Pettorino, C. Giocoli, J.-L. Starck, and M. Baldi (2018, November). Breaking degeneracies in modified gravity with higher (than 2nd) order weak-lensing statistics. *A&A* 619, A38.
- Peter, A. H. G., M. Rocha, J. S. Bullock, and M. Kaplinghat (2013, March). Cosmological simulations with self-interacting dark matter - II. Halo shapes versus observations. *MNRAS* 430, 105–120.
- Pillepich, A., V. Springel, D. Nelson, S. Genel, J. Naiman, R. Pakmor, L. Hernquist, P. Torrey, M. Vogelsberger, R. Weinberger, and F. Marinacci (2018, January). Simulating galaxy formation with the IllustrisTNG model. *MNRAS* 473, 4077–4106.
- Planck Collaboration, P. A. R. Ade, N. Aghanim, Y. Akrami, P. K. Aluri, M. Arnaud, M. Ashdown, J. Aumont, C. Baccigalupi, A. J. Banday, and et al. (2016, September). Planck 2015 results. XVI. Isotropy and statistics of the CMB. *A&A* 594, A16.
- Planck Collaboration, P. A. R. Ade, N. Aghanim, M. Arnaud, M. Ashdown, J. Aumont, C. Baccigalupi, A. J. Banday, R. B. Barreiro, J. G. Bartlett, and et al. (2016a, September). Planck 2015 results. XIII. Cosmological parameters. *A&A* 594, A13.
- Planck Collaboration, P. A. R. Ade, N. Aghanim, M. Arnaud, M. Ashdown, J. Aumont, C. Baccigalupi, A. J. Banday, R. B. Barreiro, J. G. Bartlett, and et al. (2016b, September). Planck 2015 results. XIII. Cosmological parameters. *A&A* 594, A13.
- Planck Collaboration, N. Aghanim, Y. Akrami, M. Ashdown, J. Aumont, C. Baccigalupi, M. Ballardini, A. J. Banday, R. B. Barreiro, N. Bartolo, S. Basak, R. Battye, K. Benabed, J. P. Bernard, M. Bersanelli, P. Bielewicz, J. J. Bock, J. R. Bond, J. Borrill, F. R. Bouchet, F. Boulanger, M. Bucher, C. Burigana, R. C. Butler, E. Calabrese, J. F. Cardoso, J. Carron, A. Challinor, H. C. Chiang, J. Chluba, L. P. L. Colombo, C. Combet, D. Contreras, B. P. Crill, F. Cuttaia, P. de Bernardis, G. de Zotti, J. Delabrouille, J. M. Delouis, E. Di Valentino, J. M. Diego, O. Doré, M. Douspis, A. Ducout, X. Dupac, S. Dusini, G. Efstathiou, F. Elsner, T. A. Enßlin, H. K. Eriksen, Y. Fantaye, M. Farhang, J. Fergusson, R. Fernandez-Cobos, F. Finelli, F. Forastieri, M. Frailis, E. Franceschi, A. Frolov, S. Galeotta, S. Galli, K. Ganga, R. T. Génova-Santos, M. Gerbino, T. Ghosh, J. González-Nuevo,

K. M. Górski, S. Gratton, A. Gruppuso, J. E. Gudmundsson, J. Hamann, W. Handley, D. Herranz, E. Hivon, Z. Huang, A. H. Jaffe, W. C. Jones, A. Karakci, E. Keihänen, R. Keskitalo, K. Kiiveri, J. Kim, T. S. Kisner, L. Knox, N. Krachmalnicoff, M. Kunz, H. Kurki-Suonio, G. Lagache, J. M. Lamarre, A. Lasenby, M. Lattanzi, C. R. Lawrence, M. Le Jeune, P. Lemos, J. Lesgourgues, F. Levrier, A. Lewis, M. Liguori, P. B. Lilje, M. Lilley, V. Lindholm, M. López-Caniego, P. M. Lubin, Y. Z. Ma, J. F. Macías-Pérez, G. Maggio, D. Maino, N. Mandolesi, A. Mangilli, A. Marcos-Caballero, M. Maris, P. G. Martin, M. Martinelli, E. Martínez-González, S. Matarrese, N. Mauri, J. D. McEwen, P. R. Meinhold, A. Melchiorri, A. Mennella, M. Migliaccio, M. Millea, S. Mitra, M. A. Miville-Deschênes, D. Molinari, L. Montier, G. Morgante, A. Moss, P. Natoli, H. U. Nørgaard-Nielsen, L. Pagano, D. Paoletti, B. Partridge, G. Patanchon, H. V. Peiris, F. Perrotta, V. Pettorino, F. Piacentini, L. Polastri, G. Polenta, J. L. Puget, J. P. Rachen, M. Reinecke, M. Remazeilles, A. Renzi, G. Rocha, C. Rosset, G. Roudier, J. A. Rubiño-Martín, B. Ruiz-Granados, L. Salvati, M. Sandri, M. Savelainen, D. Scott, E. P. S. Shellard, C. Sirignano, G. Sirri, L. D. Spencer, R. Sunyaev, A. S. Suur-Uski, J. A. Tauber, D. Tavagnacco, M. Tenti, L. Toffolatti, M. Tomasi, T. Trombetti, L. Valenziano, J. Valiviita, B. Van Tent, L. Vibert, P. Vielva, F. Villa, N. Vittorio, B. D. Wandelt, I. K. Wehus, M. White, S. D. M. White, A. Zacchei, and A. Zonca (2018, Jul). Planck 2018 results. VI. Cosmological parameters. *arXiv e-prints*, arXiv:1807.06209.

Planck Collaboration, N. Aghanim, Y. Akrami, M. Ashdown, J. Aumont, C. Baccigalupi, M. Ballardini, A. J. Banday, R. B. Barreiro, N. Bartolo, S. Basak, K. Benabed, M. Bersanelli, P. Bielewicz, A. Bonaldi, L. Bonavera, J. R. Bond, J. Borrill, F. R. Bouchet, C. Burigana, E. Calabrese, J. F. Cardoso, A. Challinor, H. C. Chiang, L. P. L. Colombo, C. Combet, B. P. Crill, A. Curto, F. Cuttaia, P. de Bernardis, A. de Rosa, G. de Zotti, J. Delabrouille, E. Di Valentino, C. Dickinson, J. M. Diego, O. Doré, A. Ducout, X. Dupac, S. Dusini, G. Efstathiou, F. Elsner, T. A. Enßlin, H. K. Eriksen, Y. Fantaye, F. Finelli, F. Forastieri, M. Frailis, E. Franceschi, A. Frolov, S. Galeotta, S. Galli, K. Ganga, R. T. Génova-Santos, M. Gerbino, J. González-Nuevo, K. M. Górski, S. Gratton, A. Gruppuso, J. E. Gudmundsson, D. Herranz, E. Hivon, Z. Huang, A. H. Jaffe, W. C. Jones, E. Keihänen, R. Keskitalo, K. Kiiveri, J. Kim, T. S. Kisner, L. Knox, N. Krachmalnicoff, M. Kunz, H. Kurki-Suonio, G. Lagache, J. M. Lamarre, A. Lasenby, M. Lattanzi, C. R. Lawrence, M. Le Jeune, F. Levrier, A. Lewis, M. Liguori, P. B. Lilje, M. Lilley, V. Lindholm, M. López-Caniego, P. M. Lubin, Y. Z. Ma, J. F. Macías-Pérez, G. Maggio, D. Maino, N. Mandolesi, A. Mangilli, M. Maris, P. G. Martin, E. Martínez-González, S. Matarrese, N. Mauri, J. D. McEwen, P. R. Meinhold, A. Mennella, M. Migliaccio, M. Millea, M. A. Miville-Deschênes, D. Molinari, A. Moneti, L. Montier, G. Morgante, A. Moss, A. Narimani, P. Natoli, C. A. Oxborrow, L. Pagano, D. Paoletti, B. Partridge, G. Patanchon, L. Patrizii, V. Pettorino, F. Piacentini, L. Polastri, G. Polenta, J. L. Puget, J. P. Rachen, B. Racine, M. Reinecke, M. Remazeilles, A. Renzi, G. Rocha, M. Rossetti, G. Roudier, J. A. Rubiño-Martín, B. Ruiz-Granados, L. Salvati, M. Sandri, M. Savelainen, D. Scott, C. Sirignano, G. Sirri, L. Stanco, A. S. Suur-Uski, J. A. Tauber, D. Tavagnacco, M. Tenti, L. Toffolatti, M. Tomasi, M. Tristram, T. Trombetti, J. Valiviita, F. Van Tent,

- P. Vielva, F. Villa, N. Vittorio, B. D. Wandelt, I. K. Wehus, M. White, A. Zacchei, and A. Zonca (2017, Nov). Planck intermediate results. LI. Features in the cosmic microwave background temperature power spectrum and shifts in cosmological parameters. *A&A* 607, A95.
- Postman, M., D. Coe, N. Benítez, L. Bradley, T. Broadhurst, M. Donahue, H. Ford, O. Graur, G. Graves, S. Jouvel, A. Koekemoer, D. Lemze, E. Medezinski, A. Molino, L. Moustakas, S. Ogaz, A. Riess, S. Rodney, P. Rosati, K. Umetsu, W. Zheng, A. Zitrin, M. Bartelmann, R. Bouwens, N. Czakon, S. Golwala, O. Host, L. Infante, S. Jha, Y. Jimenez-Teja, D. Kelson, O. Lahav, R. Lazkoz, D. Maoz, C. McCully, P. Melchior, M. Meneghetti, J. Merten, J. Moustakas, M. Nonino, B. Patel, E. Regös, J. Sayers, S. Seitz, and A. Van der Wel (2012, April). The Cluster Lensing and Supernova Survey with Hubble: An Overview. *ApJs* 199, 25.
- Poulin, V., K. K. Boddy, S. Bird, and M. Kamionkowski (2018, Jun). Implications of an extended dark energy cosmology with massive neutrinos for cosmological tensions. *Phys. Rev. D* 97, 123504.
- Prada, F., A. A. Klypin, A. J. Cuesta, J. E. Betancort-Rijo, and J. Primack (2012, July). Halo concentrations in the standard Λ cold dark matter cosmology. *MNRAS* 423, 3018–3030.
- Prada, F., A. A. Klypin, E. Simonneau, J. Betancort-Rijo, S. Patiri, S. Gottlöber, and M. A. Sanchez-Conde (2006, July). How Far Do They Go? The Outer Structure of Galactic Dark Matter Halos. *ApJ* 645, 1001–1011.
- Randall, S. W., M. Markevitch, D. Clowe, A. H. Gonzalez, and M. Bradač (2008, June). Constraints on the Self-Interaction Cross Section of Dark Matter from Numerical Simulations of the Merging Galaxy Cluster 1E 0657-56. *ApJ* 679, 1173–1180.
- Riess, A. G., S. Casertano, W. Yuan, L. Macri, J. Anderson, J. W. MacKenty, J. B. Bowers, K. I. Clubb, A. V. Filippenko, D. O. Jones, and B. E. Tucker (2018, Mar). New Parallaxes of Galactic Cepheids from Spatially Scanning the Hubble Space Telescope: Implications for the Hubble Constant. *ApJ* 855, 136.
- Sawala, T., C. S. Frenk, R. A. Crain, A. Jenkins, J. Schaye, T. Theuns, and J. Zavala (2013, May). The abundance of (not just) dark matter haloes. *MNRAS* 431, 1366–1382.
- Schaye, J., R. A. Crain, R. G. Bower, M. Furlong, M. Schaller, T. Theuns, C. Dalla Vecchia, C. S. Frenk, I. G. McCarthy, J. C. Helly, A. Jenkins, Y. M. Rosas-Guevara, S. D. M. White, M. Baes, C. M. Booth, P. Camps, J. F. Navarro, Y. Qu, A. Rahmati, T. Sawala, P. A. Thomas, and J. Trayford (2015, January). The EAGLE project: simulating the evolution and assembly of galaxies and their environments. *MNRAS* 446, 521–554.

- Schaye, J. and C. Dalla Vecchia (2008, January). On the relation between the Schmidt and Kennicutt-Schmidt star formation laws and its implications for numerical simulations. *MNRAS* 383, 1210–1222.
- Schaye, J., C. Dalla Vecchia, C. M. Booth, R. P. C. Wiersma, T. Theuns, M. R. Haas, S. Bertone, A. R. Duffy, I. G. McCarthy, and F. van de Voort (2010, March). The physics driving the cosmic star formation history. *MNRAS* 402, 1536–1560.
- Schirmer, M., T. Erben, M. Hettterscheidt, and P. Schneider (2007, February). GaBoDS: the Garching-Bonn Deep Survey. IX. A sample of 158 shear-selected mass concentration candidates. *A&A* 462, 875–887.
- Schneider, A. and R. Teyssier (2015, December). A new method to quantify the effects of baryons on the matter power spectrum. *J. Cosmology Astropart. Phys.* 12, 049.
- Schneider, P. (1996, December). Detection of (dark) matter concentrations via weak gravitational lensing. *MNRAS* 283, 837–853.
- Schneider, P. (2005, September). Weak gravitational lensing. *ArXiv Astrophysics e-prints*.
- Schneider, P., J. Ehlers, and E. E. Falco (1992). *Gravitational Lenses*.
- Schneider, P., L. King, and T. Erben (2000, January). Cluster mass profiles from weak lensing: constraints from shear and magnification information. *A&A* 353, 41–56.
- Schneider, P., L. van Waerbeke, B. Jain, and G. Kruse (1998, June). A new measure for cosmic shear. *MNRAS* 296, 873–892.
- Shan, H., X. Liu, H. Hildebrandt, C. Pan, N. Martinet, Z. Fan, P. Schneider, M. Asgari, J. Harnois-Déraps, H. Hoekstra, A. Wright, J. P. Dietrich, T. Erben, F. Getman, A. Grado, C. Heymans, D. Klaes, K. Kuijken, J. Merten, E. Puddu, M. Radovich, and Q. Wang (2018, February). KiDS-450: cosmological constraints from weak lensing peak statistics - I. Inference from analytical prediction of high signal-to-noise ratio convergence peaks. *MNRAS* 474, 1116–1134.
- Shaw, L. D., J. Weller, J. P. Ostriker, and P. Bode (2006, August). Statistics of Physical Properties of Dark Matter Clusters. *ApJ* 646, 815–833.
- Slipher, V. M. (1913). The radial velocity of the Andromeda Nebula. *Lowell Observatory Bulletin* 2, 56–57.
- Snaith, O. N., J. Bailin, A. Knebe, G. Stinson, J. Wadsley, and H. Couchman (2017, December). Haloes at the ragged edge: the importance of the splashback radius. *MNRAS* 472, 2694–2712.

- Spergel, D. N. and P. J. Steinhardt (2000, April). Observational Evidence for Self-Interacting Cold Dark Matter. *Physical Review Letters* *84*, 3760–3763.
- Springel, V. (2005, December). The cosmological simulation code gadget-2. *MNRAS* *364*, 1105–1134.
- Springel, V., S. D. M. White, A. Jenkins, C. S. Frenk, N. Yoshida, L. Gao, J. Navarro, R. Thacker, D. Croton, J. Helly, J. A. Peacock, S. Cole, P. Thomas, H. Couchman, A. Evrard, J. Colberg, and F. Pearce (2005, June). Simulations of the formation, evolution and clustering of galaxies and quasars. *Nature* *435*, 629–636.
- Stark, A. A. (1977, April). Triaxial Models of the Bulge of M31. *ApJ* *213*, 368–373.
- Subramanian, K. and S. A. Cowling (1986, March). On local conditions for multiple imaging by bounded, smooth gravitational lenses. *MNRAS* *219*, 333–346.
- Umetsu, K. and B. Diemer (2017, February). Lensing Constraints on the Mass Profile Shape and the Splashback Radius of Galaxy Clusters. *ApJ* *836*, 231.
- Umetsu, K., A. Zitrin, D. Gruen, J. Merten, M. Donahue, and M. Postman (2016, April). CLASH: Joint Analysis of Strong-lensing, Weak-lensing Shear, and Magnification Data for 20 Galaxy Clusters. *ApJ* *821*, 116.
- van Daalen, M. P., J. Schaye, C. M. Booth, and C. Dalla Vecchia (2011, August). The effects of galaxy formation on the matter power spectrum: a challenge for precision cosmology. *MNRAS* *415*, 3649–3665.
- Velliscig, M., M. P. van Daalen, J. Schaye, I. G. McCarthy, M. Cacciato, A. M. C. Le Brun, and C. Dalla Vecchia (2014, August). The impact of galaxy formation on the total mass, mass profile and abundance of haloes. *MNRAS* *442*, 2641–2658.
- Villaescusa-Navarro, F., F. Marulli, M. Viel, E. Branchini, E. Castorina, E. Sefusatti, and S. Saito (2014, March). Cosmology with massive neutrinos I: towards a realistic modeling of the relation between matter, haloes and galaxies. *Journal of Cosmology and Astro-Particle Physics* *2014*, 011.
- Vogelsberger, M., S. Genel, D. Sijacki, P. Torrey, V. Springel, and L. Hernquist (2013, December). A model for cosmological simulations of galaxy formation physics. *MNRAS* *436*, 3031–3067.
- Voit, G. M. (2005, April). Tracing cosmic evolution with clusters of galaxies. *Reviews of Modern Physics* *77*, 207–258.
- Wagner, C., L. Verde, and R. Jimenez (2012, June). Effects of the Neutrino Mass Splitting on the Nonlinear Matter Power Spectrum. *ApJ* *752*, L31.

- Weinberg, S. (1972, July). *Gravitation and Cosmology: Principles and Applications of the General Theory of Relativity*.
- Wen, Z. L., J. L. Han, and F. S. Liu (2010, September). Mass function of rich galaxy clusters and its constraint on σ_8 . *MNRAS* *407*, 533–543.
- White, M. and C. Vale (2004, October). Simulations of weak gravitational lensing. *Astroparticle Physics* *22*, 19–27.
- Wiersma, R. P. C., J. Schaye, and B. D. Smith (2009, February). The effect of photoionization on the cooling rates of enriched, astrophysical plasmas. *MNRAS* *393*, 99–107.
- Wiersma, R. P. C., J. Schaye, T. Theuns, C. Dalla Vecchia, and L. Tornatore (2009, October). Chemical enrichment in cosmological, smoothed particle hydrodynamics simulations. *MNRAS* *399*, 574–600.
- Wyman, M., D. H. Rudd, R. A. Vanderveld, and W. Hu (2014, Feb). Neutrinos help reconcile planck measurements with the local universe. *Phys. Rev. Lett.* *112*, 051302.
- Yang, X., J. M. Kratochvil, K. Huffenberger, Z. Haiman, and M. May (2013, January). Baryon impact on weak lensing peaks and power spectrum: Low-bias statistics and self-calibration in future surveys. *Phys. Rev. D* *87*, 023511.
- Yang, X., J. M. Kratochvil, S. Wang, E. A. Lim, Z. Haiman, and M. May (2011, August). Cosmological information in weak lensing peaks. *Phys. Rev. D* *84*, 043529.
- Zwicky, F. (1937, October). On the Masses of Nebulae and of Clusters of Nebulae. *ApJ* *86*, 217.

BIOGRAPHICAL SKETCH

Matthew Fong was born in San Jose, California. He was accepted to San Jose State University in 2007. After receiving a Bachelor of Science with a major in Physics and minor in Mathematics from San Jose State University in December 2012, he entered the physics graduate program at The University of Texas at Dallas in 2014. There he obtained his Master of Science in Physics in 2015 and then his PhD in Physics in 2019.

CURRICULUM VITAE

Matthew Fong

mxfl40930@utdallas.edu

Education

The University of Texas at Dallas (UTD), Dallas, TX

MS Physics (GPA 3.8)

12/2015

PhD Physics & Astrophysics

Expected Spring 2019

San Jose State University (SJSU), San Jose, CA

BS Physics, Minor in Mathematics

12/2012

Publications

UTD

- Study on the outskirts of galaxy clusters creating and using synthetic weak lensing data from simulations (05/2018):
M. Fong, R. Bowyer, A. Whitehead, B. Lee, L.J. King, D. Applegate, I. McCarthy; *Prospects for Determining the Mass Distributions of Galaxy Clusters on Large Scales Using Weak Gravitational Lensing, Monthly Notices of the Royal Astronomical Society*, sty1339, <https://doi.org/10.1093/mnras/sty1339>
[Work for this paper involved advising 2 undergraduate students. RB was an NSF REU (Research Experiences for Undergraduates) Fellow at the Maria Mitchell Observatory (PI Dr. Regina Jorgenson), and she then wrote her senior thesis at Rice University; along with LJK, I was her external advisor during both periods]
- Study on the impact of cosmology, baryons, and neutrinos on weak lensing statistics:
M. Fong, M. Choi, V. Catlett, B. Lee, A. Peel, R. Bowyer, L.J. King, I. McCarthy; *The Impact of Baryonic Physics and Neutrino Masses on Weak Lensing Peak Statistics* (MNRAS Submitted: MN-19-1088-MJ)
[VC is currently an undergraduate at UT Dallas, who started working with us in the summer before her first year]
- Current Work on weak lensing from triaxial galaxy clusters:
M. Fong, B. Lee, P. Gibson, A. Mendoza, V. Catlett, L.J. King, I. McCarthy; *Analysis of triaxiality in galaxy clusters using joint weak and strong lensing, SZ, and X-ray data*
[This work involves undergraduates Peter Gibson (Williamette University) who was an REU student at the Maria Mitchell Observatory and Alexandria Mendoza (McMurry University Abilene, TX) who was an REU student at UT Dallas new REU program]

Lawrence Livermore National Laboratory & SJSU

01/2013

Analysis of photonuclear reaction data:

K. Parvin, M.S. Johnson, R. Espinoza, M. Fong, T. Slauter, *Final Report for the San Jose State University Effort for Lawrence Livermore National Laboratory – Analysis of photonuclear reaction data*; Technical Report, LLNL-SR-611472 (2013)

Computing & Technical Skills

Creation and analysis of synthetic data from hydrodynamic cosmological simulations.

Cluster mass modelling and weak lensing statistics of real and synthetic data.

Development of algorithms for gravitational lensing analysis.

Highly proficient with Python, Matlab. Experience with Mathematica, Java Script.

Computing on various platforms including use of Texas Advanced Computing Center.

Highly proficient with Microsoft Office, LaTeX.

Research Experience

Graduate Researcher at UTD

08/2014—current

- Suites of cosmological hydrodynamical simulations that include baryonic prescriptions and summed neutrino mass, such as cosmo-OWLS (the Overwhelmingly Large Simulations) and BAHAMAS (Baryons and HALoes of MASSive Systems), were used in studying galaxy clusters, large scale structure, and cosmology.
- Generate synthetic weak lensing (WL) data from simulations that match the survey capabilities of current and near-future surveys like Kilo Degree Survey (KiDS), Euclid, Hubble Space Telescope (HST), and the Large Synoptic Survey Telescope (LSST).

- Collaborated with LSST Dark Energy Science Collaboration (DESC) members in creating the cluster mass modelling (CLMM) and Core Cosmology Library (CCL) modules by providing and writing code on cluster density to weak lensing profiles.
- Develop code to quickly analyze synthetic lensing catalogues to determine important characteristics about clusters, necessary for cosmological parameter constraint.
- Determined the density profiles of clusters in their large scale environments, giving insight on the splash back radius and evolution of clusters, by stacking cluster WL signals.
- Study the impact of neutrinos on cluster characteristics their shapes, mergers, and lensing signatures.
- Develop triaxial mass modelling code for galaxy cluster data.

Graduate TA at UTD

08/2014—current

- TA for graduate Cosmology course and undergraduate Extragalactic Astrophysics Course.
- Set up demos, hold office hours to assist with physical principles, ideas, and applications, and grade homeworks and exams for undergraduate Contemporary Physics and Electromagnetism and Waves.
- Instructed and managed undergraduate mechanics labs by clarifying physical concepts, how to apply theory for predictions and hands-on experiments, to use and maintain equipment, and maintain an organized work space.
- Taught Python a class to graduate students.

SJSU Research Foundation, San Jose, CA

05/2011—10/2012

- Researched and published the analysis of photonuclear measurement data taken at Duke University's Free Electron Laser Laboratory using the High Intensity Gamma-ray Source (HIGS) at Duke University.
- Wrote the background/set-up on how the experiment was done and data was measured.
- Developed code to obtain precise and accurate flux measurements from data taken from HIGS.

Outreach and mentoring

- Mentoring undergraduate students and guiding them in a wide range of research (Carlos Miguel García Rosas [International Student Participating in UTD-Mexico Program], Alisha Whitehead [then at UTD], Rachel Bowyer [then at Rice University], Peter Gibson [Willamette University], Victoria Catlett [UTD], Alexandria Mendoza [McMurry University]).
- Eureka Day at UTD (Summer 2016): Physics workshop for middle school girls from less advantaged economic backgrounds.
- Women in Science and Engineering (WISE) at San Jose, CA (09/2010 – 05/2011):
 - Participated in the 7th annual College of Science Student Research day at SJSU.
 - Discuss the importance of diversity in scientific research and professions.
 - Elucidated the importance of muon detectors, ranging from earthquake predictions to medical applications.

Honors

Scholarship:

University of Texas at Dallas (UTD) Graduate Tuition Scholarship	08/2014 - current
Margie Renfrow Student Support Fund	08/2016, 01/2018
Natural Sciences & Mathematics Mei Lein Fellowship	08/2017

Assistantships:

Graduate Student Instructor at UTD	08/2014 - current
Graduate Student Researcher at UTD	08/2014 - current

Organizations/Memberships

Dark Energy Science Collaboration (DESC)
 The Large Synoptic Survey Telescope (LSST)
 The American Astronomical Society (AAS)
 The Golden Key International Honour Society